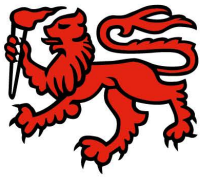

UNIVERSITY *of* TASMANIA | AMC Australian Maritime College

WATERJET TESTING TECHNIQUES FOR POWERING PERFORMANCE ESTIMATION USING A SINGLE CATAMARAN DEMIHULL

by

Konrad Zürcher, B.E. (Hons) (Naval Architecture)

National Centre for Maritime Engineering and Hydrodynamics
Australian Maritime College

Submitted in fulfillment of the requirements
for the Degree of Doctor of Philosophy

Supervisors:
Prof. Neil Bose
Assoc. Prof. Jonathan R. Binns
Prof. Thomas Giles

University of Tasmania
February, 2016

I declare that this thesis contains no material which has been accepted for a degree or diploma by the University or any other institution, except by way of background information and duly acknowledged in the thesis, and that, to the best of my knowledge and belief, this thesis contains no material previously published or written by another person, except where due acknowledgement is made in the text of the thesis.

Signed: _____
Konrad Zürcher

Date: 9/2/2016

Signed: _____
Konrad Zürcher

Date: 9/2/2016

"Engineering is the art of modelling materials we do not wholly understand, into shapes we cannot precisely analyse so as to withstand forces we cannot properly assess, in such a way that the public has no reason to suspect the extent of our ignorance."

- Dr. A. R. Dykes
British Institution of Structural Engineers, 1976

"If you want to have a maximum effect on the design of a new engineering system, learn to draw. Engineers always wind up designing the vehicle to look like the initial artist's concept."

- Georg von Tiesenhausen
Tiesenhausen's Law of Engineering Design

ABSTRACT

A new series of highly efficient medium-speed wave-piercing catamarans is under development to reduce the environmental impact of fast sea transportation. They will operate at speeds where mutual interference between waves and increased resistance produces the characteristic hump in the ship's resistance curve. The challenge is the assessment of the effects of the change in operating conditions on the waterjet propulsion system. Waterjets are used for high-speed multihulls due to their high efficiency when operating at speeds beyond hump speed. However, they are generally not used for medium-speed applications due to the assumed decrease in efficiency at lower speed.

A series of self-propulsion tests of a high-speed wave-piercing catamaran at medium-speeds was carried out to study the influence of the hydrodynamics at medium-speeds on the waterjet propulsors. The model tests were carried out using load varied (i.e. British method) self-propulsion testing in calm water. Due to size requirements of the model, a single demihull was utilised in close proximity to the side wall of the towing tank which acts as the plane of symmetry, reflecting waves generated by the demihull and therefore providing the correct blockage effects and wave interference for the non-existing second demihull.

The results were validated using full-scale sea trials data for the vessel under consideration and for waterjet unit performance comparisons, a set of benchmark data was supplied by the waterjet unit manufacturer. The model tests showed that the propulsion unit at model scale is capable of reflecting the characteristics of the full scale waterjet. Furthermore, a new, thrust based extrapolation method was introduced and utilised with the results of the experimental testing carried out for the waterjet propulsion study. The results of this extrapolation were in correlation with the available full scale powering sea trials data.

ACKNOWLEDGMENTS

First, I would like to thank my supervisors Prof. Neil Bose (Australian Maritime College), Assoc. Prof. Jonathan R. Binns (Australian Maritime College) and Prof. Thomas Giles (University College London) for their consultation, advice and encouragement throughout the whole project.

I would also like to thank Gary Davidson, Tim Roberts, and the rest of the staff at Incat Tasmania and Revolution Design Pty Ltd for all their support in this project, and Rob Verbeek at Wärtsilä for the supply of waterjet data sheets, technical drawings, waterjet unit benchmark test data, and waterjet pump curves.

Many thanks to the engineers of the Australian Maritime College (AMC) towing tank and model test basin Tim Lilienthal and Kirk Meyer for all the help with test setups and data acquisition system, sensor calibration and for answering patiently all the questions posed to them. I would also like to thank Liam Honeychurch for everything that needed to be built and assembled for the model catamaran hull, Dr. Gregor MacFarlane for the patience in allocating, organising testing appointments and testing facilities, and Rowan Carins for all electrical support. Additional to all the mentioned AMC employees, I would like to thank Stuart Phillips for the construction of the model catamaran hull, fairing of the hull, and useful model building tips early on in the research.

I would also like to express my gratitude to my fellow postgraduate students in the AMC research hub for all the interesting discussions and all the encouragement, which is greatly appreciated. Last but not least, I would like to dedicate this thesis to my mother, brother, grandparents and the rest of my family as without their moral support over the years none of this would have been possible. And to my extended family and friends a big thank you for always showing interest in what I am undertaking.

This research has been conducted as part of a collaborative research project between Incat Tasmania Pty Ltd, Revolution Design Pty Ltd, Wärtsilä Corporation, MARIN, and the Australian Maritime College at the University of Tasmania with support from the Australian Research Council's Linkage Project funding scheme, Project ID: LP110100080.

TABLE OF CONTENTS

LIST OF TABLES

LIST OF FIGURES

NOMENCLATURE

Greek Symbols

Symbol	Description	Definition	Units
δ	Boundary layer thickness	-	m
η_0	Free stream efficiency	$\eta_{Pump}\eta_{Duct}\eta_I$	-
η_{Duct}	Ducting efficiency	$\frac{P_{JSE}}{P_{PE}}$	-
η_D	Overall propulsive efficiency	$\frac{P_E}{P_D}$	-
η_{eI}	Energy interaction efficiency	-	-
η_{Inst}	Installation efficiency	-	-
η_{INT}	Total interaction efficiency	$(1-t)\,\frac{\eta_{eI}}{\eta_{mI}}$	-
η_I	Ideal efficiency	$\frac{2}{1+NVR}$	-
η_{Jet}	Momentum or jet efficiency	$\frac{P_{TE}}{P_{JSE}}$	-
η_{JS}	Jet system efficiency	$\frac{P_{JSE}}{P_D}$	-
η_{mI}	Momentum interaction efficiency	$\frac{P_{Net0}}{P_{Net}}$	-
η_{Pump}	Pump efficiency	$\frac{P_{PE}}{P_D}$	-
λ	Full scale to model scale ratio	$\frac{L_s}{L_m}$	-
μ	Viscosity	$\frac{\mu}{\rho}$	Kg/ms
ν	Kinematic viscosity	$\frac{\mu}{\rho}$	m^2/s
ψ	Head coefficient	$\frac{gH_{35}}{(nD)^2}$	-
ρ	Mass density of fluid	-	Kg/m^3
φ	Flow coefficient	$\frac{Q}{nD^3}$	-

θ_N	Jet angle relative to the horizontal at the nozzle (station 6)	-	degrees
ζ_{13}	Inlet duct loss coefficient	$\frac{E_1-E_3}{E_0}$	-
ζ_{57}	Nozzle duct loss coefficient	$\frac{E_5-E_7}{E_7}$	-
ζ_{ij}	Energy loss coefficient between station i and j	-	-

Roman Symbols

Symbol	**Description**	**Definition**	**Units**
A_N	Nozzle discharge area	-	m^2
A_S	Cross sectional area at station s	-	m^2
B	Moulded breadth	-	m
$B_{hull,\ m}$	Beam of model hull	-	m
C_B	Block coefficient	-	-
c_{es}	Energy velocity coefficient at station s	-	-
C_{LD}	Fineness ratio	-	-
C_M	Midship Section coefficient	-	-
c_{ms}	Momentum velocity coefficient at station s	-	-
C_P	Longitudinal prismatic coefficient	-	-
C_p	Local pressure coefficient	$\frac{p-p_0}{\frac{1}{2}\rho V^2}$	-
C_S	Wetted surface coefficient	-	-
C_V	Volumetric coefficient	-	-
C_{VP}	Vertical prismatic coefficient	-	-
C_{WL}	Waterplane area coefficient	-	-
D	Impeller diameter	-	m
$\triangle M$	Change of momentum flux	-	N
$\triangle \overline{M}_x$	Change in momentum flux in x direction	-	N
$\bigtriangledown$	Volumetric displacement	-	m^3

$\triangle$	Displacement	-	tonnes
D_n	Nozzle discharge diameter	-	m
Dp	Pressure differential of flow rate transducer	-	Pa
E_j	Energy flux at station j	-	W
E_S	Total energy flux at station s (kinetic + potential + pressure)	-	W
$E_{S\zeta}$	Total axial (in ζ direction) energy flux at station s	-	W
F_D	Skin friction correction in a self propulsion test carried out at ship self-propulsion point	-	N
F_r	Froude Number	$\frac{V}{\sqrt{g\ L_{WL}}}$	-
F_{rh}	Depth Froude Number	$\frac{V}{\sqrt{g\ D}}$	-
H_{35}	Mean increase of total head across pump and stator or several pump stages	-	m
H_{ij}	Head between station i and j	-	m
H_{JS}	Jet System Head	-	m
H_s	Local total head at station s	-	m
IVR	Inlet velocity ratio	$\frac{V_I}{V}$	-
JVR	Jet velocity ratio	$\frac{V_J}{V}$	-
K_Q	Torque coefficient	$\frac{Q}{\rho n^2 D^5}$	-
K_T	Thrust coefficient	$\frac{T}{\rho n^2 D^4}$	-
L_{OA}	Length overall	-	m
L_{WL}	Length waterline	-	m
$\dot{m}$	Mass flow rate (ρQ_J)	-	Kg/s
$\overline{M}_{is}$	Momentum flux at station s in i direction	-	N
N	Revolutions per minute	-	RPM
n	Revolutions per second	-	RPS
NVR	Nozzle velocity ratio	$\frac{V_J}{V}$	-
P_B	Brake power	-	W

P_D	Delivered Power to pump impeller	$\frac{P_{PE}}{\eta_{Pump}\,\eta_{Inst}}$	W
P_E	Effective power	$R_{TBH}V$	W
P_{JSE}	Effective Jet System Power	$E_7 - E_1$	W
P_{PE}	Pump effective power	-	W
P_S	Shaft power	-	W
P_{TE}	Effective thrust power	-	W
Q_{bl}	Volume flow rate inside boundary layer	-	m^3/s
Q_J	Volume flow rate through water jet system	-	m^3/s
R_{TBH}	Total bare-hull resistance	-	N
S_S	Wetted surface area	-	m^2
T_G	Gross thrust	$\rho Q_J\,(V_J - V_I)$	N
T_{JX}	Jet thrust in horizontal direction	-	N
T_{net}	Net thrust exerted by the jet system on the hull	-	N
T_q	Shaft torque	-	Nm
T	Draft	-	m
t	Thrust deduction fraction	-	-
u_{is}	Velocity component in i-direction at station s	-	m/s
u_s	Velocity at station s	-	m/s
V_0	Free stream velocity	-	m/s
V_I	Averaged ingested velocity at duct inlet	-	m/s
V_J	Averaged outlet velocity at the nozzle	-	m/s
V_{Pump}	Averaged axial inflow velocity at the pump entrance	-	m/s
V	Ship velocity	-	knots
w_{1A}	Width of capture area measured over hull surface at station 1A	-	m
w_1	Geometric intake width at station 1	-	m

w	Wake fraction	-	-
z_6	Vertical distance of nozzle centre relative to undisturbed surface	-	m

Chapter 1

Introduction

The main goal of the new series of highly efficient medium-speed wave-piercing catamarans is to reduce the environmental impact of fast sea transportation. Due to the requirement to decrease greenhouse gas emissions and the significant increase in fuel costs new ship designs must focus on reducing emissions and lowering fuel consumption instead of speed. Additional to these requirements there are new regulatory amendments to take into account forcing new vessel designs to reduce carbon dioxide (CO_2) emissions.

Initiated by Incat Tasmania, a leading manufacturer of high speed wave-piercing aluminium catamarans, this research project was established as a joint venture between then Australian Maritime College (AMC), University of Tasmania (UTAS), Incat Tasmania, Revolution Design Pty Ltd, Wärtsilä Corporation, and the Maritime Research Institute of the Netherlands (MARIN). The overall aim of the propulsion project was to determine optimal hull forms and propulsion systems for new series of medium-speed wave-piercing aluminium catamarans to be built by Incat Tasmania.

The propulsion project included a total of five PhD researchers of whom two were working on Computational Fluid Dynamics (CFD) investigations in regard to optimisation of medium-speed wave-piercing catamaran hull forms and waterjet propulsion modelling and three experimental researchers testing waterjet, propeller and paddlewheel propelled catamaran models. The content of this thesis is the waterjet propulsive performance estimation using a thrust based approach, extrapolation to full scale and validation with available powering sea trials data.

The new medium-speed catamarans will operate at speeds where mutual interference between waves and increased resistance produces the characteristic hump in the ships resistance curve. Usually waterjets are used for high-speed multihulls due to their high efficiency when operating at speeds beyond hump speed. However, they are generally not used for medium-speed applications due to the decrease in efficiency at lower speed. Therefore the challenge is to assess the effects of the change in operating conditions on the waterjet propulsion system.

The project sponsor, Incat Tasmania, plans to expand its fleet to medium-speed (i.e. 23-26 knots) wave-piercing catamaran ferries in a series of lengths in the 130-150 m range. Part of the propulsion project was an investigation to develop and optimise hull forms which will be efficient to operate at medium speeds. The new medium-speed vessels are to operate largely in the length Froude number range of 0.3 to 0.5, and this is the critical speed range where wave making resistance tend to dominate over frictional resistance and where small increases in speed result in large increase in resistance. Significant changes in running trim and associated resistance are a result of trim issues in the zone due to changes in speed. This hump speed range is usually bypassed and so the required hull form characteristics for multihulls to operate in this zone are not well understood and all project related research regarding medium-speed hull form optimisation for wave-piercing catamarans is discussed in Haase (2015).

In order to make contract specification speeds, the accurate prediction of the full scale powering requirements is critical for the medium-speed range. The need for reliable extrapolation methods to be developed for the estimation of propulsive performance of medium and high-speed multihulls was recognised by the international marine testing community as discussed in Campana et al. (2008). Extrapolation in traditional methods for model-to-ship make underlying assumptions about the flow for which experience was gained through the use of linearized correlation factors. These methods are insufficient to accurately assess their capabilities and energy saving potential when applied to unconventional vessels and propulsors, such as high-speed catamaran ferries. Using different methods for powering estimates and energy saving potential of a given system lead to large variations, up to 20% as discussed in Bose (2008). Part of the overall medium-speed propulsion project was to assess the effect of the change in operating conditions on the propulsion systems: propellers and waterjet. High-speed multihulls currently use waterjet as propulsors due to their high efficiency when operating at speeds over 30 knots.

This project looked into the determination of the more applicable propulsion system for medium-speed catamarans by comparing propeller and waterjet test results on similar catamaran hulls. For waterjet propulsion a baseline test, using a model of the 98 m Incat catamaran ferry HSV-2 *Swift* (Figure 1.1), was carried out to establish a methodology for waterjet self-propulsion testing in the Australian Maritime College (AMC) towing tank, and to create a method for data reduction and extrapolation as discussed in Zürcher et al. (2013). To verify experimental results, a set of combined standardization and powering trials results data was used conducted by the Naval Surface Warfare Center Carderock Division (NSWCCD) in March 2005 for the Incat 98 m wave-piercing catamaran HSV-2 *Swift* as discussed in Griggs et al. (2005).

Figure 1.1: 98 m Incat wave-piercing catamaran HSV-2 *Swift*.

An in depth comparison and discussion of the propeller and waterjet results in relation to applicability the medium speed catamarans is given in Kamal (2015), and a compressed discussion of the same comparison is given in Section 5.3 of this thesis. The discussion about the better propulsion system for medium-speed catamarans is not solely based on powering performance and efficiency but has to take into account other aspects such as hull forms, vessel draft, space available for required propulsion machinery and customer preferences.

This chapter introduces the aim and motivation, scope, contribution to research, general methodology of the project, and outlines the main parts of the thesis.

1.1 Motivation

The aim of this research was the development and validation of a simplified, thrust based, waterjet propulsion test to determine power requirements for a medium-speed wave-piercing catamaran using model testing, and the availability of such a method would allow faster model testing of new medium-speed catamaran hull forms.

Based on recommendations for propulsion tests given by the International Towing Tank Conference (ITTC), thrust should be based on indirect measurement of thrust by measuring velocity or flow rate at the waterjet nozzle or direct measurement of thrust. As direct measurements of thrust were not possible in the testing facilities used for this study, an indirect method to establish thrust was used in the form of a static flow measurement test (measuring captured mass of water as a function of time) which was connected to the waterjet propulsion test by a reference measurement at the nozzle as proposed by van Terwisga (1996). The waterjet propulsion testing was based on recommendations given by ITTC as well as other

published work about waterjet testing techniques such as Rispin (2007). Additional investigated parameters for the waterjet propulsion included wake fractions, based on boundary layer measurements, and thrust deduction fractions, based on thrust and bare-hull resistance measurements. The major motivation of this thesis was to reduce testing required for waterjet powering performance estimation of a wave-piercing catamaran and therefore, decrease time and effort required for experimental testing. This was achieved by using a simplified, thrust based testing and extrapolation method and validate results with a set of full scale powering sea trials data. An additional aim of the research was to compare waterjet and propeller propulsion for medium-speed wave-piercing catamarans and give recommendations to Incat Tasmania as to which of the two propulsion system is more applicable. As a benefit for other team members working on the propulsion project, the experimental resistance and propulsion results gained from the waterjet model testing allow for validation of Computational Fluid Dynamics (CFD) investigations discussed in Haase (2015) for resistance optimisation of medium-speed wave-piercing catamaran hulls and waterjet propulsion modelling.

1.2 Scope

A variety of testing techniques for waterjet propulsion were used in the investigation. The significant work which defines the scope of the project is outlined below and consists of model testing, analysis, comparison/validation using full scale sea trials data, and comparing results to propeller propulsion results of a similar, other, Incat wave-piercing catamaran. As a result of an industrial relationship between the Australian Maritime College, University of Tasmania, Incat Tasmania, Wärtsilä Corporation, and the Maritime Research Institute of the Netherlands (MARIN) an opportunity arose to carry out model testing of a waterjet propelled Incat wave-piercing catamaran.

Bare-hull resistance, flow rate measurement, and propulsion tests were carried out and data used for comparison to full scale sea trials data. A model waterjet was designed and manufactured, with the waterjet tunnel geometry scaled from an appropriate full scale unit, for use in the model propulsion tests. Computational work was carried out as part of the overall propulsion project by another member of the project team, Max Haase, and results of experimental resistance and propulsion testing were used for Computation Fluid Dynamic (CFD) validation and discussed in Haase (2015).

1.3 Contribution to Research

The research results presented in this thesis contribute by creating an additional set of experimental waterjet powering results and promoting a new, simplified thrust based extrapolation

method for waterjet performance estimation. Generally recommended methods for waterjet propulsive performance estimation are given by the International Towing Tank Conference (ITTC) Specialist Committee on Waterjets and consist of multiple tests to establish accurate performance predictions.

The thrust based extrapolation method introduced in this study (see Chapter 6) allows the determination of power requirements using reduced testing compared to the ITTC based method, with the drawback of lowered accuracy (due to higher uncertainty) of results (see Section 4.6.10 and Section 5.2), but faster turnaround for series testing of waterjet propelled models.

The new, thrust based extrapolation method is thought to serve as an example of the new method and to start a discussion in the propulsion community about advantages, disadvantages and possible improvements. The presented waterjet powering results can be used for validation purposes and the description of the experimental testing as reference for future waterjet testing at the Australian Maritime College (AMC), or by any other researchers, looking into testing waterjet propelled models in a towing tank.

A detailed uncertainty analysis was undertaken for the three experimental tests carried out for the waterjet performance estimation research: bare-hull resistance test, flow rate measurement test, and waterjet self-propulsion test. Uncertainty analysis results for the three mentioned tests are given in Sections 4.4.10, 4.5.5, and 4.6.11. Descriptions of the detailed uncertainty analysis methodology used for the three tests is given in Sections D.1, D.1, and D.1 of Appendix D. This new set of uncertainty results can be used for comparison and validation purposes for future waterjet testing, or testing carried out by other researchers.

1.4 Methodology

For the research presented in this thesis, experimental testing was carried out using a waterjet propelled single catamaran demihull scaled from a 98 m wave-piercing catamaran. Waterjet self-propulsion testing was carried out for performance estimations, and extrapolated full scale results were validated using available full scale powering sea trials results for the tested vessel. Three different model tests were undertaken as follows

1. Bare-hull resistance test to identify hump speed region for waterjet self-propulsion test speed range.

2. Static flow rate measurement test to determine flow rates of waterjet pump. The static flow rate measurement test was connected to the self-propulsion test by a reference measurement recorded at the outlet of the waterjet nozzle.

3. Waterjet self-propulsion test for waterjet powering performance in hump speed range.

A detailed experimental methodology outlining waterjet propulsion, test conditions, extrapolation, data reduction methodology, and an overview of instrumentation systems used for the experimental testing of the project is given in Chapter 3. Experimental testing of the bare-hull testing is detailed in Section 4.4, static flow rate measurement testing in Section 4.5, and waterjet self-propulsion testing in Section 4.6. Validation and comparison of the extrapolated experimental testing results with full scale powering sea trials data is discussed in Chapter 5. The performance evaluation was carried out on a thrust basis and the method is outlined in detail in Chapter 6.

1.5 Outline of this Thesis

In Chapter 2 waterjet propulsion systems are discussed in detail as well as capture area, control volume, thrust and waterjet pump characteristics. The momentum flux method is discussed as well as thrust deduction, wake fraction, and thrust breakdown. Also given is an overview of the forms of resistance and scaling laws which include geometric, kinematic, dynamic similarities as well as Froude and Reynolds numbers. The chapter concludes with a literature review of previous research carried out for the subject of waterjet performance assessment.

Chapter 3 deals with the experimental methodology used in the experimental testing carried out for the research presented in this thesis. The content of this chapter includes discussions about model waterjets, test conditions, extrapolation, data reduction, instrumentation systems, and estimates for the expected errors of the instruments used for experimental testing.

Chapter 4 shows detailed analysis of the experimental testing carried out for the waterjet propulsion research. The tests described here include bare-hull resistance test, static flow rate measurement test, and waterjet self-propulsion test. Each test is shown in its own section which includes test setup and instrumentation, test program, analysis, and discussion of results. A short overview of the model used for testing is given but a more detailed discussion of the model building process is presented in Appendix A and the model waterjet propulsion is outlined in Appendix B.

A comparison and validation of extrapolated results from model testing to full scale powering sea trials data is shown in Chapter 5. As discussed in the introduction of Chapter 1, model testing of a propeller propelled catamaran was carried out at the same time as the waterjet propulsion testing and a comparison of overall propulsive efficiency and powering results is given in the last section of Chapter 5.

Chapter 6 introduces a thrust based extrapolation method using just the results of the

waterjet self-propulsion test to estimate waterjet powering performance. This method is presented to start a discussion in the waterjet propulsion community to establish a simple method for waterjet performance estimation to allow faster series model testing.

Chapter 7 presents the conclusions of the presented research and recommendations for future waterjet propulsion testing which are based on experiences gained while carrying out the experimental testing for the research presented in this thesis.

Chapter 2

Background

Discussed in this chapter are the basic principles of waterjet propulsion. Equations of waterjet propulsion performance are based on descriptions of pump performance using standard nomenclature. Nomenclature of commonly used propeller theory will be mentioned as a reference where possible. In the first section, an introduction to waterjet propulsion is given, which explains the main principles and key features of this type of propulsion system. The second section outlines the waterjet capture area, control volume, thrust, and waterjet pump. In the third section momentum flux theory is introduced. The contents of the fourth to sixth sections are thrust deduction, wake fraction, and thrust breakdown. The seventh section describes forms of resistance outlining frictional resistance, wave making resistance, and air resistance. Section eight discusses dimensional analysis, scaling laws (i.e. geometric, kinematic, and dynamic similarity), length Froude number, and Reynolds number. The chapter, concludes with a literature review of previous research carried out for the subject of waterjet performance estimation, waterjet/hull interaction, and published waterjet testing techniques.

2.1 Introduction to Waterjet Propulsion

Waterjet propulsion has been continuously developed since it entered marine industry as a serious ship propulsion alternative in the 1950s. Waterjet propulsion works in a similar manner to conventional screw propeller propulsion in that fluid is accelerated by the propulsor so as to provide a net thrust on the propulsor and the main principles of a waterjet are:

- Impeller draws in seawater through an inlet;
- Impeller adds head (i.e. pressure) to the water flow;
- When water is pushed through the nozzle the nozzle converts the water pressure into a high-speed jet;
- Acceleration of the water flow generates a thrust force that pushes the vessel forward;

- For sailing astern, water flow exiting from the nozzle can be reversed in the forward direction using a reverse plate or reverse section (also called bucket).

A significant difference is that the propeller is replaced by a pump which is located within the vessel and ducting carries water to and from the pump. The concept of accelerating water to provide a usable, forward thrust by using an internal pump is not a new idea and was around for quite some time and an overview of previous research is discussed in Section 2.9. Many small to medium waterjets can be coupled directly to the engine without the need for a gearbox and waterjet units are often delivered as a complete package which includes steering and reversing systems.

In the last 100 years there was a tendency to use marine screw propellers rather than waterjet propulsion; the reason for this was that the design and production of screw propellers was simpler and more details about historical waterjet development are given in Roy (1994) and Allison (2001). The introduction of more efficient pumps used in waterjet systems has changed this tendency. Today there are specific characteristics of the waterjet propulsion that make this type of propulsion system a better choice compared to conventional marine screw propellers and this includes higher achievable speed, better efficiency at high speed, better manoeuvrability, low drag, shallow draft, safety, lower noise levels, and lower underwater acoustic signature.

As there are no appendages such as rudder, struts, etc. the shallow draft of the waterjet propulsion system allows vessels to operate in shallow water. However, debris and mud might be sucked into the system and cause damage to the pump system. Appendage drag can be as much as 20%, as discussed by van Terwisga (1996), of the bare-hull resistance at high speed but there is no such component for waterjet propelled vessels.

Cavitation characteristics are different for waterjet and propeller systems. For waterjet propulsion systems cavitation occurs at higher velocities due to increased pressure inside the waterjet system. Because of this, when efficiency of screw propellers diminishes, waterjet propulsion is a better choice. Due to the heavier weight of waterjet propulsion systems compared to conventional screw propellers these systems are more applicable as propulsion system on larger vessel such as wave-piercing ferries.

Today, waterjet systems are available in many different variations and sizes and a variety of manufacturers and waterjet propulsion systems are used for fast passenger ferries, work boats, rescue craft, patrol craft, pilots boats, pleasure cruisers, and fishing boats.

2.2 Capture Area, Control Volume, Thrust and Pump

Waterjet systems can be divided simply into a pump and a ducting system. The pump converts the mechanical power (input) into hydraulic power (output). The ducting system leads the flow through the exterior to the pump and through the nozzle back to the environment. Standard locations for the flow, as defined by the International Towing Tank Conference (ITTC), are indicated in Figure 2.1, where the inflow capture area is marked as station 1a which is located one inlet diameter ahead of the inlet tangency. References to momentum flux stations throughout this thesis are, when not otherwise stated, referring to the ITTC momentum flux station definition as shown in Figure 2.1.

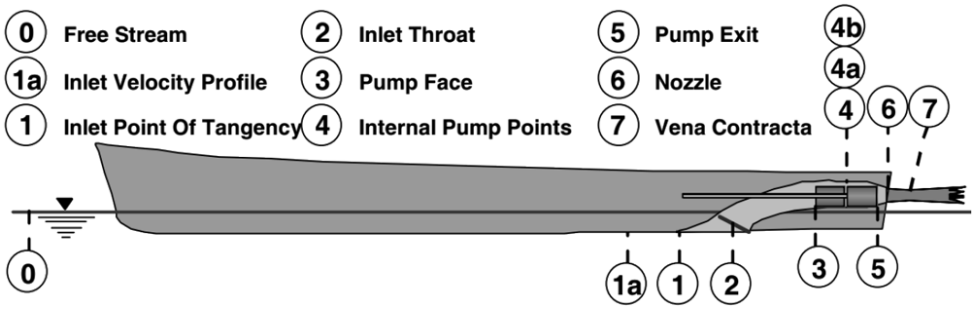

Figure 2.1: Control volume representing the hydrodynamic model of the waterjet as defined by ITTC (2002) showing momentum flux stations 0 to 7.

Processes throughout the system are presented in relation to the seven stations shown in Figure 2.1 and discussed by the 23rd ITTC Specialist Committee on Validation of Waterjet Test Procedures in ITTC (2002) as follows:

- **Station 0:** Far ahead of the ship in undisturbed flow. Water flows free with a speed matching the speed of the boat through water.
- **Station 1:** Stream tube inlet at one inlet width upstream of inlet tangency point. Part of the flow below the hull which enters the waterjet system. At this location the average velocity is smaller than at station 0 due to the boundary layer built up on the keel. The cross sectional area is typically modelled as a rectangle with 1.3 times the width of the duct pipe diameter and a height determined by the mass flow rate through the waterjet, as described in ITTC (1996) and van Terwisga (1996).
- **Station 2:** Duct inlet at the aft lip of the waterjet inlet. At this location the water enters the propulsion system.
- **Station 3:** Pump inlet just ahead of the pump blade tips. The wake field entering the pump is defined at this location, and depending on the operation of the vessel, the pressure can be lower or higher than the pressure at station 1. The pressure at

this point is dependent on the vessel speed, the mass flow rate, and the pressure loss experienced in the duct inlet (station 2).

- **Station 4:** Pump centre between pump rotor and stator. At this location, right after the rotor, the static pressure is at its maximum, the flow is rotational, but with the same average axial velocity as at station 3.

- **Station 5:** Pump outlet just aft of the pump stator. Running from station 4 to 6 guide vanes are installed, transforming static pressure into a dynamic pressure as the water is accelerating through the nozzle. Head rise is reduced by the guide vanes to produce a specific thrust and recovering some of the energy bound in the rotational flow.

- **Station 6:** Nozzle outlet plane. Here the accelerated jet flow leaves the propulsion system.

- **Station 7:** Jet maximum vena contracta where static pressure is near ambient in the jet. The stream continues to contract after leaving the nozzle (at station 6) which is due to the vena contracta phenomena discussed in ITTC (2005b). At this location the diameter of the waterjet is at its minimum and this location is considered the end point of the propulsion system. The maximum average velocity is reached at this location and the thrust of the waterjet propulsion system is determined.

The cross sectional area of a waterjet propulsion unit and the control volume usually applied for a waterjet system analysis is shown in Figure 2.2, where the numbering of the surface areas are the same as introduced by van Terwisga (1996).

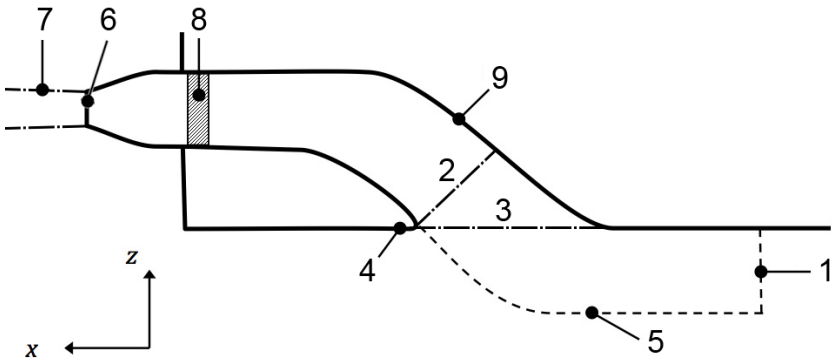

Figure 2.2: Waterjet control volume as a cut through the ducting system.

The numbered surface areas can be broken down as follows:

- **Surface 1:** Capture area. ITTC (2005a) locates this surface as "far enough in front of the intake ramp tangency point, before inlet losses occur" and as a practical solution recommends one inlet diameter ahead of the inlet tangency point. The main reason for

selecting this area for the capture area is to avoid major flow distortions caused by the intake geometry.

- **Surface 2:** Intake throat where the sectional area of the channel is the smallest
- **Surface 3:** Surface covering the waterjet inlet opening
- **Surface 4:** Outer lip surface
- **Surface 5:** Dividing stream tube. Imaginary Surface which separates the flow drawn into the ducting system from the rest of the flow field and is defined by the stagnation stream line from the lip surface.
- **Surface 6:** Nozzle discharge area
- **Surface 7:** Vena contracta
- **Surface 8:** Boundary area of the pump control volume
- **Surface 9:** Waterjet system internal material boundary

A basic overview of the main components found in a waterjet propulsion unit is given in Figure 2.3 which also shows the most important velocities which are the inlet velocity (V_I), pump velocity (V_{Pump}), and jet velocity (V_J).

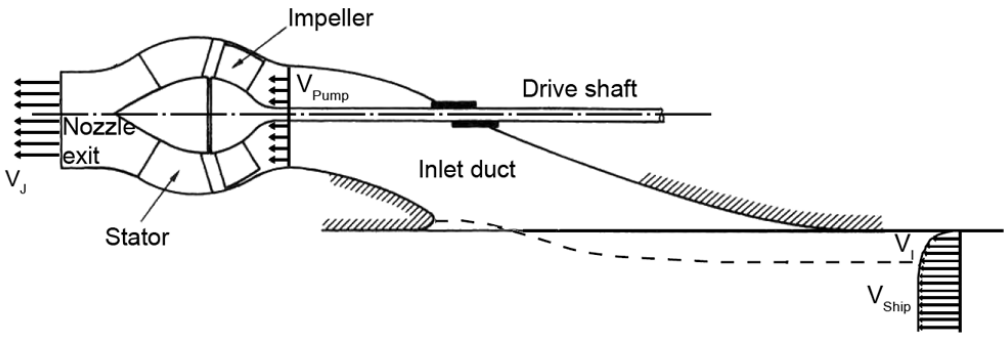

Figure 2.3: Main components of a waterjet propulsion unit with indicated inlet, pump, outlet, and ship velocities as well as stator, impeller and inlet duct.

Thrust describes the force a waterjet system produces on a vessel and thrust is defined as forward acting force produced by propelling water backwards. Newtons third law is followed by the system by exceeding a force on the water in the waterjet which then exerts a force on the waterjet system which is then transferred to the vessel, propelling it forward. A basic thrust equation is defined in Allison (1993) and shown in Equation 2.1, where V_1 and V_7 are the average axial velocities at stations 1 and 7 (see Figure 2.1), $\dot{m}$ is the mass flow rate, ρ is the fluid density, Q_J is the volumetric flow rate, and T is the produced thrust. If the jet velocity (V_7) is kept constant, thrust is reduced when increasing the vessel speed (V_0). This

is due to the dependency of the stream tube velocity (V_1) on the vessel velocity through the water. Thrust produced at zero speed is defined as Bollard pull and represents the maximum pulling force a waterjet propulsion system can produce at a specific rotational speed and torque.

$$T = \dot{m}\,(V_7 - V_1) = \rho Q_J\,(V_7 - V_1) \tag{2.1}$$

The waterjet pump is the main component of the propulsion system. In the pump the energy is transferred from the engine to the water through the propeller blades. Many waterjet pumps consist of two stages; the nozzle stage, in which the guide vanes are integrated (see Figure 2.4), and the impeller stage.

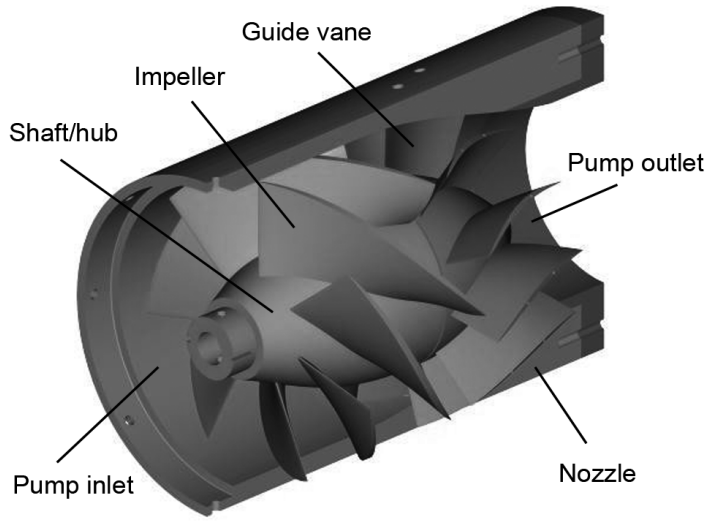

Figure 2.4: 3D representation of a typical stock waterjet showing guide vanes (stator), impeller, waterjet nozzle, shaft/hub, and pump inlet and nozzle (outlet).

The impeller rotation adds energy to the fluid, creating a pressure rise and sustaining the flow rate of the waterjet system by counteracting the pressure loss throughout the system. Due to a high degree of swirl introduced by the rotating impeller, the static pressure is high after the impeller. Water accelerated though the nozzle transforms high static pressure to dynamic pressure (kinetic energy). The transformation from static to dynamic pressure is achieved by narrowing the nozzle and streamlining the flow in the axial direction using the guide vanes. Extra friction is introduced by the guide vanes, but the streamlining of the flow reduces the required head rise (by the conversion of swirl to axial flow) so that the overall pump efficiency is increased. Bounds in the swirl after the nozzle results in lost energy as it does not contribute to the propulsion of the vessel.

2.3 Momentum Flux Method

Earlier attempts to develop techniques for predicting performance of waterjet propulsors involved applying techniques used for conventional marine screw propellers. As a waterjet is an integral part of the hull, some of the traditional concepts such as thrust deduction are difficult to apply to waterjet propelled ships in a physically obvious way. Measurements of some basic quantities, particularly thrust, are difficult in practice and require an indirect measurement method based on flow rates. For this reason, a different approach was devised for performing model tests on waterjets and waterjet propelled vessels and this approach is called the momentum flux method. The momentum flux method is described in the Final Report and Recommendations to the 21st ITTC Waterjet Group and is based on the laws of conservation of momentum, energy and continuity.

The momentum flux method is used mainly in the analysis of the steady state behaviour of a waterjet and momentum flux is defined as the measure of the momentum in a quantity of fluid which crosses a unit area of a given surface in a unit of time. To calculate power and internal losses energy flux is used, which is similar but is the measure of the energy in the fluid. The locations where energy and momentum flux are measured correspond to the stations discussed in Section 2.1.

The propulsion concept of waterjets is based on the thrust force achieved through the momentum flux change through the system where low speed velocity enters the system through the capture area. The pump inside the ducting channel adds momentum to the entrained water and the now high-speed jet is discharged though the nozzle. The momentum flux balance for a control volume gives the resultant force acting on this control volume. Generally, momentum flux vector (M) in i direction over a control volume is defined as Equation 2.2, where ρ is the fluid density, u is the velocity vector and n is the unit vector normal to the control volume surface.

$$\overline{M}_i = \iint_A \rho \, u_i \, (u_k \, n_k) \; dA \tag{2.2}$$

2.4 Thrust Deduction

Using conventional naval architecture analysis, ship resistance with an active propeller is found to be different from the bare-hull resistance. A low pressure region is created, due to the action of the propeller, which results in increased drag of the vessel. The difference between the bare-hull resistance (R_{BH}) and the required thrust is given in terms of the thrust deduction factor (t) according to Equation 2.3, where R_{BH} is bare-hull resistance and T is required thrust at a certain ship speed. The thrust deduction is always positive for a

propeller, which increases ship resistance due to the action of the propeller and therefore a higher required thrust. The propulsive device accelerates the flow ahead of itself, thereby increasing the rate of shear in the boundary layer (therefore increasing the frictional resistance of the hull) and reducing pressure (i.e. Bernoulli) over the rear of the hull and therefore increasing the pressure resistance.

$$R_{BH} = (1 - t)\, T \tag{2.3}$$

Additionally, if separation occurs in the after body of the hull when towed without a propeller, the action of the propeller may suppress the separation by reducing the pressure gradient of the after body of the hull. Usually the resistance of the hull is increased by the action of the propeller by an amount that is approximately proportional to thrust and this means that the thrust will exceed the bare-hull resistance. Physically this is best defined as a resistance augment, but in practise it is taken as thrust deduction.

In waterjet propulsion analysis, the thrust deduction factor (t) can be used to account for the effects of the neglected surface forces such as the force on the region after of the waterjet inlet and the force on the stream tube as well as a change in pressure distribution along the hull. This approach was used by van Terwisga (1996) as well as by Eslamdoost (2014) where the thrust deduction fractions t_r and t_j were introduced. Linking up with existing propeller hydrodynamics nomenclature, resistance increment is referred to as the hulls thrust deduction fraction (t_r) and the corresponding thrust deduction factor may be defined as the ratio of the bare-hull resistance to the net thrust of the waterjet system as shown in Equation 2.4.

$$t_r = 1 - \frac{R_{BH}}{T_{Net}} \tag{2.4}$$

Thrust deduction fraction is built up from the jet thrust deduction fraction (t_j) and the hull's resistance increment (t_r) as shown in Equation 2.5, where R_{BH} is bare-hull resistance, T_{Net} is net thrust, and T_G is gross thrust.

$$t = t_r + t_j - t_r \times t_j = \left(1 - \frac{R_{BH}}{T_{Net}}\right) + \left(1 - \frac{T_{Net}}{T_G}\right) - \left(1 - \frac{R_{BH}}{T_{Net}}\right) \times \left(1 - \frac{T_{Net}}{T_G}\right) \tag{2.5}$$

Research presented in van Terwisga (1996) and ITTC (2005a) stated that jet thrust deduction fraction (t_j) is negligibly small except at the transom clearance Froude number and the second order term on the right side can be neglected to give thrust deduction fraction as $t = t_r + t_j$. Eslamdoost (2014) stated that the second order term in Equation 2.5 cannot be neglected when the nozzle exit is not ventilated. For higher ship speeds the momentum flux change through the waterjet system can be a good measure for the resistance increment of the hull since t_j is normally much smaller than t_r.

2.5 Wake Fraction

Due to the boundary layer under the hull shown in Figure 2.5, the water entering the waterjet inlet beneath the vessel is travelling slower than the free stream velocity (i.e. ship speed). As less power is required to accelerate the water to get the same momentum change and thrust, this is improving the performance to a small degree.

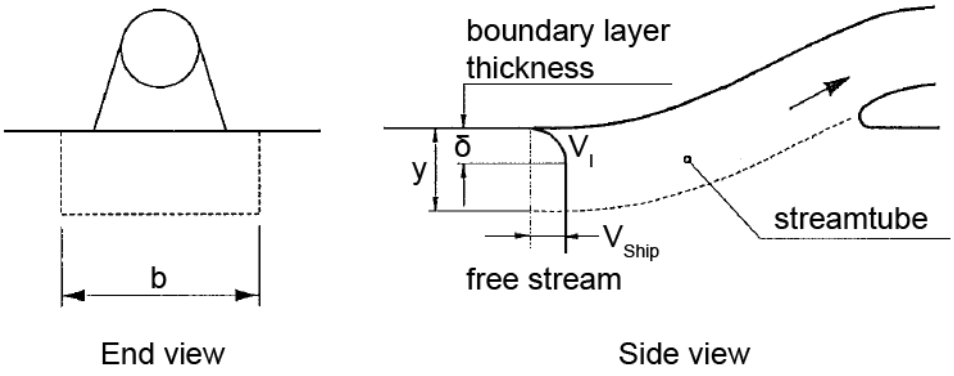

Figure 2.5: Hull boundary layer where V_{Ship} defines the free stream or ship speed, V_I the inlet speed, b the inlet width, and δ the boundary layer thickness.

To achieve this modification, a new velocity is defined called inlet velocity (V_I) as the momentum average velocity of water entering the intake to provide the same momentum as the flow with its boundary layer shown in Equation 2.6, where w is the wake factor.

$$V_I = (1 - w)\, V \tag{2.6}$$

Approximations for the inlet velocity can be found using standard boundary layer theory taking into consideration that this does not account for effects such as the longitudinal pressure gradient and its effect on boundary layer growth below the hull. In theory it is assumed that the stream tube has a rectangular cross section with a height of y and a width of b but in practice the stream tube is likely to be elliptical.

Assuming a power law velocity profile with a local velocity of V within the turbulent boundary layer, as described by Coop (1995), boundary layer thickness (δ) for n=7 can be calculated using Equation 2.7, where δ is boundary layer thickness, and R_e is Reynolds number.

$$\delta = \frac{0.371}{(R_e)^{0.2}} \tag{2.7}$$

Using Equation 2.7 will result in a numerical estimate for the boundary layer thickness (δ), which can also be determined experimentally as it was done for this project and is described in detail in Section 4.6.3. The velocity profile can then be calculated using Equation 2.8, where δ is boundary layer thickness, y is depth of ingested flow, and n is the power law index.

$$\frac{V}{V_s} = \left(\frac{y}{\delta}\right)^{\frac{1}{n}} \tag{2.8}$$

Using Equation 2.8 flow rate (Q_J) is equal to:

$$\begin{aligned} Q_J &= \int_0^{\delta} V\,dy + (y-\delta)\,b\,V_s \\ Q_J &= b\,V_s \int_0^{\delta} \left(\frac{y}{\delta}\right)^{\frac{1}{n}} dy + (y-\delta)\,b\,V_s \\ Q_J &= \frac{b\,V_s}{\left(\frac{n+1}{n}\right)}\delta + (y-\delta)\,b\,V_s \\ Q_J &= b\,V_s\left(y - \frac{\delta}{n+1}\right) \end{aligned} \tag{2.9}$$

Rearranging Equation 2.9 to give depth of ingested flow (y) in terms of the flow rate (Q_J) where n is the power law index, 7 for model scale and 9 for full scale as discussed by Bulten (2006), MARIN (2008) and Duerr et al. (2014), in the velocity profile:

$$y = \frac{Q_J}{b\,V_s} + \frac{\delta}{n+1} \tag{2.10}$$

For $y/\delta >= 1$:

$$\frac{V_i}{V_s} = \frac{\frac{n}{n+2} + \frac{y}{\delta} - 1}{\frac{n}{n+1} + \frac{y}{\delta} - 1} \tag{2.11}$$

For $y/\delta < 1$:

$$\frac{V_I}{V_s} = \frac{n+1}{n+2}\left(\frac{y}{\delta}\right)^{\frac{1}{n}} \tag{2.12}$$

The wake factor (w) is related to ship speed (V_s) and inlet speed (V_I):

$$w = \frac{V_s - V_I}{V_s} \tag{2.13}$$

Usually, the depth of ingested flow is greater than the boundary layer thickness (i.e. $y/\delta > 1$). Using this assumption, equations can be derived to give w in terms of the jet velocity ratio (JVR) where JVR=V_s/V_J (assuming V_J=V_n so that vena contracta appears at the nozzle exit plane):

$$\frac{V_I}{V_s} = \frac{\frac{n}{n+2} + \frac{y}{\delta} - 1}{\frac{n}{n+1} + \frac{y}{\delta} - 1} \tag{2.14}$$

Depth of ingested flow (y) becomes:

$$y = \frac{Q_J}{b\,V_s} + \frac{\delta}{n+1} \tag{2.15}$$

Flow rate (Q_J):

$$Q_J = A_n\,V_n \tag{2.16}$$

Putting it all together:

$$y = \frac{A_n}{b\,JVR} + \frac{\delta}{n+1} \tag{2.17}$$

Using substitution:

$$\frac{V_I}{V_s} = \frac{\frac{n}{n+2} + \frac{A_n}{b\,\delta\,JVR} - \frac{n}{n+1}}{\frac{n}{n+1} + \frac{A_n}{b\,\delta\,JVR} - \frac{n}{n+1}} \tag{2.18}$$

Assuming a power law index of $n = 7$ and inlet stream width equal to b, wake factor can be calculated using:

$$w = 1 - \frac{V_I}{V_n} = \frac{7}{72}\frac{b\,\delta\,JVR}{A_n} \tag{2.19}$$

Using the stated equations, wake factor (w) can be calculated for a known intake and jet unit geometry. The net effect of the wake factor is to increase the thrust from the value predicted using simple theory with no wake factor, or to increase the expected unit efficiency for a given thrust.

2.6 Thrust Breakdown

Head rise, torque and efficiency levels are cavitation dependent. Under highly cavitating conditions head rise, torque and efficiency decrease. The point where these quantities drop off is called thrust breakdown; but the phase thrust breakdown is a misnomer as thrust is not considered.

Thrust breakdown is often defined as the point at which the pump efficiency drops by 1% due to cavitation, a 3% drop in head rise, or a 1% drop in torque which only occurs at very low pressure. The percentage declines are related to the baseline head rise, torque, and efficiency at non-cavitating conditions. The cavitation coefficient is recorded throughout breakdown and is, as discussed in Marquardt (2011), expressed as:

$$N^* = \frac{p_{t3} - p_v}{\rho\, n^2\, D^2} = \frac{g\, NPSH}{n^2\, D^2} \tag{2.20}$$

Where $N*$ is the cavitation coefficient, p_{ts} is total pressure at momentum flux station 3 as defined by ITTC in Figure 2.1, p_v is the vapour pressure of water, n is revolutions per second (RPS), D is inlet diameter, and Net Positive Suction Head (NPSH) which is given by:

$$NPSH = \frac{p_{t3} - p_v}{\rho\, g} \tag{2.21}$$

A complete thrust break down due to an extreme drop in pump efficiency occurs shortly after and this is due to excessive cavitation in the pump. Thrust breakdown is estimated using the low pressure area on the impeller, a margin is defined as how much the static pressure at the pump inlet can be lowered before a certain low pressure area is reached and this margin varies from pump to pump and is based on Computational Fluid Dynamics (CFD) computations or experimental results.

2.7 Forms of Resistance

Resistance of a ship at a given speed is the force required to tow the ship at that speed in calm (smooth) water. If there are no appendages on the hull, this is called bare-hull or "towing" resistance, and although very near to, it is not exactly the same as the propulsion resistance (see Section 4.6.8) due to hull/propulsor interaction. Total resistance is made up of several different components, as shown in Figure 2.6, which are caused by a variety of factors and interact with each other in a rather complex fashion.

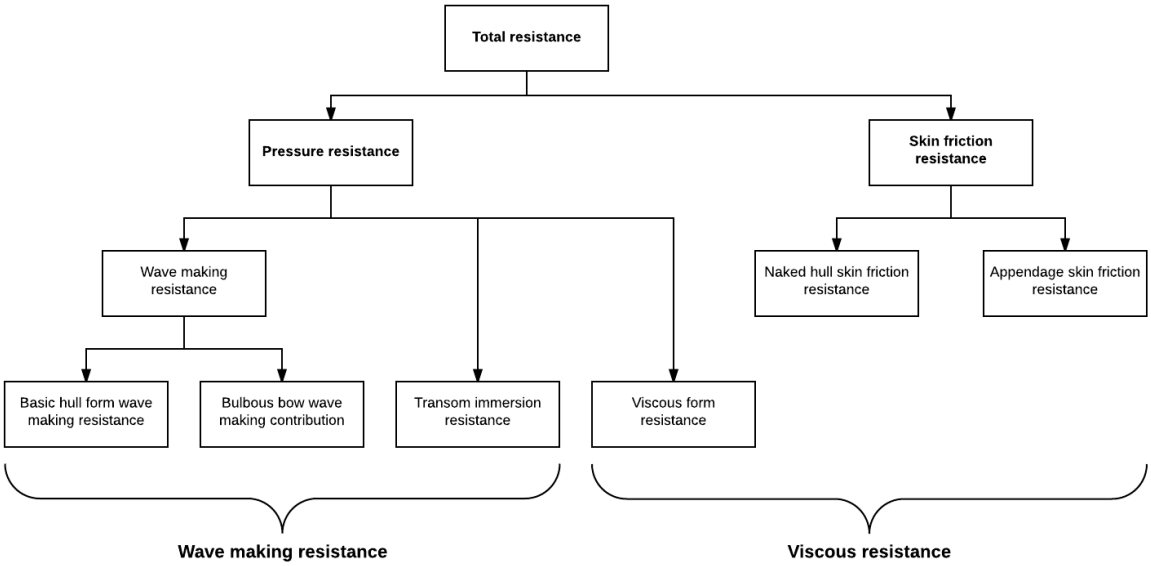

Figure 2.6: Resistance components of wave making and viscous resistance.

Calm water resistance is considered to be made up of four main components:

1. Frictional resistance due to the motion of the hull through the viscous fluid.
2. Wave making resistance due to the energy that must be supplied continuously by the ship to the wave system created on the free surface.
3. Eddy resistance due to the energy carried away by eddies shed from the hull or appendages. This is more severe at the stern where the water may be unable to follow the curvature and will break away from the hull and giving rise to eddies and separation resistance.
4. Air resistance experienced by the above water part of the main hull and the superstructure due to motion of the ship through the air.

Resistance under (2.) and (3.) are commonly considered together, despite the fact that they arise from different physical mechanisms, under the name residuary resistance. A variety

of other forms of resistance exists such as added resistance due to waves, wave breaking resistance for a ship sailing in a seaway, and added resistance due to turning but they will not be discussed in any detail here as experimental testing was carried out in calm water conditions only.

The simplest form of resistance consists of a streamlined body moving in a straight line at constant forward speed, deeply immersed in an unlimited ocean. As there is no free surface, there is no wave formation and therefore no wave making resistance. Velocity distribution (i.e. for an ideal fluid) past the hull will be greater than the speed of advance along the mid-portion, and in the region of bow and stern will be less. Pressure distribution, derived from Bernoulli's law, will follow the inverse pattern: higher at the bow and stern and lower in the middle. Since the fluid is assumed to be without viscosity, pressure forces will everywhere be normal to the hull and it can be shown that they will cancel out each other and the body will experience no resistance referred to as hydrodynamic or D'Alembert's paradox as discussed in Harvald (1991).

In a real fluid the boundary layer alters the virtual shape and length of the body, pressure distribution at the stern is changed and its forward component is reduced, and in this case there is a net force on the body acting against the motion, giving rise to a resistance which is referred to as form drag or viscous pressure drag. The body also experiences frictional resistance as well as eddy resistance. Fluid immediately in contact with the surface of the body is carried along with the surface, and the fluid in the close vicinity is set in motion in the same direction as the fluid in which the body is moving and this develops in a boundary layer which gradually gets thicker from the bow to the stern. Here the velocity varies from that of the body at its surface to that appropriate to the potential flow pattern at the outer edge of the boundary layer and the momentum supplied to the water in the boundary layer, by the hull, is a measure of the frictional resistance. If a body is used with a blunt after end the flow may detach at some point, which is called the separation point, so reducing the total pressure on the after body and adding to the resistance.

2.8 Scaling Laws

Towing tank testing of a ship model is the traditional method to determine a ship's total resistance. For this method, a model is towed in a towing tank measuring hull resistance for a series of speeds. Model scale resistance results are then extrapolated to full scale hull resistance. When using physical models, it must be ensured that results are transferred correctly from model to full scale. Complete similarity between the two states is often not possible, and a system of laws to maintain similarity between the most significant elements of model and full scale is required.

Dimensional analysis can be used to derive groups of meaningful dimensionless quantities for applicable variables. This is useful for complex problems. Typically all the different quantities assumed to be important for a certain phenomenon are listed. A functional relationship between the different groups of parameters is established for all flow governing quantities and scaling laws are then obtained by considering the ratio of the different forces. A detailed description of dimensional analysis can be found in Taylor (1974) and a comprehensive discussion about model laws is given by Chakrabarti (1998).

To achieve similarity in forces between the model and the full scale situations the following conditions must be met:

- Geometric similarity
- Kinematic similarity
- Dynamic similarity

In the following sections these requirements will be discussed in more detail.

2.8.1 Geometric Similarity

By requiring a constant scale factor between model and full scale ship, geometric similarity assures that full scale and model scale ships are geometrically similar. The model scale factor (λ) is defined as the ratio between length in model and full scale:

$$\lambda = \frac{L_s}{L_m} \tag{2.22}$$

This requirement is also valid for the environment surrounding the model and ship as well as the elastic deformations. This implies that water depth, waves and hull roughness are to be modelled with the same scale factor. From the geometric similarity follows that the ratio of areas is equal to the factor squared and the ratio of volumes equal to the cube of the scale factor and these relationships are shown below:

$$\lambda^2 = \frac{S_s}{S_m} \tag{2.23}$$

$$\lambda^3 = \frac{\nabla_s}{\nabla_m} \tag{2.24}$$

2.8.2 Kinematic Similarity

Kinematic similarity requires that all velocities in the flow, including components, to be scaled by the same scale factor (λ). This implies that the streamlines around the hull will be geometrically similar at model and full scale and therefore undergo similar motions.

Additionally, in order to maintain similarity, ratios between velocities in the model must he equal to the ratios between corresponding velocities at full scale at corresponding positions and is relevant to waterjet systems in particular.

2.8.3 Dynamic Similarity

Dynamic similarity requires that force-scale ratios should be equal in both full and model scale. This means that the direction of the forces and the ratio of the forces must be the same. The requirement is therefore to scale the model by the length Froude number (F_r), thus requiring the same ratio between gravity and inertia forces shown in Equation 2.25.

$$F_r = \frac{V_m}{\sqrt{g\ L_m}} = \frac{V_s}{\sqrt{g\ L_s}} \tag{2.25}$$

This similarity ensures that wave patterns for the same length Froude number will be the same in model and full scale so the wave making resistance follows the length Froude number. This is important since this is the basis for assuming that the residual resistance coefficient (C_R), which includes wave making resistance, will be equal in model and full scale. To obtain the correct ratio between inertia and viscous forces, dynamic similarity implies that model tests should be scaled by the Reynolds number (R_e):

$$R_e = \frac{V_m\ L_s}{\nu_m} = \frac{V_s\ L_s}{\nu_s} \tag{2.26}$$

Achieving complete dynamic similarity is not possible in every case, and the experimenter is charged with the responsibility to select the forces that dominate, and those that are relevant to both model and full scale.

The best basis for similarity theory is dimensional analysis which is essentially a means of utilising a partial knowledge of a problem when details are too obscure to allow an exact analysis. As dimensional analysis methods do not yield numerical answers they provide the form of the answer so that an experiment can be used to the fullest advantage in establishing a general empirical solution. This method rests on the basic principle that every equation which expresses a physical relationship must be dimensionally consistent. In mechanics there are three basic quantities which are mass (M), length (L), and time (T). Dimensions for all other quantities are made up using the three basic ones. Now consider the case of a ship moving with a constant velocity of V on the free surface. Geometrical similarity is assumed with the geometry of the vessels hull characterised by its length (L). Steady motion of the ship on the free surface a system of waves dependent on the gravitational acceleration (g) and this parameter must be included in the dimensional analysis along with the length (L), velocity (V), fluid density (ρ), and kinematic viscosity (ν) of the water. A detailed discussion about dimensional analysis in relation to dynamic similarity is given in Harvald (1991) and dimensional analysis reveals two important parameters in ship resistance which are as follows:

1. Reynolds number (R_e) which physically represents the ratio of inertial forces to viscous forces in the fluid.

2. Length Froude number (F_r) which is the ratio of inertia forces to gravity forces.

Therefore two geometrically similar hulls "geosims" with the same Reynolds number (R_e) and length Froude number (F_r) will have the same resistance coefficient (C_R) but to keep both variables the same at the same time is not really possible and so experimental scaling is usually done by using Froude scaling and Reynolds number is corrected for in the data analysis.

2.8.4 Froude Number

Froude number can calculated using different parameters and here only length Froude number (F_r) and depth Froude number (F_{rh}) will be discussed. Length Froude number can be thought of as being the ratio of inertial forces to gravitational forces in the system. Waterjet propulsion systems perform work on the water by lifting it through an elevation in order to expel it again above, or below, the water surface. Therefore, Froude number is significant and needs to be matched at model and full scale.

Dynamic similarity requirements applied on the ratio between inertia and gravity forces give the relation shown in Equation 2.27, where ρ is the fluid density, L is length waterline, g is the gravitational constant, V is the ship speed and the subscripts "i" and "g" (i.e. on the force variables) denote inertia and gravity forces. Equality in Froude number in model and full scale ensures that gravity forces are correctly scaled. As surface waves are also gravity driven, equality in Froude number will assure that wave resistance and other wave forces are correctly scaled as well.

$$\frac{Inertia\ force}{Gravity\ force} = \frac{F_i}{F_g} \propto \frac{\rho\, V^2\, L^2}{\rho\, g\, L^3} = \frac{V^2}{g\, L} \tag{2.27}$$

Applied on full scale and model scale this requirement gives Equation 2.28 where F_r is the length Froude number, and the subscripts "s" and "m" on the variables denote the model scale and full scale values.

$$F_r = \frac{V_m}{\sqrt{g\, L_m}} = \frac{V_s}{\sqrt{g\, L_s}} \tag{2.28}$$

Depth Froude number (F_{rh}) is defined as the ratio of the ship speed to the wave propagation speed in shallow water as shown in Equation 2.29, where h is water depth, V is ship speed, and g is gravitational constant.

$$F_{rh} = \frac{V}{\sqrt{g\, h}} \tag{2.29}$$

2.8.5 Reynolds Number

Equal ratio between inertia and viscous forces will give Equation 2.30, where R_e is the Reynolds number and kinematic viscosity (ν) is given by Equation 2.31, where μ is the viscosity, and ρ is the fluid density. Equality in Reynolds number between full and model scale will therefore ensure that the viscous forces are correctly scaled.

$$\frac{F_i}{F_v} \approx \frac{\rho\, V^2\, L^2}{\mu\, V\, L} = \frac{\rho\, V\, L}{\mu} = \frac{V\, L}{\nu} = R_e \tag{2.30}$$

$$\nu = \frac{\mu}{\rho} \tag{2.31}$$

2.9 Previous Research

In reviewing research dedicated to the inner workings and behaviour of waterjet propulsion systems, many interesting theses, papers, and reports were found and each of these sources reveal facts about waterjet propulsion systems, experimental testing, and extrapolation of results. In this section a thorough review of available, published literature is presented.

Waterjet self-propulsion testing has been an ongoing discussion for many years and significant progress has been made in the last decade, particularly by the International Towing Tank Conference (ITTC) Propulsion Committee, and all the researchers and institutions involved. There was a shift in the importance from a thrust deduction based analysis of waterjets to a momentum flux based analysis as outlined in Bose (2008). The momentum flux theory is now the preferred analysis method of ITTC, while other institutions such as Maritime Research Institute Netherlands (MARIN), use a combination of both methods to analyse model waterjet performance.

Literature contains several extrapolation procedures such as ITTC 1978 published in Lindgren et al. (1978) or publications by David Taylor Model Basin (DTMB) which rely on a complete set of data to allow for an accurate extrapolation to full-scale. For example, extrapolation based on ITTC 1978 requires three different tests for a complete dataset (bare-hull resistance test, self-propulsion test and waterjet system test). Several other institutions such as the Center for the Commercial Deployment of Transportation Technologies (CCDoTT) have created detailed reports regarding the planning of waterjet self-propulsion tests, data acquisition setup, the correlation to full-scale and the applied corrections. These reports can be used as basic guidelines for the planning of the self-propulsion tests and the final report of this project was published in Rispin (2007). The background of the project was the model self-propulsion testing (with a model to full scale ratio of 17.5) of a single catamaran demihull of 6.04 m in length featuring scaled waterjet inlets and the hull was based on a

representative 40 knot catamaran design where the main area of interest was inlet/hull interaction. Differences of boundary layer thicknesses were taken into account in the data scaling procedure. Thrust deduction was positive on the model scale, but taking this correction into account resulted in negative thrust deduction fraction and this conclusion raised the question whether the thrust deduction is dependent on scaling or not. Additional waterjet propulsion testing was carried out at the Naval Surface Warfare Center Carderock Division (NSWCCD) in 2001 using an advanced hull form with twin shaft underwater discharge waterjets from Rolls Royce and results were published in Chesnakas (2001) and Scherer et al. (2001).

Interaction of free surface, jet, hull flow, and hull were studied by Allison (1993) to investigate the moments and resulting forces through Computational Fluid Dynamic (CFD) calculations and model tests. An analytical method to defined inlet/hull flows for a large semi displacement monohull was presented based on reference frame moving with the hull and submerged nozzles.

A comprehensive study on waterjet/hull interaction investigating in particular the effect of different parameters on the interaction was carried out by van Terwisga (1996). The definitions proposed by van Terwisga (1996) were used by the ITTC Waterjet Specialist Committee and incorporated into The Specialist Committee on Validation of Waterjet Test Procedures in 2002. The adopted method was a control volume approach which balances momentum and energy through the waterjet system to arrive at system thrust, delivered power, and thrust deduction. A prediction for full scale delivered power can be made from assumptions made for the full scale pump efficiency, and inflow wake scaling. The ITTC committee identified the accurate measuring of the pump mass flow as the area of largest uncertainty and this is due to nonuniformity of the output nozzles, the measurement of hull resistance, and the determination of the proper towing force. Work presented in van Terwisga (1996) found that a difference between net thrust and gross thrust may occur notably around ship speeds where the transom is not fully cleared. This difference is very small for higher speeds and therefore the difference between bare-hull resistance and gross thrust is a good measure of the resistance increment of the hull due to flow induced by the waterjet. Through an uncertainty analysis it was shown that the errors in flow rate measurements in power estimation increases with decreasing Jet Velocity Ratio (JVR).

At about the same time as van Terwisga (1996), Coop (1995) investigated hull/waterjet interaction effects using a flush type intake planning hull of 7.4 m in length and the main purpose of the research was the validation of an analytical towing model against full scale and model scale and model scale test results. A Computational Fluid Dynamics (CFD) investigation of hull/waterjet flow interaction was carried out by Hughes et al. (1997) investigating the comparison of experimental data with CFD predictions for the flow through and over the upstream hull and inlet duct of a waterjet geometry.

Dynamic forces on a waterjet, without consideration of the interaction with the hull, was studied by Bulten (2006) and in contrast to van Terwisga (1996) concluded that the net thrust and gross thrust are significantly different and these conflicting conclusions potentially result in different thrust deduction values. Investigations carried out by Bulten (2006) included numerical and experimental analysis of a waterjet test setup where the waterjet inlet was tested in a cavitation tunnel and where the mass flow rate in the tunnel was adjusted to achieve the chosen inlet velocity ratio (IVR) values. The same setup, which also included waterjet stator and rotor geometry, was then modelled in Computational Fluid Dynamics (CFD) using a defined velocity profile at the inlet of the cavitation tunnel as well as a constant pressure boundary condition at the outlet plane.

A series of waterjet propulsion tests on a slender high-speed hull form model propelled by four side-by-side waterjet units was carried out by Wilson et al. (2005), where jet system thrust was calculated using momentum flux change through that waterjet control (Section 2.1) volume as introduced by 21st ITTC Waterjet Specialist Committee in 1996. As part of this research a detailed analysis of the balance of viscous forces and pressure on the ship was suggested in order to explain the mechanics of negative thrust deduction.

An integral force/moment model to simulate waterjet/hull interaction was introduced by Kandasamy et al. (2011). Using an Unsteady Reynolds-averaged NavierStokes (URANS) solver and a body force model to serve as waterjet pump, Takai et al. (2011) simulated a waterjet driven high-speed sealift hull to optimise that intake. Despite the measured thrust deduction being positive for the studied hull, a negative thrust deduction was computed for a wide speed range.

An extensive set of experiments applying Laser Doppler Velocimetry (LDV) and pitot-static tubes to investigate the static pressures and velocity field for three hull variants to study the effects of different propulsors was accomplished by Jessup et al. (2008). The first hull was equipped with four propellers with open shaft and strut appendages and the second and third hull were intended for axial and mixed flow waterjets. Despite the fact that the overall thrust of the axial flow waterjet was smaller than the thrust of the mixed flow waterjet, negative thrust deductions were reported for the hull with the mixed flow waterjet units.

More recent investigations of waterjet/hull interaction effects and thrust deduction are introduced in Eslamdoost (2012, 2014). The main area of interest of these investigations was the study of thrust and powering of waterjet propulsors. For a propeller, the net thrust can be obtained by measuring the force passed on through its shaft, but as there is not just a single point of contact between the waterjet unit and the hull, net thrust measurements cannot be easily accomplished. Instead of the net thrust, another thrust force that is simpler to measure is defined to express the magnitude of the waterjet thrust and this new thrust

definition is called gross thrust, which is obtained by the measurement of the momentum flux change through the control volume of the waterjet.

Due to contradictory conclusions found in literature it seems that the mechanism of the waterjet/hull interaction is currently not fully understood. As propeller driven hulls have a larger resistance than the corresponding towed hull resulting thrust deduction fractions are positive but waterjet driven hulls may well have negative thrust deductions as shown in van Terwisga (1996) and Eslamdoost (2014). Since the definition of thrust deduction is slightly different from that of conventional propeller hulls, this does not necessarily mean that the waterjet hull has a smaller resistance than the bare hull.

As a result of the investigation of previously published research a gap was identified in the literature regarding waterjet self-propulsion extrapolation procedures based only on waterjet self-propulsion tests and this research project will present an alternative approach based on thrust versus towing force comparisons using proven testing methods.

Chapter 3

Experimental Methodology

The main objective of the experimental waterjet propulsion testing was to quantify waterjet powering performance in uniform inflow and to obtain a better understanding of the physical problems of waterjet performance estimates. Powering performance was evaluated at non-cavitating conditions through measurements of flow rate, shaft speed, and shaft torque carrying out load varied self-propulsion testing of a single waterjet propelled catamaran demihull. Several additional measurements were carried out such as a turbulence stimulator investigation, trim tab investigation, and boundary layer measurements for momentum wake fraction determinations.

This chapter contains descriptions of the facilities used for experimental testing, descriptions of the tested waterjet, test conditions, data reduction methodology, and instrumentation systems which include flow rate measurements, pressure measurements, thrust, and velocity measurements.

3.1 Facilities

Bare-hull resistance, flow rate measurement, and waterjet propulsion testing was carried out using two different facilities at the Australian Maritime College (AMC): the towing tank (TT) and the model test basin (MTB). The towing tank was used for bare-hull resistance (see Section 4.4) and waterjet propulsion testing (see Section 4.6) and specifications of the AMC towing tank are given in Table 3.1.

Table 3.1: Specifications Of The AMC Towing Tank.

Parameter	**Dimension**
Length:	100 m
Width:	3.55 m
Water depth (standard):	1.5 m
Carriage speed range:	1.0 to 4.6 m/s

The second facility used for experimental testing was the AMC model test basin. The test carried out using this facility was the waterjet flow rate measurement testing (see Section 4.5). A change of facility was necessary due to scheduling constraints and as the flow rate measurements were carried out as a static test this facility was also better suited for the purpose and specifications of the AMC model test basin are given in Table 3.2.

Table 3.2: Specifications Of The AMC Model Test Basin.

Parameter	**Dimension**
Length:	35 m
Width:	12 m
Water depth (standard):	0.9 m

For the flow rate measurement testing, the main requirement was to have a body of water where the statically mounted waterjets pump water into a bucket and flow rate is measured as a change of expelled mass of water from the nozzle as a function of time.

3.2 Model Waterjet

A 6-bladed impeller and 7-bladed stator was designed for experimental testing based on the Lips Jet LJ120E waterjet unit, supplied the manufacturer Wärtsilä. The model waterjet is described in detail in Appendix B. The available power for the Incat 98 m wave-piercing catamaran (HSV-2) is described in the principal particulars of the vessel as 4 x 7,200 = 28,800 kW at 100% maximum continuous rating (MCR) for a top speed of 42 knots and 300 tonnes deadweight. To establish typical definitions of waterjet locations, the naming convention used by the 23rd ITTC Specialist Committee on Validation of Waterjet Test Procedures described in ITTC (2002) were adopted and the locations are described in Section 2.1.

3.3 Test Conditions

Three different types of tests were carried out: the first test was a bare-hull resistance test to establish resistance at hump speed, the second test was a static flow rate measurement test to determine flow rates to be used in reference with the waterjet self-propulsion tests, and the third test was a self-propulsion test. Bare-hull resistance testing (Section 4.4), with covered waterjet inlets and nozzles, was carried out at the AMC towing tank using two displacements (1,500 and 1,804 tonnes) with three static trim conditions each (0.5, 0, and -0.5 degrees) for a total of six conditions and a length Froude number range of 0.2 to 0.5 (full scale speed 12-28 knots). Static flow rate measurements (Section 4.5) were carried out at the AMC model test basin for a shaft speed range of 800 to 3,400 RPM and measuring of discharged water, by waterjet pump, as a function of time. Waterjet powering performance testing,

using a waterjet self-propulsion (Section 4.6) test, was carried out at the AMC towing tank using a single displacement (1,500 tonnes) and a single static trim (0 degrees) for a length Froude number range of 0.24 to 0.4 (full scale speed 14-24 knots) to capture performance parameters at the resistance hump speed (i.e. vessel speed at which maximum trim occurs.) as determined in the bare-hull resistance test.

3.4 Extrapolation

A detailed breakdown for experimental fluid dynamics is shown in Figure 3.1, where extrapolation is part of the data reduction equations in the data reduction section. Performance extrapolation of the waterjet self-propulsion testing was carried out using ITTC established extrapolation procedures as outlined in ITTC waterjet propulsive performance prediction guidelines 7.5-02-05-02, 7.5-02-05-03.1, and 7.5-02-05-03.2 which outline required quantities to be recorded for waterjet performance testing, recommends sensors and equipment, and describe recommended data reduction and extrapolation procedures. One other main source for extrapolation techniques used in this research project was publications related to waterjet propulsion testing and extrapolation of results by the Center for the Commercial Deployment of Transportation Technologies (CCDoTT) at California State University. The baseline hull for these tests was a representative 40 knot catamaran design, but only a single hull was tested as the main area of interest was inlet-hull interactions. Testing was carried out over the span of several years, resulted in a final report published in Rispin (2007). The published material included model building process, model waterjet, performance testing, data reduction, extrapolation as well as uncertainty analysis and acted as a very helpful case study for experimental testing of waterjet propelled models.

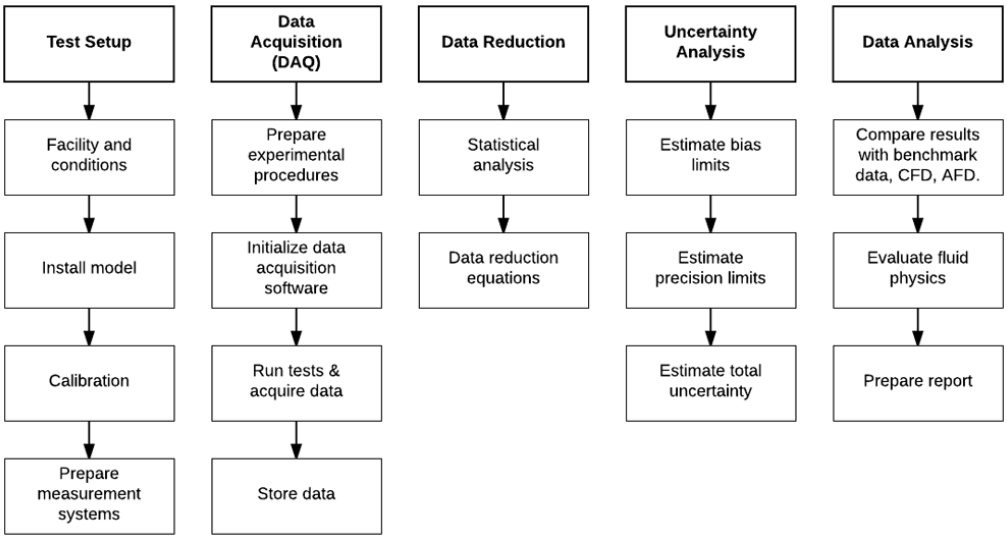

Figure 3.1: Schematic breakdown of experimental fluid dynamics where Computational Fluid Dynamics (CFD), Analytical Fluid Dynamics (AFD), and Data Acquisition System (DAQ).

3.5 Data Reduction Methodology

Data reduction was carried out on a thrust identity basis, where thrust, defined as gross thrust $T_G = Q_J(V_J - V_I)$ and discussed in Section 4.6.9, was established based on flow rate measurements, nozzle dimensions, and momentum wake fractions using boundary layer measurements. To validate thrust identity, model scale and full scale thrust coefficients (C_T) have to be the same so that $C_{Tm} = C_{Ts}$. Powering relations are discussed in Section 4.6.6 and the powering results used for this research are mainly based on effective power (P_E), delivered power (P_D), and effective pump power (P_{PE}). A detailed discussion of the thrust based extrapolation method, used for this research project, is discussed in Chapter 6.

3.6 Waterjet Performance Prediction

In 1996 the Waterjet Group of the 21st International Towing Tank Conference, as outlined in ITTC (1996), concluded that model self-propulsion tests were required to make reliable predictions of the performance of waterjet propelled crafts. However due to the uncertainty of the methodology and the complexity of the experimental procedures, many waterjet propelled ships are still being built without self-propulsion tests being conducted. Significant effort was made to improve this situation by Specialist Committees of the ITTC on Waterjet Test Procedures and ITTC Recommended Procedures and Guidelines were established and are being continuously improved as discussed in ITTC (2005a), ITTC (2005b), ITTC (2011c) and ITTC (2014). ITTC procedures and guidelines are kept as generic as possible and no detailed test procedures and extrapolation methods, such as the procedures for ships with marine propellers known as ITTC 1978, were specified. Implementation of the ITTC procedures is left up to the individual testing facilities. Other publications on waterjet performance testing techniques are given by Thornhill (1999), Rispin (2007), Jessup et al. (2008), and Eslamdoost (2014). Bulten (2006) describes an extensive experimental and numerical analysis of a waterjet propulsion system and Dang et al. (2013) outline the implementation of the ITTC recommended test procedures for waterjet systems.

3.7 Instrumentation Systems

In this section a short introduction is given in the type of instruments/sensors used to measure resistance, aft and forward sinkage, water temperature, flow rate basic static pressure measurements, impeller thrust, torque and shaft speeds, and velocity measurements for boundary layer measurements used to determine momentum wake fraction and waterjet inlet speed. All instruments used for experimental data acquisition were calibrated regularly, with the

linear variable differential transformers (LVDTs) and the resistance dynamometer (i.e. load cell) calibrated on a daily basis. The calibrations included all items of the measurement chain, including amplifier, signal conditioner, filter and analog to digital converter. For each device the range of calibration exceeded the range of values measured in the experiments. Linearity as well as repeatability of the calibration points was checked to ensure the least squares curve fit resulted in an accurate calibration factor.

3.7.1 Resistance

Resistance was measured using an Advanced Mechanical Technology (AMT) load cell (rated for a maximum force of 100 N) on the forward carriage post and was used for the resistance as well as the waterjet self-propulsion testing. The accuracy of the load cell was 0.2% as stated by the manufacturer and tolerances, as recommended by ITTC procedure 7.5-02-05-01, required that the resistance had to be measured to within 0.2% of maximum resistance or 0.05 N, whichever was the larger.

3.7.2 Aft and Forward Sinkage for Heave and Running Trim

Sinkage fore and aft was measured using two Schaevitz 5000 DC-EC linear variable differential transformers (LVDTs). The running trim and heave was then calculated from the measured running sinkage fore and aft as well as the distance between aft and the forward carriage post.

3.7.3 Speed

Speed of the AMC towing tank carriage was measured using a Red Lion Rotary Pulse Generator attached to a dedicated wheel. Measured speed was found to be within tolerances recommended by the ITTC procedure 7.5-02-02-01, where the speed of the model should be measured to within 0.1% of the maximum speed or to within 3 mm/s, whichever was the larger.

3.7.4 Water Temperature

Water temperature was required for the calculation of viscosity as well as water density and was measured at a depth near half of the model draught using a PT100 RTD temperature probe. It was assumed, that the water temperature was constant throughout the towing tank. Temperature measurements were recorded at least once per day, with daily variations being less than ± 0.2 degrees C.

3.7.5 Flow Rate

Waterjet flow rates were measured by carrying out a static flow rate measurement test measuring discharged mass of water as a function of time, as discussed in detail in Section 4.5. The flow rate measurements test consisted of a bucket where the discharged water was collected and a wave probe measured the change of mass of water in the bucket. Discharged mass of water over time resulted in the mass flow rate which in turn resulted in the gross thrust using wake fractions established in boundary layer measurements discussed in Section 4.6.3. The static flow rate measurement test was connected to the waterjet propulsion test by a reference measurement (see Section 3.7.9) at the nozzle outlet using Kiel probes and differential pressure transducers (DPTs) as outlined in Section 4.5.1. The main reason for carrying out the static flow rate measurement test was to establish a relationship of mass flow rate plotted against Kiel probe output, which was then used in the waterjet self-propulsion test to establish flow rates and gross thrust. The accuracy of the flow rate measurements is ±0.5% over the tested range.

3.7.6 Pressure Measurements

Important static pressure measurements are those at the inlet (momentum flux station 3) and at the nozzle outlet (momentum flux station 6). A single wall tap was used in this study for all stations and each wall tap was connected to an individual differential pressure transducer (DPT) with reference to the test section static pressure. Head rise was determined from the difference between the mean pressures at momentum flux station 3 and 5 and the accuracy of the head rise measurements is ±1.0%. Type PX142 (Omega Engineering Inc.) differential pressure transducers (DPTs) were used to measure static pressures using wall taps, reference measurement at waterjet nozzle for flow rate investigation, and boundary layer velocities at incremental vertical distances from the hull for determination of momentum wake fractions. Three different models of Omega Engineering Inc. DPTs used for this study. Accuracy of DPTs was determined in pressure calibration tests (testing several DPTs of the same model in controlled conditions) and a comparison of the measured and documented accuracies (from Omega Engineering Inc. type PX142 datasheets) is shown in Table 3.3.

Table 3.3: Comparison Of Measured And Documented Accuracies For Omega Engineering Inc. Type PX142 Differential Pressure Transducers Used For Measurements In Experimental Testing.

DPT model	**Measured accuracy**	**Documented accuracy** Min/Max
PX142-002D5V (2 PSI)	±0.3%	±0.4% / ±0.75%
PX142-005D5V (5 PSI)	±0.76%	±0.75% / ±1.5%
PX142-015D5V (15 PSI)	±0.47%	±0.4% / ±0.75%

3.7.7 Impeller Thrust, Torque and Shaft Speed

Impeller thrust and torque were measured using a Cussons self-propulsion propeller dynamometer type R31 (maximum rating: 4 Nm for torque and 100 N for thrust) located between the Dunkermotoren BG-75 CI electric motor and the waterjet pump for port and starboard waterjet propulsion systems as shown in Section 4.5.1. Documented accuracy of the self-propulsion propeller dynamometer in manufacturer datasheet was ±0.2% for torque and ±0.2% for thrust. Measurements for shaft speed were recorded using an AM9-10 analog induction proximity sensor by Automation Direct Pty Ltd mounted above each shaft connector connecting the electric motor and the self-propulsion propeller dynamometer. The induction proximity sensor reacts to a piece of steel (i.e. screw head) on the brass shaft connector as shown in Section 4.5.1. Measured shaft speeds were established in post processing the recorded shaft speed data after the tests were completed. During testing, direct measurement of the motor speed was given by the motor control software. Results based on induction proximity sensors was then used for analysis and documentation purposes as the motor control software was not capable to exchange data directly with the data acquisition system of the towing tank.

3.7.8 Velocity Measurements

Two different types of velocity measurements were part of the research, where the first type of velocity measurement was carried out to measure ship speed (i.e. towing tank carriage speed) which was measured using a rotary pulse generator attached to a dedicated wheel as described in Section 4.3. The second type of velocity measurement was related to the boundary layer measurements used to determine momentum wake fraction and inlet speed discussed in detail in Section 4.6.3. Velocity measurements for boundary layer profiles were carried out using model PCA-8-KL pitot-static tubes by United Sensors Corp together with model PX142-005D5V differential pressure transducers by Omega Engineering Inc to measure velocities at different vertical distances from the hull. Accuracy of the differential pressure transducers are discussed in Section 3.7.6 and were within 1% of manufacturer defined specifications. Accuracy of pitot-static tubes depend on errors due to turbulence, yaw and pitch angle (Figure 3.2) and increases rapidly for angles of attack larger than 5 degrees.

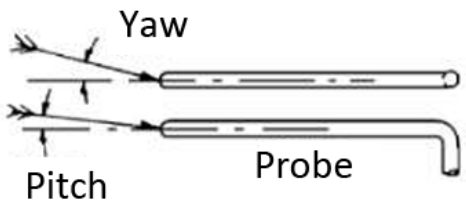

Figure 3.2: Description of yaw and pitch angles for pitot-static tubes.

3.7.9 Nozzle Reference Measurements for Flow Rate Determination

For reference measurements, connecting the flow rate measurement test (Section 4.5) and waterjet self-propulsion test (Section 4.6), a single United Sensor Corp. Kiel probe (model KAA-6) was used at each nozzle exit. Kiel probes were mounted just aft of the waterjet nozzle exit in line with the pump axis at the 70% nozzle exit radius of the port and starboard waterjet propulsion, where the velocity is expected to be close to the average nozzle velocity due to nozzle pressure distribution as described in Section 4.5.1. The advantage of Kiel probes, compared with other total pressure probes, is low sensitivity to direction of flow. Each Kiel probe was connected to a model PX142-005D5V differential pressure transducer Omega Engineering Inc. Accuracy of the differential pressure transducers are shown in Section 3.7.6 and were within 1% of manufacturer defined specifications. Turbulence errors are negligible, especially since Kiel probes are yaw insensitive and a definition of yaw and pitch is given in Figure 3.3.

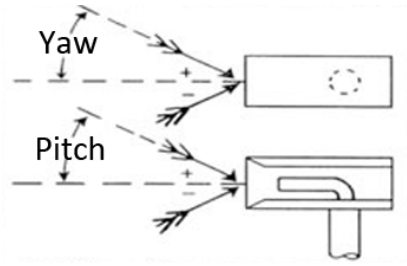

Figure 3.3: Description of yaw and pitch angles for Kiel probes.

Chapter 4

Experiments

This chapter describes the bare-hull resistance, flow rate measurement, and waterjet self-propulsion experiments, including the data analysis techniques and presents the test results. Due to the availability of testing facilities at the Australian Maritime College (AMC) the experimental testing was carried out in the following order: static flow rate measurement test, bare-hull resistance test, waterjet self-propulsion test, and repeat/validation of flow rate measurement test. Bare-hull resistance and waterjet self-propulsion tests were carried out using the AMC towing tank, whilst the flow rate measurement tests were conducted in the AMC model test basin. The repeated flow rate measurement test was carried out to validate the original flow rates, as established in the first test, as well as to refine uncertainty analysis results. A functional overview of the experimental test methodology is presented in Figure 4.1, which outlines model assembly, sensor calibration, bare-hull resistance test, flow rate measurement test, self-propulsion test, data reduction, analysis, extrapolation, and final results.

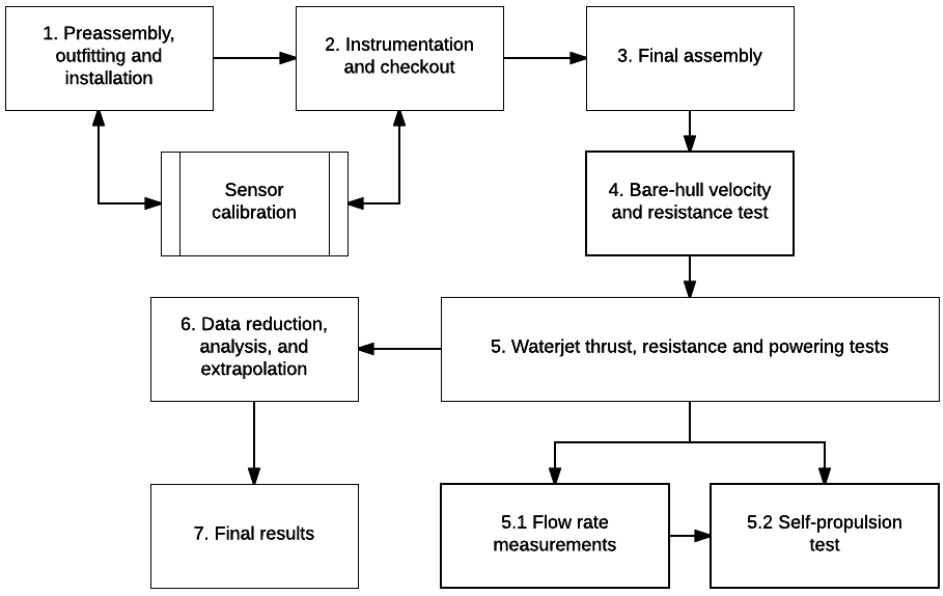

Figure 4.1: Functional overview of experimental test program.

If not stated otherwise the length Froude number, as shown in Equation 4.1, is used whenever Froude number is mentioned in the following sections and chapters. For a detailed description of scaling laws see Section 2.5.

$$F_r = \frac{V}{\sqrt{gL_{WL}}} \tag{4.1}$$

Schematic representations of the static flow rate and waterjet self-propulsion tests, including data acquisition system, required sensors and other test equipment are given in Appendix C.

4.1 Model Requirements

The vessel selected for experimental testing was a 98 m wave-piercing catamaran (Figure 4.2) designed by Revolution Design Pty Ltd and built by Incat Tasmania in 2003 with hull number 61. The vessel was selected due to the availability of sea trials data carried out in 2004 by the Naval Surface Warfare Center Carderock Division (NSWCCD) for the US Navy. The data measurements were carried out for 3 displacements (shallow water and deep water) and a speed range of up to 40 knots.

The general arrangement plan of a single demihull of the vessel is shown in Figure 4.3 and the waterjet propulsion consists of two Wärtsilä LJ120E waterjet units in each hull. Principal particulars of the 98 m Incat wave-piercing catamaran HSV-2 *Swift* are shown in Table 4.1.

Figure 4.2: Incat 98 m wave-piercing catamaran (hull 61) HSV-2 *Swift* underway.

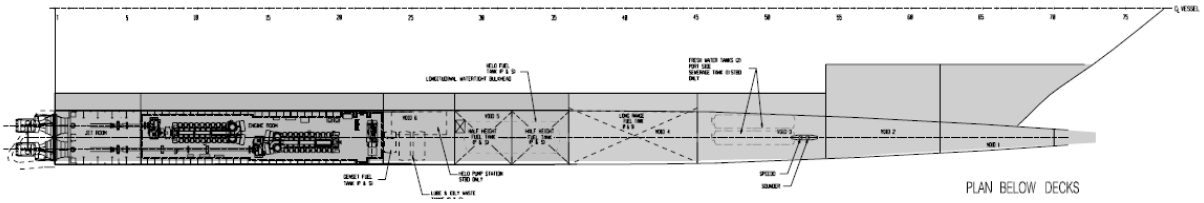

Figure 4.3: Waterjet propulsion arrangement of a single demihull of 98 m Incat wave-piercing catamaran (hull 61) HSV-2 *Swift* as shown on general arrangement plan provided by Incat Tasmania. Two Wärtsilä LJ120E waterjet units are installed in each demihull.

Table 4.1: Principal Particulars Of 98 m Incat Wave-Piercing Catamaran HSV-2 *Swift*.

General particulars			
Parameter	**Acronym**	**Unit**	**Value**
Length overall	L_{OA}	m	97.2
Length waterline	L_{WL}	m	92.0
Beam overall	B_{OA}	m	26.6
Beam of demihull	$B_{OA,\ demihull}$	m	4.5
Demihull distance	$C_{L,\ demihull}$	m	22.1
Loaded draft	T_{Loaded}	m	3.43
Speed			
Parameter	**Acronym**	**Unit**	**Value**
Speed at 627 tonnes deadweight	V_{627t}	knots	38
Speed at 300 tonnes deadweight	V_{300t}	knots	42
Machinery installations			
Engines	4x Caterpillar 3616 (each rated at 7,200 kW)		
Waterjet	4x Wärtsilä LJ120E		

Tests were performed using Froude similarity where the model scale Froude number and full scale Froude number are the same. Scale effects (i.e. errors of not keeping the Reynolds similarity) were then compensated for by numerical corrections. In order to minimise scale effects, the model should be as large as possible to avoid interference (i.e. blockage) effects from the towing tank walls and towing tank floor. Therefore, to maximise the available space required for the two model waterjet propulsion systems, just a single demihull was tested (see Section 4.2) and the increased space also allowed easier access to the propulsion system, sensor equipment, and carriage post attachments installed in the hull. Another requirement was to have easy access to the model in the towing tank, and as the model was installed close to the right towing tank wall (see Figure 4.4 in Section 4.2), the port demihull was selected for model construction.

The model size was established based on four main restrictions and four sub restrictions which are part of the restricted water effects:

- **Speed:** The model should be small enough such that the corresponding speed can be achieved by the towing tank carriage.
- **Size:** The model should be as large as possible to minimize viscosity scale effects (especially concerning laminar/turbulent flow and flow separation). The model should also be large enough to accommodate two model waterjet propulsion systems, especially the self-propulsion dynamometers (see Section 4.5.1) which would require a demihull beam of at least 200 mm.
- **Strength:** The model should be small enough to avoid strength problems (i.e. internal strength of the model and loads on the towing tank carriage).
- **Restricted water:** The model should be small enough to avoid noticeable effects of restricted water in the towing tank.
  - Based on Robbins et al. (2009) an influence exists on the wave resistance at depth Froude numbers larger than 0.8 where depth Froude number is calculated using $F_r = \frac{V}{\sqrt{gH}}$, where H is the water depth of the towing tank.
  - Blockage ratio ($\frac{A_C}{A_M}$), where A_C is the towing tank cross-sectional area, and A_M is the submerged cross-sectional area of the model should be less than 15 before a general restriction of the waterway will start to occur as discussed in ITTC (1987).
  - Flow around the hull is influenced by the towing tank boundaries if the water depth to draft ratio ($\frac{h}{T}$) is less than 4, as discussed in ITTC (1987). This effect is considered independent of the depth Froude number effect.
  - There is an influence from the lateral boundary on the stern flow if either the water width to length ratio ($\frac{W}{L}$) is less than 1 or the water width to beam ratio ($\frac{W}{B}$) is less than 4, as discussed in ITTC (1987).

For the model sizing, a maximum testing speed was set of 28 knots, and the model was designed so that the depth Froude number would be 0.8 at this speed. Based on the discussed restrictions, a decision matrix was established to find the best possible model size for experimental testing and the results are shown in Table 4.2, where L_{OA} is length overall, L_{WL} is length waterline, B_{OA} is beam overall, B_{DH} is beam of a single demihull, T is draft, λ is full scale to model scale ratio, $\frac{A_C}{A_M}$ is the blockage ratio, $\frac{h}{T}$ is the water depth to draft ratio, and $\frac{W}{B}$ is the water width to beam ratio.

Table 4.2: Decision Matrix For Model Length Range Of 3 To 6m Used For Model Size Selection.

L_{OA}	L_{WL}	B_{OA}	B_{DH}	T	λ	$B_{DH>200\,mm}$	$F_{r@28\,knots}$	$\frac{A_C}{A_M}$	$\frac{h}{T}$	$\frac{W}{B}$
m	m	m	m	m	-	-	-	-	-	-
3.0	2.84	0.82	0.14	0.11	32.4	No	< 0.8	362	14	26
3.3	3.12	0.90	0.15	0.12	29.5	No	< 0.8	299	13	23
3.6	3.41	0.98	0.17	0.13	27.0	No	< 0.8	252	12	21
3.9	3.69	1.07	0.18	0.14	24.9	No	< 0.8	214	11	20
4.2	3.97	1.15	0.19	0.15	23.1	No	< 0.8	185	10	18
4.5	4.26	1.23	0.21	0.16	21.6	Yes	$= 0.8$	161	9	17
4.8	4.54	1.31	0.22	0.17	20.3	Yes	> 0.8	142	9	16
5.1	4.83	1.40	0.24	0.18	19.1	Yes	> 0.8	125	8	15
5.4	5.11	1.48	0.25	0.19	18.0	Yes	> 0.8	112	8	14
5.7	5.39	1.56	0.26	0.20	17.1	Yes	> 0.8	100	7	13
6.0	5.68	1.64	0.28	0.21	16.2	Yes	> 0.8	91	7	13

Evaluating all restrictions resulted in an acceptable overall model length of 4.5 m, length waterline of 4.26 m, demihull beam of 0.21 m, and a full scale to model scale ratio of 21.6 shown in Table 4.3 together with respective full scale particulars. The maximum tested model speed, at the selected scale, and a full scale speed of 28 knots was 3.1 m/s, which allowed for a data recording time in the towing tank of about 15 seconds which was considered sufficient. Models typically tested at AMC have a length of 2 to 2.5 m, but using a length like this was not possible as scaling the catamaran demihull to this length resulted in demihull beams of 0.09 to 0.12 m that were too narrow to fit the two model waterjet propulsion systems.

Table 4.3: Full And Model Scale Ship Particulars Scaled Using A Scale Ratio Of 21.6.

Parameter	**Acronym**	**Unit**	**Full scale**	**Model scale**
Length overall	L_{OA}	m	97.2	4.5
Length waterline	L_{WL}	m	92.0	4.26
Beam overall	B_{OA}	m	26.6	1.23
Beam overall of demihull	$B_{OA,\ demihull}$	m	4.5	0.21
Demihulls centreline distance	$C_{L,\ demihull}$	m	22.1	1.02

Based on the established model dimensions, the structural design process and material selection was then started and the detailed model construction process is described in Appendix A. A description of the design and construction of the 3D printed model waterjet propulsion system used for the experimental testing is given in Appendix B.

4.2 Single Demihull Testing

Based on the space requirements of two waterjet units in each hull and the desire to increase total forces and decrease scaling effects, it was desirable for the testing model to be as large as possible within the confines of the Australian Maritime College (AMC) towing tank. Taking into account the dimensions of the AMC towing tank with length 100 m, width 3.55 m and depth 1.5 m as well as shallow water and blockage considerations, it was decided that the testing of a single demihull would be the preferred method of testing.

A novel technique to predict the effects of catamaran demihull spacing was presented by Rovere (1997) and is based on testing of a single catamaran demihull in close proximity to the towing tank wall. The towing tank wall acts as the plane of symmetry, reflecting the waves and thereby providing the correct wave interference and blockage effects from the second, non-existing, hull. The investigation carried out by Rovere (1997) included a large number of experimental results as well as theoretical computations to examine the hypothesis that the single demihull testing method is a viable option to accurately predict the influence of the catamaran demihull spacing. A schematic representation of the single demihull testing method is shown in Figure 4.4, where the symmetry plane of the catamaran is shifted to the towing tank wall.

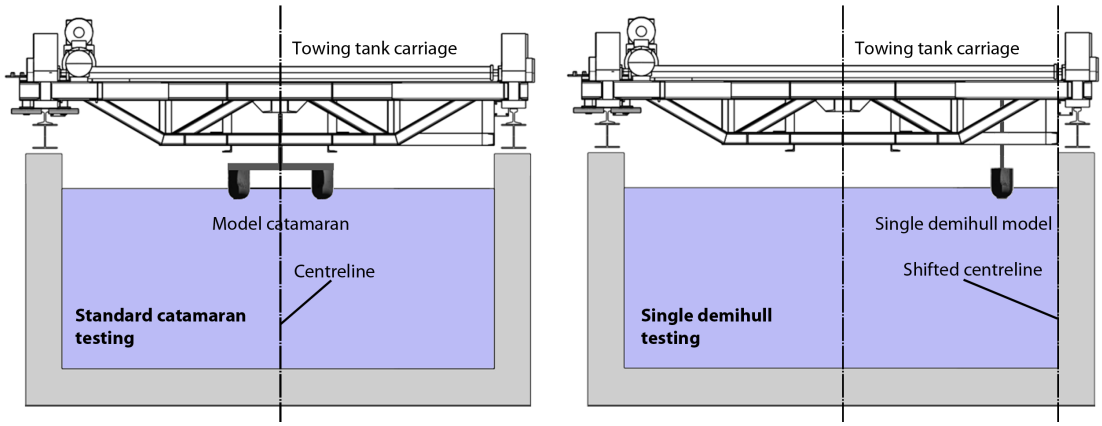

Figure 4.4: Single demihull testing shown as schematic representation of the standard catamaran testing method (left), where the model catamaran is located at the centre of the towing tank and the single demihull testing method (right), where a single demihull is located half a demihull centreline distance off the towing tank wall.

An investigation, using Computational Fluid Dynamics (CFD), was presented by Haase et al. (2014) where the model setup using a single demihull with the towing tank wall as a symmetry plane was replicated. The study also included a series of changing demihull separations to investigate the resistance change in correlation with the change in demihull separation. Results from this research confirmed the results presented by Rovere (1997) and also showed that the influence of hull separation on the resistance for $\frac{S}{L} < 0.2$ is about 3%.

4.3 General Instrumentation

Several of the measuring instruments listed below were used for multiple sets of tests, such as the resistance, flow rate measurement, and waterjet self-propulsion tests. All the other test-specific sensors and instruments are described in the instrumentation sections of the respective test outlines and are discussed for bare-hull resistance test in Section 4.4.1, for static flow rate measurement test in Section 4.5.1, and for waterjet self-propulsion test in Section 4.6.1.

- **Model speed:** Rotary pulse generator attached to a dedicated wheel of the towing tank carriage.
- **Model resistance:** Single Advanced Mechanical Technology (AMT) load cell located on the forward carriage post. Maximum rating: 100 N.
- **Model sinkage:** Two Schaevitz 5000 DC-EC Linear Variable Differential Transformers (LVDTs). One LVDT is located at the forward and the other at the aft carriage post. The running trim was calculated from the measured running sinkage fore and aft.
- **Impeller thrust:** Cussons Ship Model Self-Propulsion Dynamometer (Type R31). Maximum rating: 100 N.
- **Shaft torque:** Cussons Ship Model Self-Propulsion Dynamometer (Type R31). Maximum rating: 4 Nm.
- **Reference measurement (for flow rate):** Two model KAA-6 Kiel probes by United Sensors Corp. and two PX142-005D5V Differential Pressure Transducers (DPT) by Omega Engineering Inc. Maximum rating: 5 PSI.

4.4 Bare Hull Resistance Test

The standard bare-hull resistance test was carried out following the International Towing Tank Committee 1978 guidelines as described by ITTC (2011a). The main objective of the resistance tests was to obtain a full dataset for the model demihull as this hull form was not previously model tested, and to determine the full scale resistance (R_{TS}), form factor (k), and the wave making coefficient (C_R).

4.4.1 Setup and Instrumentation

Table 4.4 shows the quantities and units measured for the bare-hull resistance test which are just model speed, sinkage, and resistance (drag).

Table 4.4: Quantities And Units Measured For Bare-Hull Resistance Test.

Measurement	**Unit**
Model speed (V_m)	m/s
Total resistance (R_{Tm})	N
Sinkage fore and aft (z_{SF}, z_{SA})	mm
Running trim and running sinkage (t_V, z_V)	mm & deg.
Water temperature (t_w)	°C

As described in Section 4.3, the four sensors used for the bare-hull resistance tests consisted of a rotary pulse generator attached to a dedicated wheel of the towing tank carriage to measure model speed, two Schaevitz 5000 DC-EC Linear Variable Differential Transducers (LVDTs) to measure sinkage (running trim was calculated from the measured running sinkage fore and aft), and an Advanced Mechanical Technology (AMT) load cell located on the forward carriage post to measure resistance (i.e. drag). A representative picture of the two towing tank carriage posts is shown in Figure 4.5.

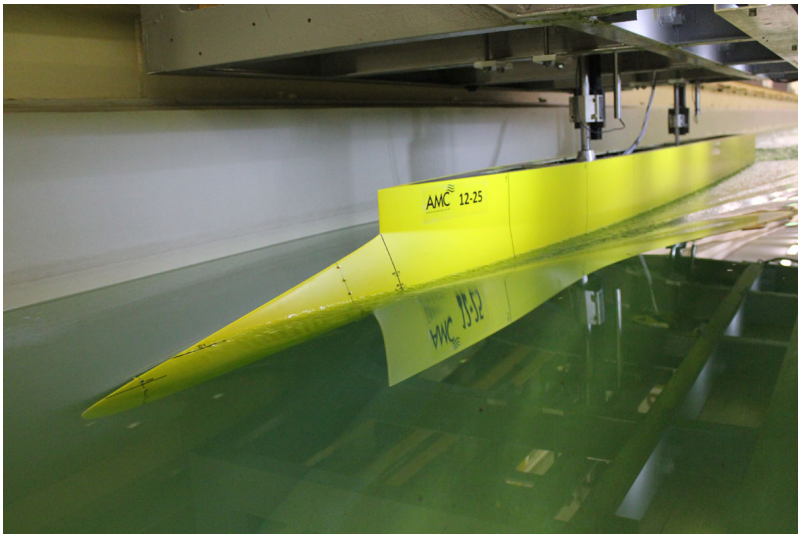

Figure 4.5: Resistance test showing run 96: Displacement 1,500 tonnes, $F_r = 0.35$ and static level trim. The two carriage posts are visible as are the LVDTs (located in the tube beside each carriage post).

All instruments used for the data acquisition system (DAQ) were calibrated were at least calibrated at the start and the end of testing, with the LVDTs and the resistance force transducer (i.e. load cell) calibrated on a daily basis. The calibrations included all items of the measurement chain, including amplifier, signal conditioner, filter and analog to digital converter. The range of calibration exceeded the range of values measured in the experiments and linearity and repeatability of the calibration points were checked to ensure a good least squares (R^2) curve fit. Ballasting and trimming of the model was carried as per ITTC Recommended Procedure 7.5-01-01-01 and the model was loaded based on the two displacements

(1,500 and 1,804 tonnes) and was within 0.2% of the Froude scaled displacement. Initial readings of all instruments were taken before to each run and were also checked between runs to ensure no notable drift had occurred. Acquisition of data commenced after a constant speed was achieved and the model was in a steady-state situation. The sampling rate was set at 200 Hz and generally about 20 seconds of steady-state condition data was recorded for each run, although this number had to be slightly reduced to enable higher speeds to be investigated. Mean values for each test run were derived from the time series data, selecting a time window where the measurement values had stabilised. This process was repeated for all speeds tested. Sufficient time was allowed between consecutive runs to allow the water surface to settle and achieve similar conditions for each of the runs.

4.4.2 Test Program

Bare-hull resistance test conditions included two displacements (1,500 and 1,804 tonnes), length Froude number range of 0.2 to 0.5 and static trims of -0.5, 0 (level) and 0.5 degrees. The waterjet inlets were covered up using a plug and sealed with plasticine as shown in Figure 4.6 and the weight of included water in the waterjet tunnel was compensated by using ballast located on top of the waterjet tunnel to preserve the trim and displacement.

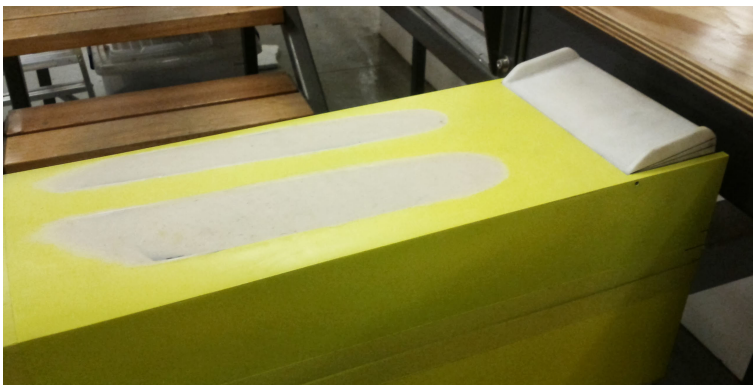

Figure 4.6: Covered waterjet inlet for bare-hull resistance test.

The bare-hull resistance test program was divided into four separate tests: turbulence stimulator investigation, trim tab optimisation, bare-hull resistance test, and Prohaska runs for form factor estimation. The bare-hull resistance test series spanned full scale velocities from approximately 12 to 28 knots (model speeds from 1.3 to 3.1 m/s) and a summary of the test conditions for all four test types showing static trim conditions, trim tab settings, tested displacements and test speed range, in length Froude number, is given in Table 4.5.

Table 4.5: Summary Of Static Trim Conditions, Trim Tab Settings, Displacements And Speed Ranges For Four Different Resistance Tests.

Test	**Static trim**	**Trim tab**	**Displacement**	**F_r**
	degrees	degrees	tonnes	-
Turbulence stimulators	0	5	1,500	0.23, 0.44
Trim tab optimisation	0	0, 5, 10	1,500	0.43, 0.45, 0.47
Bare-hull resistance	-0.5, 0, 0.5	5	1,500 & 1,804	0.2 to 0.47
Prohaska runs for (1+k)	Deep transom	5	1,500	0.1 to 0.2

To determine the accuracy and repeatability of results, measurements for every speed in the bare-hull resistance test were repeated three times. All resistance related tests were carried out with closed waterjet inlets, closed waterjet nozzles and corrected weight of entrained water. To support bare-hull resistance test documentation still pictures were taken for each testing condition as well as video showing the port side view of the bow and the stern of the model.

4.4.3 Friction Line

The purpose of the calculation of the frictional coefficient (C_F) is to determine a consistent form factor across the required speed range and wave making coefficient or coefficient of friction (C_R), as described by Grigson (1993). The two friction lines considered were the ITTC 1957 (Equation 4.2) model ship correlation line shown in Manen et al. (1988), which is recommended for use with the ITTC 1978 method and the Grigson friction line.

$$C_F = \frac{0.075}{(log_{10}R_n - 2)^2} \tag{4.2}$$

Grigson (1989, 1993, 1995, 2000) describe an alternative formulation for the turbulent flat-plat friction line and its utilisation for ship powering extrapolation for experimental model testing. In two of these papers, Grigson (1993, 2000) presented two different forms of an approximation to this line. The first approximation is in the form of a curve fitted to the differences between the new line and the standard ITTC 1957 model-ship correlation line. The second, more accurate approximation is given in terms of factors G_1 and G_2 as described by Bose (2008). These factors can be multiplied to give the Grigson friction coefficient values where factor G is either G_1 or G_2, dependent on the Reynolds number:

$$C_{F\,Grigson} = C_{F\,ITTC1957} \times G \tag{4.3}$$

Reynolds number range for G_1 from 1.5x10^6 to 20x10^6 (Equation 4.4) where x=log R_e-6.3.

$$G_1 = 0.9335 + 0.147x^2 - 0.071x^3 \tag{4.4}$$

Reynolds number range for G_2 from 20x10^6 to 6x10^9 (Equation 4.5) where x=log R_e-7.3.

$$G_2 = 1.0096 + 0.0456x - 0.013944x^2 + 0.0019444x^3 \tag{4.5}$$

The improvement of Grigsons formulation is based on the theoretical development of the friction line and the improved consistency of form factors in geosim research as published in Grigson (1995, 2000). For the purpose of this project and all the results shown in this thesis, the friction line used is based on Grigson (1993) as form factors are expected to be more consistent. In addition, the propulsion committee of the 23rd International Towing Tank Conference recommended the use of Grigsons line as being a physically more accurate approximation of turbulent flat plate friction compared to the ITTC 1957 friction line.

4.4.4 Form Factor

The form factor (k) was determined according to Prohaska's method using results from low speed resistance test discussed in Lindgren et al. (1978) and ITTC (2011b). The speed range used for the Prohaska testing ranged from Froude length number 0.1 to 0.2. Test conditions for Prohaska testing were set as using light displacement, 1,500 tonnes, and transom out of the water which resulted in a static trim of approximately 3 degrees by bow and a representative picture of the slow-speed resistance testing for form factor estimation is shown in Figure 4.7.

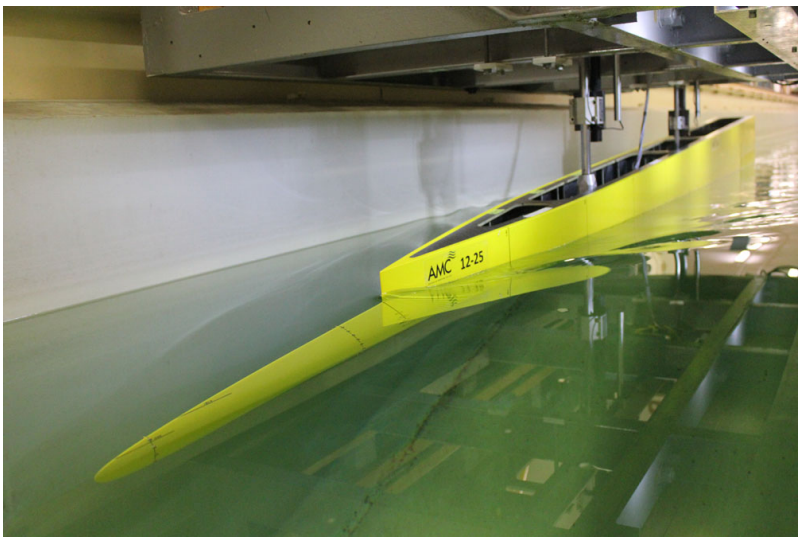

Figure 4.7: Slow-speed resistance test for form factor determination showing run 235: Displacement 1,500 tonnes, F_r = 0.12 and transom out of the water with a static trim of approximately 3 degrees by bow.

Prohaska test runs were carried out for a length Froude number range of 0.1 to 0.2 (equivalent full scale speed 5.9 to 10.6 knots) and measurements for each tested speed were repeated three times to provide information on repeatability. The Grigson friction line as well as the ITTC

1957 friction line were used to establish the frictional resistance (C_F). The total model resistance coefficient (C_T) was calculated using Equation 4.6.

$$C_{Tm} = \frac{R_{Tm}}{\frac{1}{2}\,\rho_m\,S_m\,V_m^2} \tag{4.6}$$

When the wave-resistance component in a low speed region (i.e. $0.1 < \mathrm{F_r} < 0.2$) is assumed to be a function of F_r^4, the straight line plot of $\frac{C_{Tm}}{C_{Fm}}$ versus $\frac{F_r^4}{C_{Fm}}$ will intersect the ordinate ($\mathrm{F_r}$=0) at (1+k) and therefore enables the form factor to be determined. The experimentally determined form factors, using this method, are shown in Figure 4.8 where (1+k) established using Grigson friction line is 1.14 and (1+k) using ITTC 1957 friction line is 1.08. Results below 0.1 of $\frac{F_r^4}{C_{Fm}}$ were omitted from analysis due to very high scatter, which decreased the least squares (R^2) of the linear fit to approximately 0.1. A form factor of 1.14 was used for the performance analysis described in all successive chapters of this thesis.

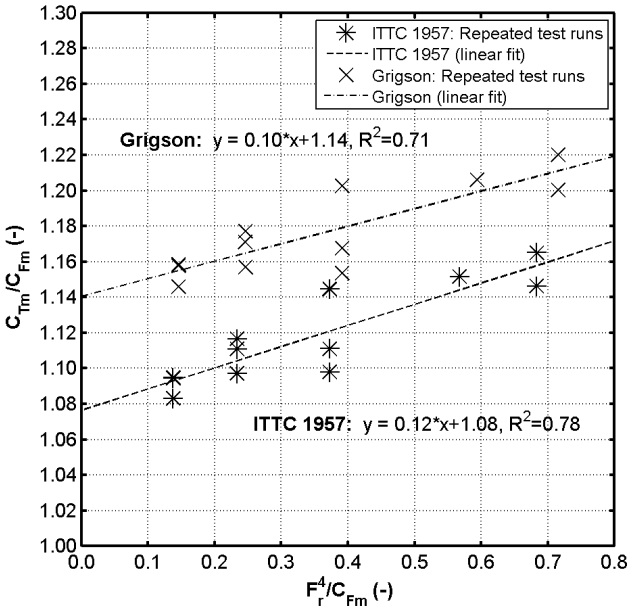

Figure 4.8: Form factors by using Prohaska method, length Froude number range of 0.1 to 0.2, displacement 1,500 tonnes and transom out of the water which resulted in a static trim of approximately 3 degrees by bow.

Uncertainty on total resistance coefficient (C_T) varies from to 17 to 5% in the length Froude number range of 0.1 to 0.2, decreasing with higher length Froude numbers as shown in resistance uncertainty analysis results in Section 4.4.10. Using either Grigson friction line or ITTC 1957 friction line shows a remaining problem in determining an accurate form factor using Prohaska's method, which is the scatter in resistance at low speeds.

4.4.5 Turbulence Stimulator Investigation

The flow regime is an important aspect of model testing and the model should be fitted with a recognised turbulence stimulator. Suitable turbulence stimulators include sand grain strips, wires and studs as outlined in ITTC (2011d). Figure 4.9 from Hughes et al. (1951) and National Physical Laboratory (1960) gives guidelines for the location and the dimension of studs as turbulence stimulators on a raked stem of conventional type.

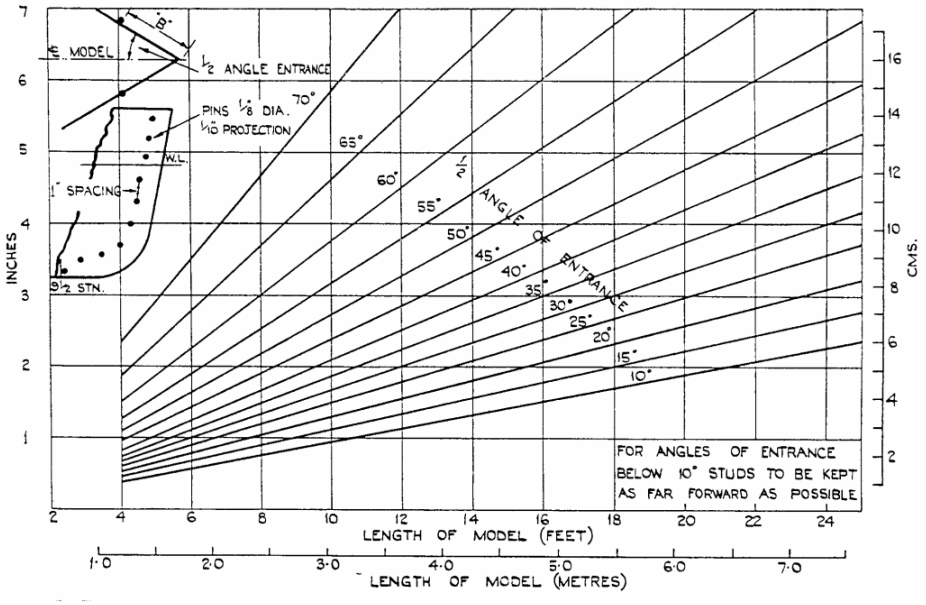

Figure 4.9: Location of turbulence stimulators as given in ITTC guideline 7.5-01-01-01.

Previously, when model testing wave-piercing catamarans at the AMC the location of the turbulence stimulators was slightly forward of the stem, compared to the location of 5% LPP aft of the forward particular as recommended by ITTC (2011d). A different approach was proposed for the current testing series with a small turbulence stimulation investigation being carried out, based on a non- ITTC approach to establish the most appropriate location of the turbulence stimulation on wave-piercing catamaran hulls.

The new approach for the locations of the turbulence stimulators is based on momentum thickness as described by Preston (1958) and McCarthy et al. (1976) where the minimum value for fully developed turbulent boundary layer is set as $R_\theta < 320$. Schlichting et al. (2000) give Equation 4.7 to determine momentum thickness.

$$\theta = 0.664\sqrt{\frac{\nu\, x}{U_\infty}} \tag{4.7}$$

For Reynolds number based on momentum thickness:

$$R_{e\theta} = \frac{U_\infty\, \theta}{\nu} \tag{4.8}$$

Combining Equation 4.7 and Equation 4.8 and solving for x gives:

$$x = \left(\frac{R_{e\theta}\ \nu}{U_\infty\ 0.664} \right)^2 \frac{U_\infty}{\nu} \tag{4.9}$$

Using Reynolds number based on momentum thickness theory as $R_{e\theta}$=320 and the minimum and maximum expected model testing speeds, two distances (x) from the leading edge (forward perpendicular of model) were calculated to locate rows of turbulence stimulators (72 mm and 434 mm). The turbulence stimulator types selected were studs and the stud diameter (3 mm), height (3 mm) and spacing (20 mm) were determined using the standard ITTC procedure presented in ITTC (2011d). The final arrangement of the turbulence stimulators on the wave piercing model hull is shown in Figure 4.10.

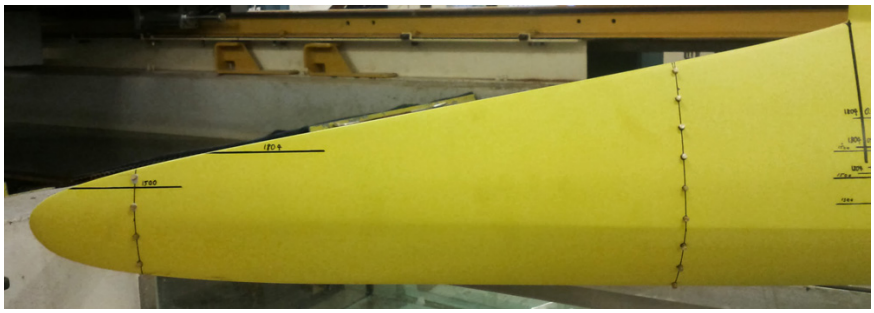

Figure 4.10: Final arrangements of two rows of turbulence stimulators, using studs, on wave-piercing model hull as determined using momentum thickness theory.

The turbulence investigation carried out to check the effectiveness of the turbulence stimulators consisted of three types of resistance tests:

1. Bare-hull resistance test without any turbulence stimulators
2. Bare-hull resistance test using a single row of turbulence stimulators
3. Bare-hull resistance test using both rows of turbulence stimulators

All resistance tests related to turbulence stimulation were carried out using a displacement of 1,500 tonnes, level static trim, trim tab at 5 degrees, and two different speeds which are F_r = 0.23 (low speed) and F_r = 0.44 (high speed) for each condition. The results of the resistance tests using different arrangements of rows of turbulence stimulators are shown in Figure 4.11 as a comparison of total resistance coefficient (C_{Tm}) compared to length Froude number.

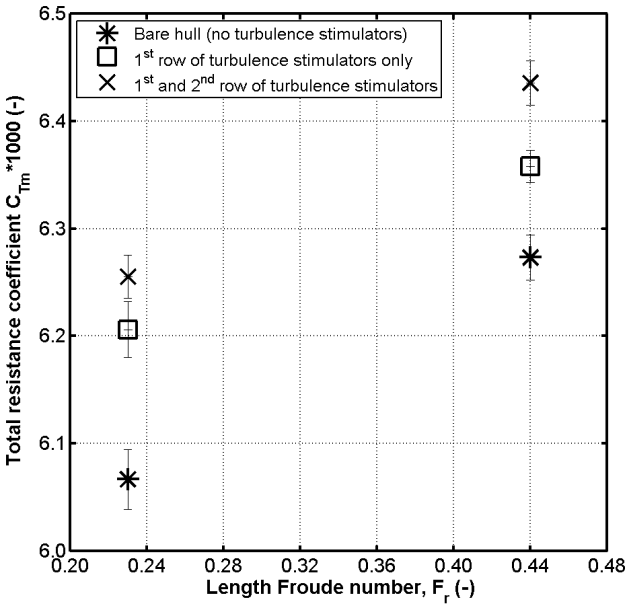

Figure 4.11: Comparison of total resistance coefficients from bare-hull without turbulence stimulators attached, a single row of turbulence stimulators and two final rows of turbulence stimulators.

The comparison of the total resistance coefficients (C_{Tm}) for different arrangements of turbulence stimulators show that there is a measurable difference in change of resistance based on the number of rows of turbulence stimulators attached to the model. The turbulence stimulator condition selected for all the experimental testing was to use both rows of turbulence stimulators. From the turbulence stimulator testing results, a stud drag coefficient was derived and subtracted from the drag used for the full scale resistance prediction. The stud drag coefficient, for each tested speed, was based on a line of best fit from the turbulence stimulator resistance results, where the line of best fit was calculated from the averaged turbulence stimulator resistance results from multiple runs.

4.4.6 Correlation Coefficient

Model experiments are carried out using smooth surface models with turbulence stimulators but full scale ships have some roughness on their surface and propulsion systems. The effects of surface roughness (e.g. paint, fouling, and corrosion) are included in an allowance coefficient, which is added to the smooth residual resistance and surface friction coefficients when determining the overall drag of a full scale ship. ITTC (1978) adopted the allowance coefficient (C_A) of Bowden et al. (1974), shown in Equation 4.10, to be used with the ITTC 1978 performance prediction line for ship resistance where the coefficient is a function of mean hull roughness average peak of peak-to-trough roughness height measured over 50 mm sampling lengths on the hull surface. The correlation allowance (C_A) incorporates the correction factors for hull roughness and still air resistance and is used as a general correction

factor with physical significance as opposed to simply using an ad hoc quantity (i.e. "fudge factor").

$$C_A = \left[105 \left(\frac{k_s}{L_{WL}}\right)^{\frac{1}{3}} - 0.64\right] \times 10^{-3} \tag{4.10}$$

ITTC Procedure 7.5-02-03-01.4 separated the roughness allowance (ΔC_F) shown in Equation 4.11 and the correlation allowance (C_A) shown in Equation 4.12. Total full scale resistance coefficient (C_{TS}) of a ship without bilge keels is then calculated using Equation 4.13.

$$\Delta C_F = 0.044 \left[\left(\frac{k_s}{L_{WL}}\right)^{\frac{1}{3}} - 10\ R_e^{-\frac{1}{3}}\right] + 0.000125 \tag{4.11}$$

$$C_A = (5.68 - 0.6\ log\ R_e) \times 10^{-3} \tag{4.12}$$

$$C_{TS} = (1 + k)\, C_{FS} + \Delta C_F + C_A + C_R + C_{AAS} \tag{4.13}$$

Using a correlation allowance as described by Bowden et al. (1974) or ITTC (2011a) results in a higher correlation allowance than is normally used for catamaran model testing and this is most likely due to using a typical value for roughness height of the hull (k_s) when there is no dedicated roughness database available at the testing facility. Tests carried out by MARIN (2008) used a correlation allowance (C_A) of 0.00035 and this value was adopted as the general correlation allowance for the waterjet performance analysis presented in this thesis.

4.4.7 Trim Tab Optimisation Tests

The experimental program included a trim tab optimisation test to determine the optimal trim tab angle setting to be used in all experiments. The speeds tested were 25, 26 and 27 knots (F_r = 0.43, 0.45 and 0.47). Three different trim tab settings were tested for a single displacement of 1,500 tonnes: firstly with the tab parallel to the baseline (defined as 0 degrees), then with angles of 5 and 10 degrees downwards compared to the baseline. The trim tab was designed to allow angles of up to 20 degrees to be set using a central locking mechanism located between the waterjet nozzles as shown in Figure 4.12. To allow accurate setting of the trim tab angles markings were added to the side of the trim tab in 5 degree increments. Results showing total resistance coefficients plotted against speed for the varying trim tab angles are shown in Figure 4.13.

Figure 4.12: Stern and bottom view showing the trim tab setup. Trim tab angles can be changed by loosening the butterfly nut located between the waterjet nozzles and sliding the connecting arm downward the central slot. The markings for the trim tab angles (5 degree increments) are shown in the picture on the right hand side. Both pictures show the model demihull in bare-hull resistance test condition as the waterjet nozzles and inlets are covered.

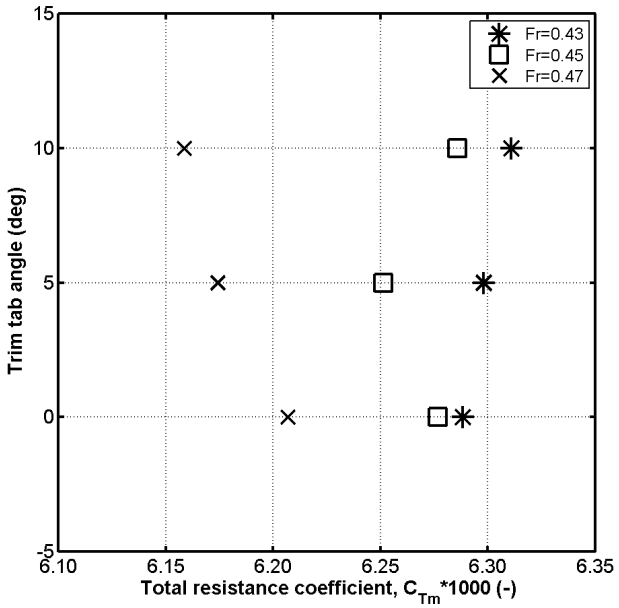

Figure 4.13: Total resistance coefficients for three trim tab angles (0, 5, and 10 degrees), three different tested speeds of 25, 16, and 27 knots (F_r = 0.43, 0.45 and 0.47), using a model equivalent displacement of 1,500 tonnes full scale (i.e. light displacement) and level static trim.

Based on these results, it was decided to use the second trim tab setting (5 degrees downward compared to the baseline) as a general setting for all experimental testing. The decision was based on the generally low resistance with trim tab setting of 5 degrees.

4.4.8 Data Reduction and Extrapolation

Data reduction and full scale resistance extrapolation followed the guidelines for bare-hull resistance tests outlined in 1978 ITTC performance prediction method and discussed in

detail in ITTC (2011a). The form factor was calculated using Prohaska's method using results from low speed resistance tests as presented in Section 4.4.4. Data reduction and extrapolation relies on using the data acquired from the bare-hull resistance test runs which included model velocity (V_m), total model resistance (R_{Tm}), heave (t_v), running trim (z_v), and water temperature of towing tank (t_w) as outlined in Section 4.4.1. The model resistance data is used to calculate non-dimensional coefficients that are extrapolated to full scale such as total resistance coefficient (C_{Tm}) shown in Equation 4.14, residual resistance coefficient (C_{Rm}), and frictional resistance coefficient (C_{Fm}) which was calculated using a friction line as described by Grigson (1993) and discussed in Section 4.4.3.

$$C_{Tm} = \frac{R_{Tm}}{\frac{1}{2}\,\rho_m\,S_m\,V_m^2} \tag{4.14}$$

The model scale residual resistance (C_{Rm}) is calculated using Equation 4-13 where (1+k) is 1.14 as determined in low speed Prohaska runs (Section 4.4.4) and for full scale residual resistance $C_{Rs} = C_{Rm}$ where C_{Rm} is calculated using Equation 4.15.

$$C_{Rm} = C_{Tm} - (1+k)\,C_{Fm} \tag{4.15}$$

Total full scale resistance of ship is determined using Equation 4.16 as discussed in 1978 ITTC performance prediction method (Procedure 7.5-02-03-01.4) published in 2011.

$$C_{TS} = (1+k)\,C_{FS} + \Delta C_F + C_A + C_R + C_{AAS} \tag{4.16}$$

Roughness allowance (ΔC_F) was calculated using Equation 4.17, where k_s is the roughness height on the hull, L_{WL} is the waterline length, and R_e is the full scale Reynolds number. As there was no hull roughness data available at the AMC towing tank, a typical value of $k_s = 150x10^{-6}$ m was used.

$$\Delta C_F = 0.044\left[\left(\frac{k_s}{L_{WL}}\right)^{\frac{1}{3}} - 10\,R_e^{-\frac{1}{3}}\right] + 0.000125 \tag{4.17}$$

Correlation coefficient (C_A) was calculated using Equation 4.18, where R_e is the full scale Reynolds number.

$$C_A = (5.68 - 0.6\,log\,R_e) \times 10^{-3} \tag{4.18}$$

Air resistance coefficient (C_{AAS}) was calculated using Equation 4.19, where A_{Vs} is the projected area of the ship above the waterline to the transverse plane, S_s is the wetted surface area of the ship, ρ_A is the air density (1.2041 Kg/m^3, air density at 20° C and 101.325 kPa.), ρ_s is the water density (1,025 Kg/m^3), and C_{DA} is the air drag coefficient of the ship above the waterline. An air drag coefficient of $C_{DA} = 0.446$ was used for the determination of the air resistance coefficient (C_{AAS}) and was based on research carried out by Oura et al. (2007)

related to manoeuvrability of a wave-piercing high-speed catamaran at low speed in strong wind. This research and a discussion with Incat Tasmania showed that an air drag coefficient (C_{DA}) of 0.446 is valid for a range of Incat Tasmania designed vessels and was therefore used for full scale resistance extrapolation of the tested model demihull.

$$C_{AAS} = C_{DA} \frac{\rho_A \, A_{Vs}}{\rho_s \, S_s} \tag{4.19}$$

For the model scale resistance data to be used together with the waterjet self-propulsion test the resistance data has to be corrected for differences in water temperature between bare-hull resistance and self-propulsion tests using Equation 4.20, where C_{FMC} is the frictional resistance coefficient at the temperature of the self-propulsion test.

$$R_C = \frac{(1+k)\, C_{FMC} + C_R}{(1+k)\, C_{FM} + C_R} R_{TM} \tag{4.20}$$

Thrust deduction (t) can be calculated using the results of the bare-hull resistance test together with the thrust established in the waterjet self-propulsion test as shown in Equation 4.21, where T_G is gross thrust, F_D towing force, and R_C temperature corrected resistance.

$$t = \frac{(T_G + F_D - R_C)}{T_G} \tag{4.21}$$

Thrust deduction (t) can also be determined using results of waterjet self-propulsion test only. A discussion of this method and results comparing both methods are presented in Section 4.6.5.

4.4.9 Test Results

A comparison of the measured resistance results for two tested displacements (1,500 and 1,804 tonnes) with three different static trim conditions for each displacement (level trim, -0.5 degrees by bow, and 0.5 degrees by stern) is shown as non-dimensional resistance (R_{Tm}), and total resistance coefficient (C_{Tm}) plotted against length Froude number in Figure 4.14. Comparisons of running trim as well as heave for all six tested conditions plotted against length Froude number is shown in Figure 4.15. A comparison of full scale effective power ($P_E = R_{BH}V$), for all six tested conditions, plotted against ship speed is shown in Figure 4.16.

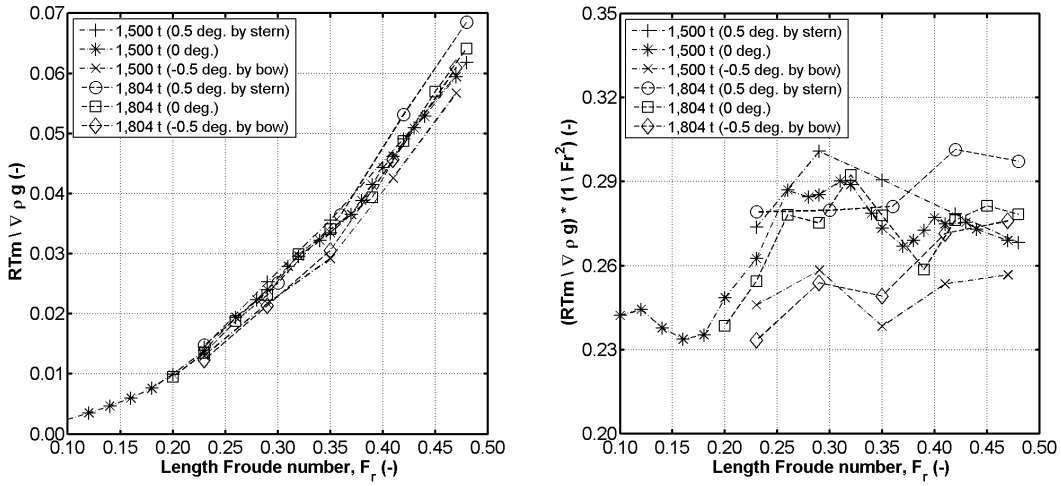

Figure 4.14: Non-dimensional total resistance and total resistance coefficient plotted against length Froude number for two displacements with three different static trims for each displacement.

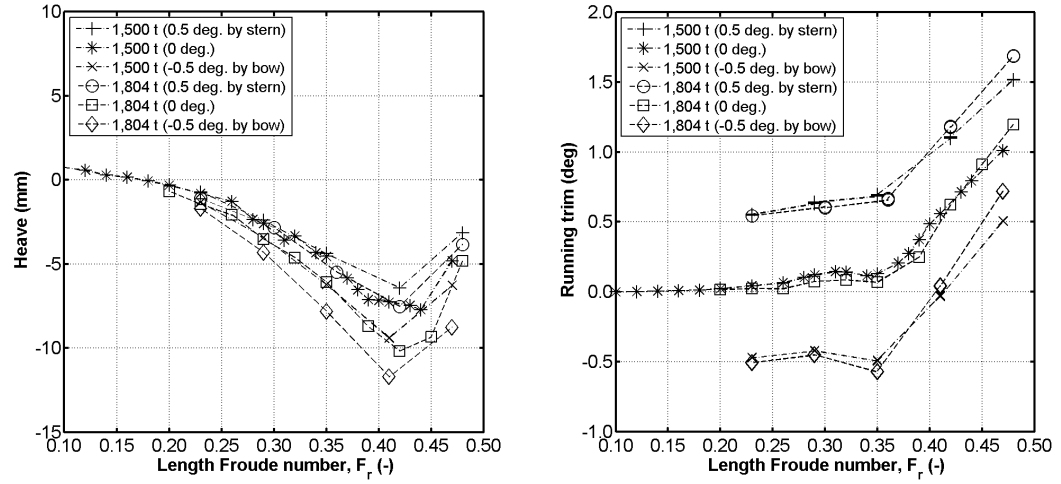

Figure 4.15: Running trim and heave plotted against length Froude number for two displacements with three different static trims for each displacement.

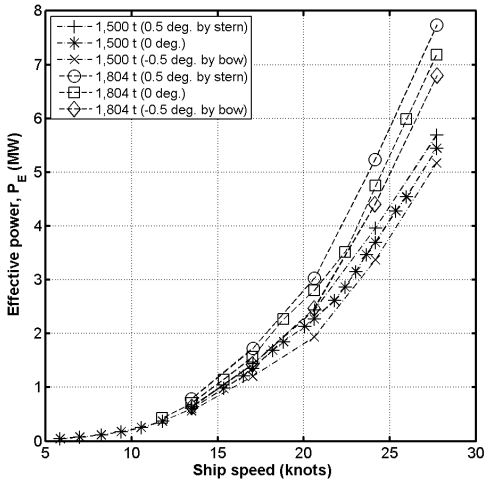

Figure 4.16: Full scale effective power plotted against length Froude number for two displacements with three different static trims for each displacement.

The resistance results (Figure 4.14) show that the hump speed (i.e. vessel speed at which maximum trim occurs) for a displacement of 1,500 tonnes and level trim (the condition tested in the waterjet self-propulsion test) occurs at a Froude length number of $F_r = 0.37$ and this is the speed regime at which the waterjet self-propulsion testing was carried out, as discussed in the waterjet test program in Section 4.4.2.

For the bare-hull resistance condition all appendage drag was deducted from the resistance results. The only appendage drag component for this was the drag by the turbulence stimulator studs as discussed in Section 4.4.5, and which resulted in a deduction of model resistance between 0.3 and 1.0 N in the length Froude number range of 0.23 to 0.44. Shallow water effects were taken into account in the resistance analysis and corrections were calculated following ITTC resistance tests guidelines which include blockage and depth corrections based on Tamura (1975), Schuster (1955), and Scott (1970). Corrections for all three stated methods were calculated and the difference in uncorrected to corrected resistance ranges from 1 to 2.5% for Tamura, 1 to 12% for Schuster, and 3 to 7% for Scott in the applicable Froude length and depth Froude number ranges.

The depth Froude number (F_{rh}) for the model resistance test ranged from 0.2 to 0.8 for model speeds of 0.65 to 3.05 m/s (i.e. full scale 6 to 28 knots). Differences in resistance results using the three mentioned blockage and depth correction methods are shown in Figure 4.17 and the selected method for shallow water corrections of the model resistance data is Schuster as this method accounts for blockage as well as wave effects.

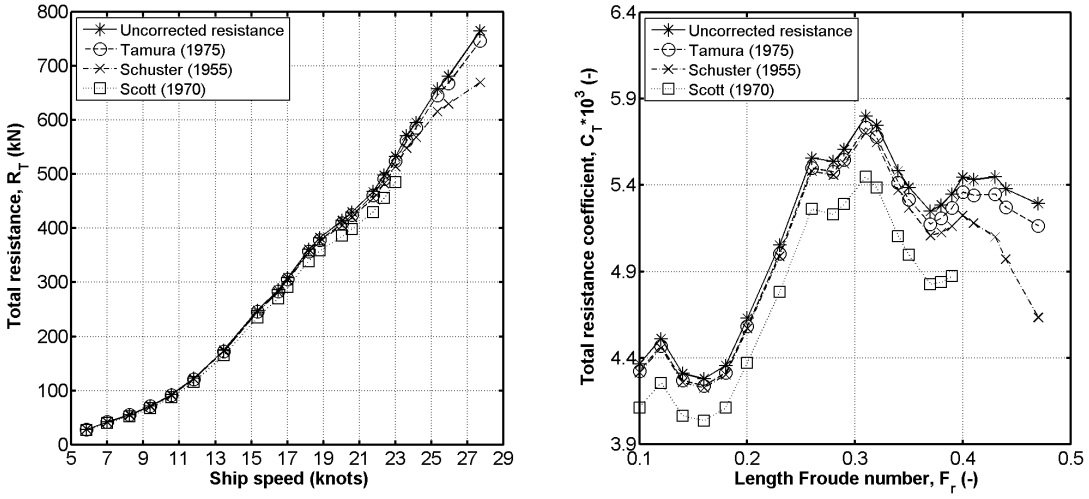

Figure 4.17: Comparison of full scale bare hull resistance plotted against corrected resistance using blockage and depth corrections based on Tamura, Schuster, and Scott methods as described by ITTC resistance test procedure 7.5-02-02-01.

Another way to look at the change of resistance for the six tested conditions is using a comparison of hull sinkage, running trim and measured resistance. The results for the light displacement test, 1,500 tonnes, are shown in Figure 4.18 and the results for the heavy

displacement, 1,804 tonnes, are shown in Figure 4.19. Maximum measured heave was -9.4 mm for a displacement of 1,500 tonnes at a static trim of 0.5 degrees by stern and -11.7 mm for a displacement of 1,804 tonnes at a static trim of 0.5 degrees by stern.

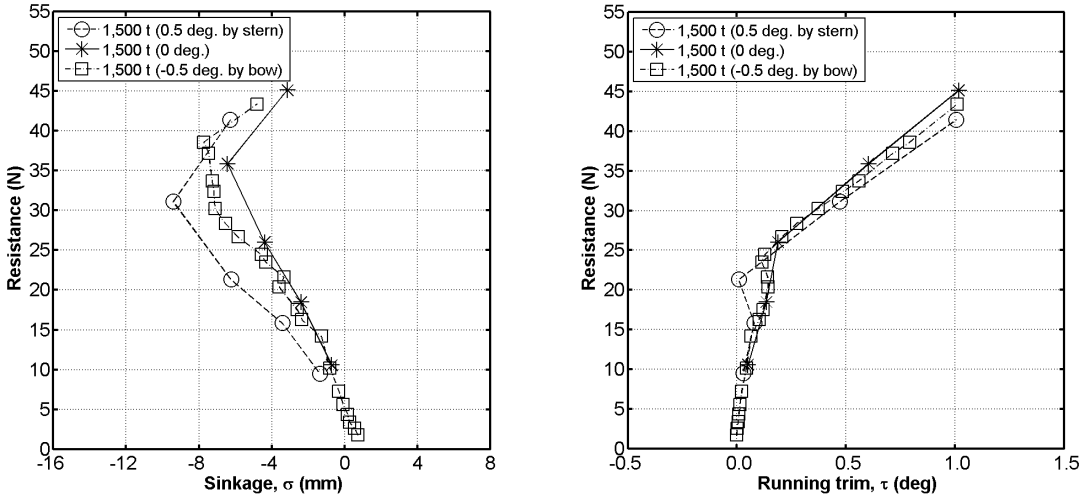

Figure 4.18: Resistance variations against sinkage and trim variations for 98 m Incat wave piercing catamaran for 1,500 tonnes displacement and -0.5, 0, and 0.5 degrees of static trim.

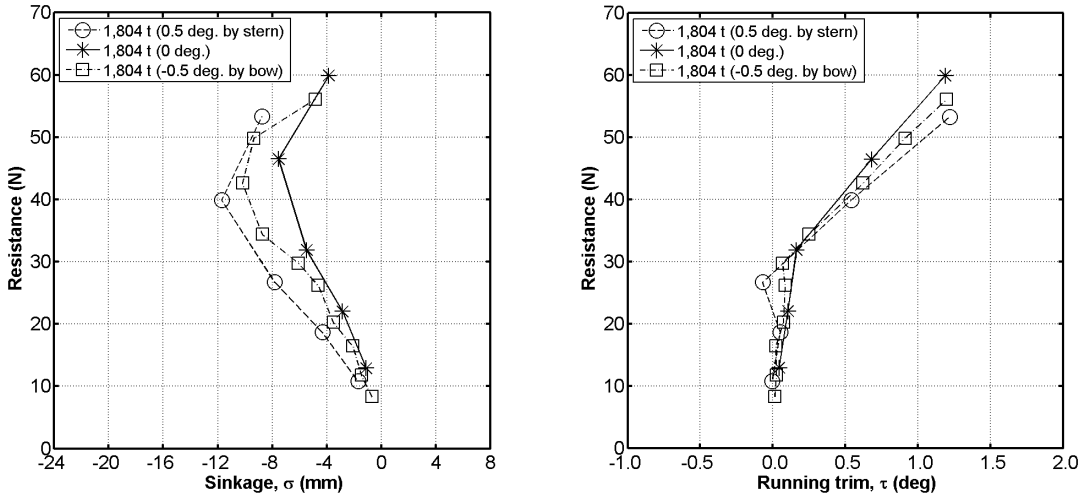

Figure 4.19: Resistance variations against sinkage and trim variations for 98 m Incat wave piercing catamaran for 1,804 tonnes displacement and -0.5, 0, and 0.5 degrees of static trim.

4.4.10 Uncertainty Analysis Results

An ITTC based resistance uncertainty analysis, using the results of the bare-hull resistance test measurements, was carried out using uncertainty analysis methodology discussed in Appendix D. Bias and error components taken into account for the bare-hull resistance uncertainty analysis are outlined in Section D.1 of Appendix D and included geometrical, alignment, calibration, direct measurement, and data reduction errors. Resistance uncertainties were calculated for two displacements (1,500 and 1,804 tonnes), three different static trim conditions for each displacement (level trim, -0.5 degrees, and 0.5 degrees), a length Froude number range of 0.2 to 0.5 and are presented in relation to total resistance coefficient (C_T) in Figure 4.20.

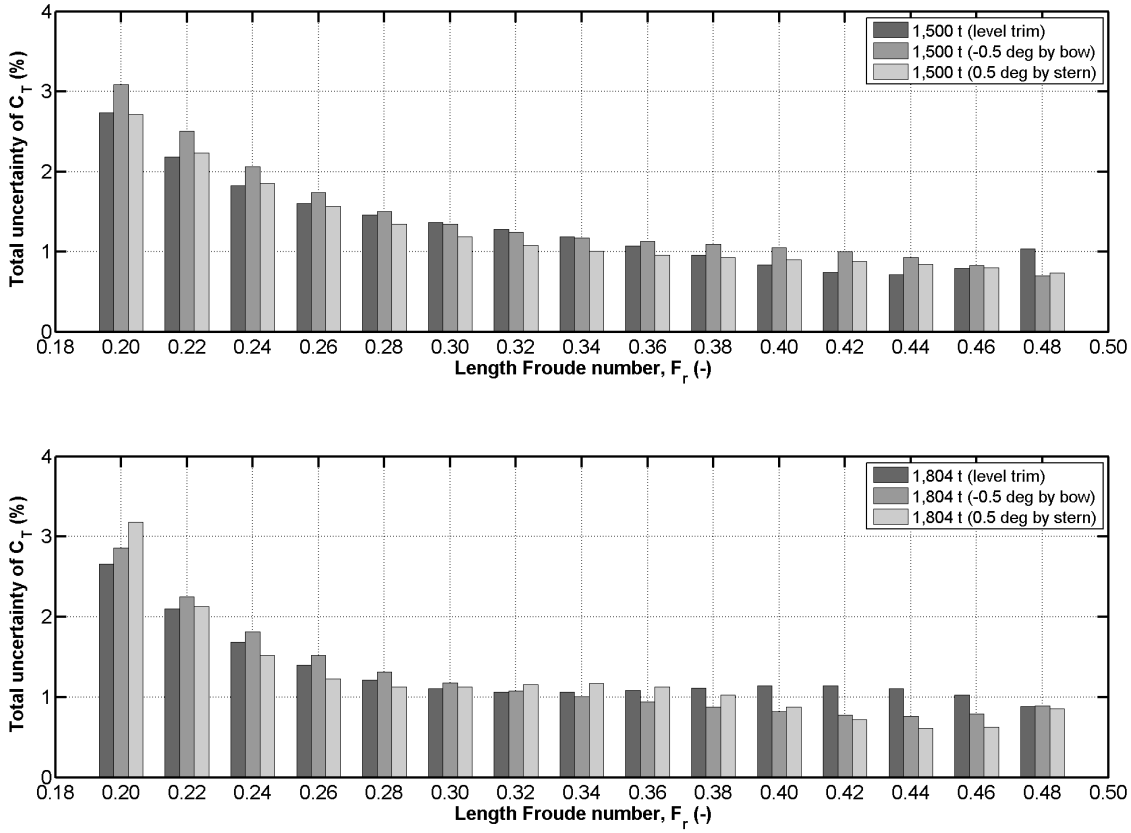

Figure 4.20: Summary of total uncertainties in relation to total resistance coefficient (C_T) for two different displacements (1,500 and 1,804 tonnes), three different static trim conditions (level trim, -0.5 degrees, and 0.5 degrees), and a length Froude number range of 0.2 to 0.5.

A comparison of uncertainties for resistance measurements in a length Froude range of 0.1 to 0.2 using resistance measurement test results measured using a displacement of 1,500 tonnes at level trim and deep transom (about 3% of static trim by bow) form factor testing using Prohaska's method (see Section 4.4.4) is given in Figure 4.20. Resistance uncertainties of a length Froude number range of 0.1 to 0.2 are very high (up to 11% at a length Froude

number of 0.1) which is also reflected in the large scatter and bad linear fit of form factor measurement results shown in Figure 4.8. Resistance uncertainties are even higher (up to 18% at a length Froude number of 0.1) for the resistance results for the testing based on Prohaska's method for form factor estimation using a deep transom condition (i.e. at about 3% of static trim by bow).

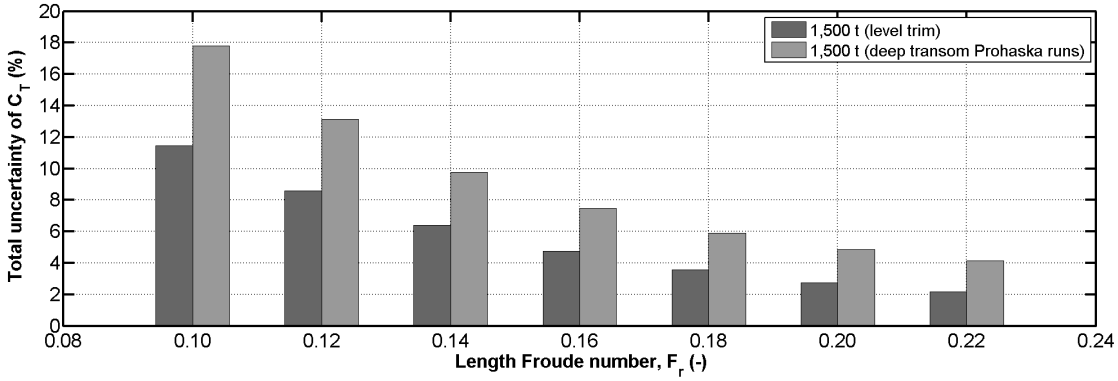

Figure 4.21: Summary of total uncertainties in relation to total resistance coefficient (C_T) for two different displacements (1,500 and 1,804 tonnes), three different static trim conditions (level trim, -0.5 degrees, and 0.5 degrees), and a length Froude number range of 0.2 to 0.5.

4.5 Static Waterjet Flow Rate Test

Accurate determination of the waterjet flow rate is crucial for applying the momentum flux method. ITTC (2011c) recommends two methods to measure flow rate; either by using Differential Pressure Transducers (DPTs) through nozzle (e.g. averaging Pitot-static tube through nozzle) or Laser Doppler Velocimetry (LDV) measurements of velocities in cross-sectional area and integration of velocities. The Differential Pressure Transducer (DPT) equipment was the most cost effective method of measuring flow rates.

Instead of using an averaging Pitot-static tube through the nozzle a slightly adjusted method of flow rate measurement was adopted as discussed in Zürcher et al. (2013). This consisted of using a single Kiel probe at each nozzle, together with a Differential Pressure Transducer (DPT), to record a reference measurement at the nozzle in the waterjet self-propulsion test which is then used in conjunction with a static flow measurement test to establish the waterjet flow rates. The major advantage of using Kiel probes compared with other total pressure probes is the complete insensitivity to direction of flow within certain limits.

For a static flow rate measurement test there are several options on how to capture the mass flow rate, such as by weight as described by van Terwisga (1996) and Jessup et al. (2008), or volumetric changes as a function over time or the change of mass of water as a function over time. The method used in this project was the change of mass of water over time and the main objective of this method is the use of the model waterjet propulsion systems to fill

a bucket (hence the given name: "bucket test") using a series of shaft speeds and measure the change of mass of water as a function of time to give mass flow rate ($\dot{m}$).

A new flow rate measurement method was introduced by Eslamdoost (2014), which should be considered for future waterjet testing and was added to the general recommendations for future waterjet testing discussed in Section 7.1. As this new method was not available in any published work when the experimental testing for the research presented in this thesis was carried out, this method was not included in the planning of experimental testing. For the Eslamdoost (2014) presented method, a T-junction was used to redirect the nozzle discharged flow perpendicular to the nozzle exit and then an axial momentum flux balance equation was used to establish volumetric flow rate. To determine flow rate using the methodology of the new testing method, two tests have to be carried out for each speed measured considered for the waterjet self-propulsion test. The first test, without T-junction, determines sinkage, trim and pump revolution at the self-propulsion point and the second test, carried out at the established shaft speed at the self-propulsion point, measures flow rate using the T-junction.

4.5.1 Test Conditions, Setup and Instrumentation

The tests were conducted in the AMC model test basin and, as shown in Figure 4.22, for the static flow measurement test setup the nozzles of the two waterjets in the demihull model were attached through pipes to a bucket. The waterjets pumps were then run at a series of shaft speeds and for each speed the collected water in the bucket was recorded as a function of time. A practical disadvantage of this method was that the bucket had to be emptied at the end of each test run, making the testing procedure very time consuming. A schematic representation of the waterjet flow rate test setup and data acquisition system is given in Appendix D.

Figure 4.22: Setup of waterjet flow rate measurement test using the AMC model test basin (MTB). The picture shows the model demihull with the model waterjet system attached to the collection bucket using the two pipes leading through the bucket wall. The Kiel probes attached to the nozzle slot into the pipes and the edge of the connection, where the nozzle connects to the pipe, was sealed to prevent water from seeping in other than the one supplied by the waterjet pump.

The quantities and units shown in Table 4.6 were measured for the static flow rate measurement test, where the mass flow rate, shaft speed, reference measurement, impeller thrust and shaft torque were measured separately for both (port and starboard) propulsion systems.

Table 4.6: Quantities And Units Measured For Static Flow Measurement Test.

Measurement	Unit
Mass flow rate (ρQ_J or $\dot{m}$) using an analog wave probe	Kg/s
Reference measurement at nozzle (P_n)	Volt
Shaft speed (n)	RPM or RPS
Impeller thrust (T_I)	N
Shaft torque (T_Q)	Nm

The bucket, shown in Figure 4.23, had a capacity of about 525 Kg of water, so it could be used to record up to 100 seconds of data at the highest tested shaft speed of 3,400 RPM. The maximum shaft speed was set at 3,400 RPM due to the limitation of a maximum rated speed of 3,500 RPM for the dynamometers used to measure impeller thrust and shaft torque.

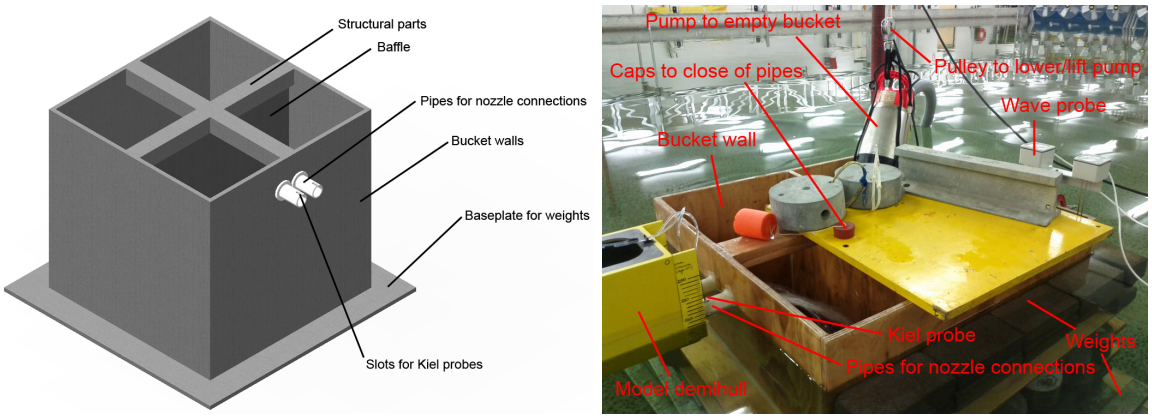

Figure 4.23: 3D of design (left) and final (right) version of water collection bucket used for static flow measurement testing. The bucket contained a central baffle; on one side the baffle water enters the bucket and the wave probe measures the flow rate on the other side of the baffle with lessened surface disturbance to reduce measurement error.

The wave probe used for the determination of the mass flow rate shown in Figure 4.24 was calibrated twice, once at the start of the flow rate measurement test and once at the end to check that the calibration factor had not changed due to changes in water temperature or other variables.

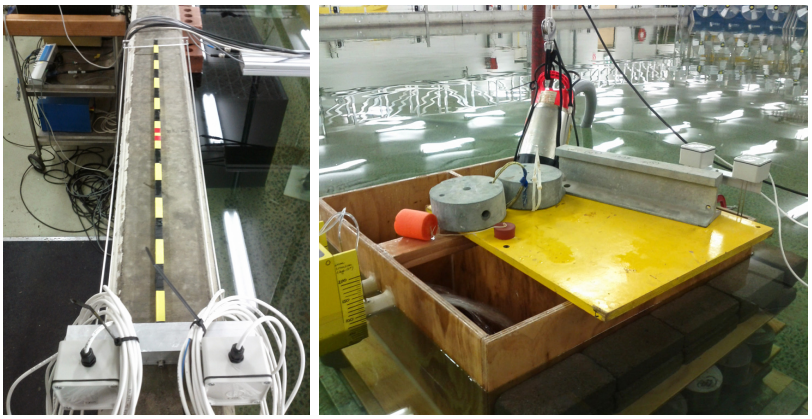

Figure 4.24: Custom analog wave probe used to measure change of mass of water in the bucket as a function of time (left) and installed in the bucket (right). The yellow board was used to prevent splashing of water from the waterjets outside the bucket.

The calibration of the analog wave probe was carried out by adding water to the bucket in increments of 25 Kg (measured using a scale) then adding the water to the bucket and recording the new voltage output of the wave probe for each incremental change to create a mass (Kg) versus wave probe output (voltage) plot as shown in Figure 4.25. For each test run, the change in voltage (i.e. change in mass of water) was recorded and together with the sampling time resulted in the measured mass flow rate ($\dot{m}$) being obtained for each test run.

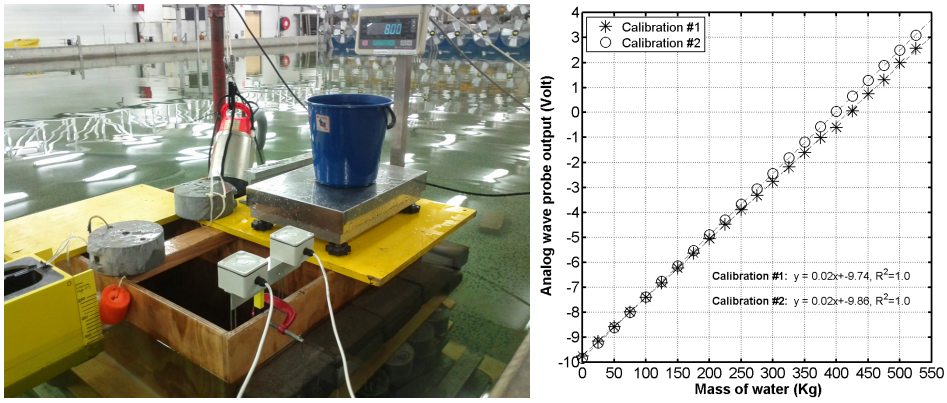

Figure 4.25: Calibration plot of analog wave probe for a change of mass of water of 525 Kg in increments of 25 Kg. The plastic bucket together with the scale was used to measure 25 Kg increments of water, which was then added to the bucket, and at each increment the new voltage output of the wave probe was recorded to create the wave probe calibration. The plot on the right shows the two calibrated wave probe mass vs. voltage curves measured at the start and the end of the flow rate measurement test.

The Kiel probes for reference measurements were located on the centreline of the port and starboard waterjet nozzles. The stator in the waterjet nozzle was intended to remove the swirl from the nozzle exit flow so that the absolute velocity from the nozzle was essentially in line with the pump axis. The Kiel probes were mounted just aft of the waterjet nozzle exit in line with the pump axis at the 70% nozzle exit radius, as discussed in Rispin (2007).

This position was estimated to be approximately at the midpoint of the nozzle mass flow and is representative of the averaged velocity conditions of the nozzle. The Kiel probes and their locations can be seen in the stern view of the nozzles in Figure 4.26 and the Induction Proximity Sensors and the Cussons Dynamometers are shown in Figure 4.27. The sampling frequency for this test was set at 800 Hz (800 samples for each second) to allow enough resolution for the Induction Proximity Sensors to accurately record the shaft revolutions at the highest shafts speeds.

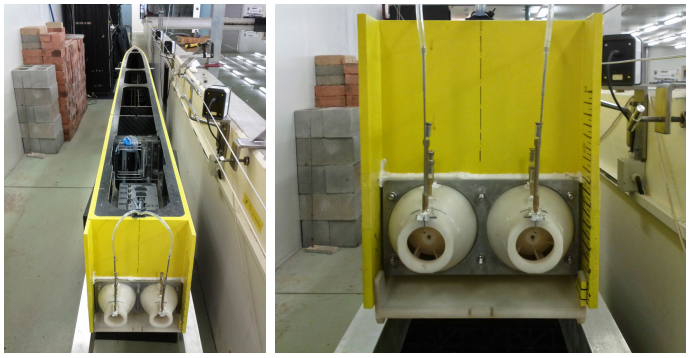

Figure 4.26: Locations of Kiel probes used for flow rate reference measurements combining the static flow rate measurement test results and the results from the waterjet self-propulsion test. The Kiel probes are located on the nozzle centreline, in line with the pump axis at the 70% nozzle exit radius which is approximately at the midpoint of the nozzle mass flow and is representative of the averaged velocity conditions of the nozzle.

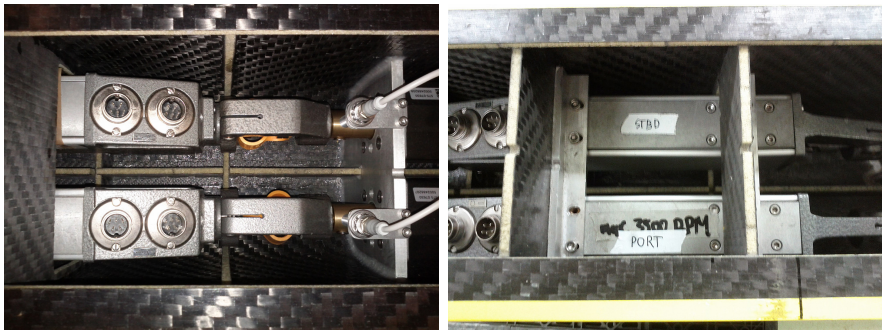

Figure 4.27: The left picture shows two AM9-10 analog induction proximity sensors by Automation Direct Pty Ltd installed above the shaft connector (connecting electric motor and dynamometer) and the right picture shows two installed type R31 Cussons model self-propulsion propeller dynamometers as used for impeller thrust and shaft torque measurements in the flow rate and waterjet self-propulsion tests.

4.5.2 Test Program

The static waterjet flow rate measurement test program was conducted for the port and starboard waterjet propulsion systems independently and the tests were carried out for a shaft speed range of 800 to 3,400 RPM, in increments of 200 RPM for a total of 14 measurements for each propulsion system. Every second run of the flow rate measurement test was repeated three times to determine the repeatability of the test results.

4.5.3 Data Reduction

As stated in Section 4.5.1, the measurements recorded in the flow rate measurement test included mass flow rate, the nozzle reference measurement, shaft speed, impeller thrust, and shaft torque. The data recorded for shaft torque and impeller thrust was not really used in the analysis of the flow rate measurement test but was measured to check the correct data recording of the two installed dynamometers. The data from the wave probes and the nozzle reference measurement (i.e. Kiel probes at nozzle) for each run resulted in a reference measurement in volts and a mass flow rate in Kg/s. To obtain the flow rate from the wave probe, the change in voltage over time from the data acquisition system was used, and in conjunction with the wave probe calibration curves results in the change of flow rate over time which is mass flow rate. For analysis purposes the averaged results of the repeated test runs were used.

4.5.4 Test Results

Test results of the flow rate measurement test are summarised as mass flow rate plotted against Kiel probe output (nozzle reference measurement) and are presented in Figure 4.28 where "Series 1" refers to the results of the first flow rate measurement test and "Series 2" to the results of the second, repeated, flow rate measurement test. The slight differences in flow rates of the two tests are mostly based on calibration and temperature differences at time of testing. To complete the mass flow rates for each possible Kiel probe measurement a polynomial fit curve was fitted through the measured data.

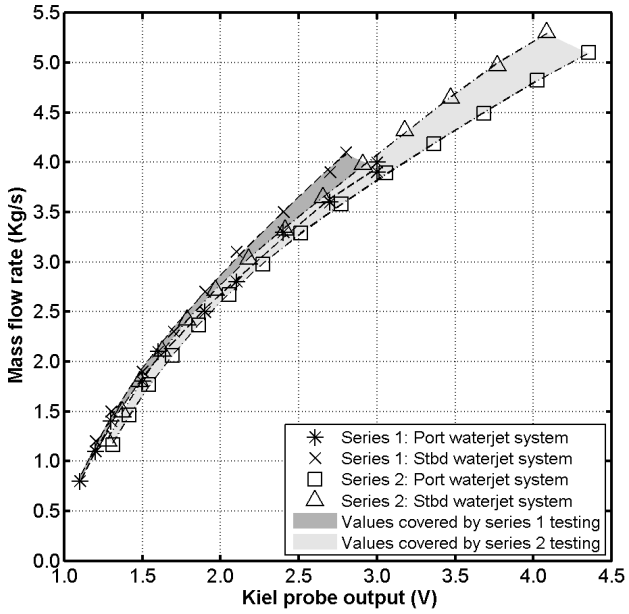

Figure 4.28: Results of two flow measurement tests using a shaft speed range of 800 to 3,400 RPM.

The flow measurement data shown in Figure 4.28 was then used to determine the mass flow rate in the waterjet self-propulsion test (Section 4.6) by finding the mass flow rate at the nozzle reference measurement for each test run. For "Series 2" results, polynomials were derived from the lines of best fit, as shown in Equation 4.22 (port waterjet system) and Equation 4.23 (starboard waterjet system). These equations then allowed the calculation of the mass flow rate with an input of a nozzle reference measurement in voltage, measured by the Kiel probes and differential pressure transducers.

$$y = -0.04x^4 + 0.57x^3 - 2.95x^2 + 7.85x - 5.20 \tag{4.22}$$

$$y = -0.09x^4 + 1.12x^3 - 4.99x^2 + 11.05x - 6.85 \tag{4.23}$$

4.5.5 Uncertainty Analysis Results

An uncertainty analysis based on the method of the American Society of Mechanical Engineers (ASME PTC 19.1-2005), using the results of the static flow rate measurements, was carried out as discussed in Appendix D. Bias and error components taken into account for the flow rate measurement uncertainty analysis are outlined in Section D.2 of Appendix D. Mass flow rate uncertainty ($U_{C\dot{m}}$) was calculated based on a shaft speed range of 1,000 to 3,400 RPM for port and starboard waterjet propulsion system and results are presented as percentage error of $C_{\dot{m}}$ in Figure 4.29.

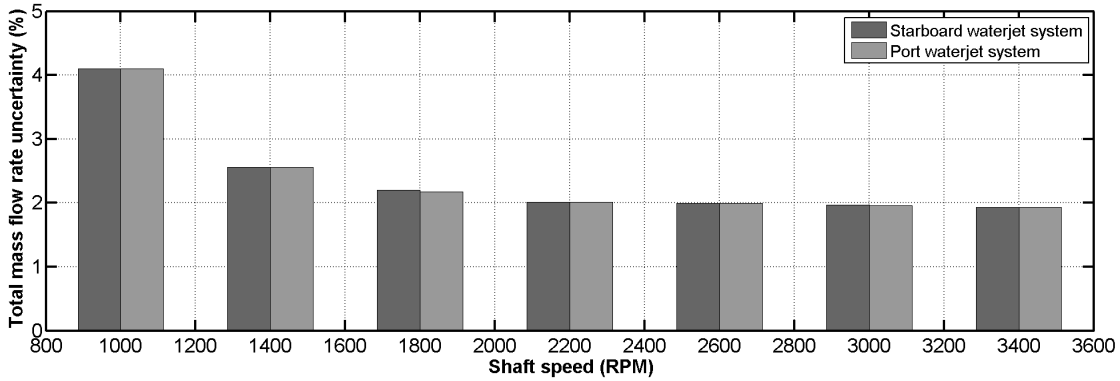

Figure 4.29: Percentage error of $C_{\dot{m}}$ for static flow rate measurement test, port and starboard propulsion system, and a shaft speed range of 1,000 to 3,400 RPM.

4.6 Waterjet Self-Propulsion Test

The purpose of model self-propulsion tests is to measure the waterjet-hull interaction effects and therefore the scaled hull model needs to be fitted with a scaled propulsion system. In

the test runs continuous recordings of tow force (drag), impeller torque, impeller rate of revolution, sinkage fore and aft (i.e. heave and trim), reference measurement for flow rate, and model speed are taken and subsequently combined with the results from the flow rate measurement test and boundary layer measurements to investigate wake fraction and thrust deduction effects.

The waterjet self-propulsion test models the ship operating conditions as closely as possible but as the Reynolds number for model scale and full scale are different, the frictional resistance also varies. To compensate for the deficiency of the frictional resistance coefficient at full scale, an extra towing force was applied to the model in the self-propulsion test to unload to propulsor. By applying this towing force, the propulsor only needs to overcome the full scale frictional resistance and an illustration showing the frictional resistance coefficient variation from model scale (C_{Fm}) to full scale (C_{Fs}) is shown in Figure 4.30.

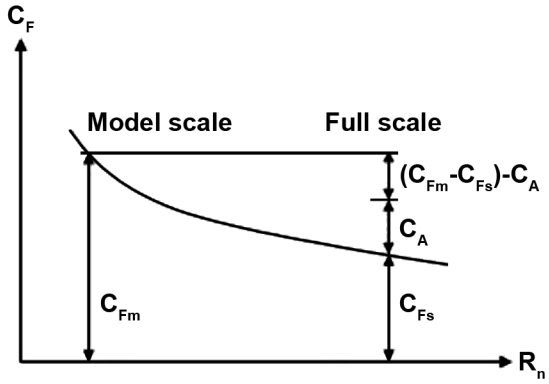

Figure 4.30: Variation of frictional resistance coefficient from model scale (C_{Fm}) to full scale (C_{Fs}) plotted against Reynolds number (R_e).

The total frictional resistance coefficient of the full scale vessel is equal to the frictional resistance coefficient at full scale obtained using the ITTC 1957 friction line, shown in Equation 4.2, plus the correlation allowance (C_A) defined in Section 4.4.6 as $C_A = 0.00035$. Correlation allowance is an empirical surface roughness correction applied to account for the larger roughness of the full scale vessel compared to the smooth surface of the model. The dimensional form of the towing force, which should be applied to the model is obtained from Equation 4.24, where ρ_m is the water density from the model test, V_m is the model speed, S_m is the wetted surface area of the model, $1+k$ is the form factor, C_{Fm} and C_{Fs} are model scale and full scale frictional resistance coefficients, and C_A is the correlation allowance.

$$F_D = \frac{1}{2}\,\rho_m\,V_m^2\,S_m\;\left((1+k)(C_{Fm}-C_{Fs})-C_A\right) \tag{4.24}$$

Form factor (1+k) used for the determination of towing force was set as 1.14 (Section 4.4.4) and the calculated towing forces for a length Froude number range of 0.24 to 0.4 are given in Table 4.7.

Table 4.7: Calculated Towing Force (F_D) Values For A Length Froude Number Range Of 0.24 to 0.4. Form Factor (1+k) Used For Towing Force Calculation Is 1.14 As Determined With Slow Speed Prohaska Resistance Test Runs.

$\mathbf{F_r}$	$\mathbf{V_m}$	$\mathbf{C_{Fm}}$	$\mathbf{C_{Fs}}$	$\mathbf{C_A}$	$\mathbf{F_D}$
-	m/s	-	-	-	N
0.24	1.56	0.0031	0.0017	0.00035	2.41
0.26	1.70	0.0031	0.0017	0.00035	2.81
0.28	1.83	0.0031	0.0017	0.00035	3.20
0.30	1.96	0.0030	0.0017	0.00035	3.60
0.32	2.08	0.0030	0.0016	0.00035	4.04
0.34	2.22	0.0030	0.0016	0.00035	4.53
0.36	2.35	0.0029	0.0016	0.00035	5.02
0.38	2.48	0.0029	0.0016	0.00035	5.51
0.40	2.62	0.0029	0.0016	0.00035	6.06

Generally there are two methods that can be used to carry out self-propulsion testing. For the first method (constant speed method) the model is restrained by the force transducer or load cell (i.e. resistance dynamometer as indicted in Figure 4.31) in a captive manner. For a certain forward speed the shaft revolution is set to a range of values and at each setting the steady-state value of model towing force, thrust and torque are recorded. The shaft revolutions are chosen in a manner that the model operates at both under- and overloaded conditions relative to the self-propulsion point of the vessel, defined by the towing force (F_D). This method is referred to as the load-varying test or the "British" method. The equivalent waterjet propulsion setup for the constant speed method is shown in Figure 4.33 and a schematic representation of the waterjet self-propulsion test setup is given in Appendix C. The second method (constant loading method) uses a fixed towing force and a sketch of the setup is shown in Figure 4.32. During a run, either the shaft loading is fixed and the model towing speed is varied within a small range to obtain a balance point, or the towing speed is fixed and the shaft revolutions are adjusted to obtain a balance point. During the test steady-states values are recorded at the balance point and this method is referred to as the "Continental" method.

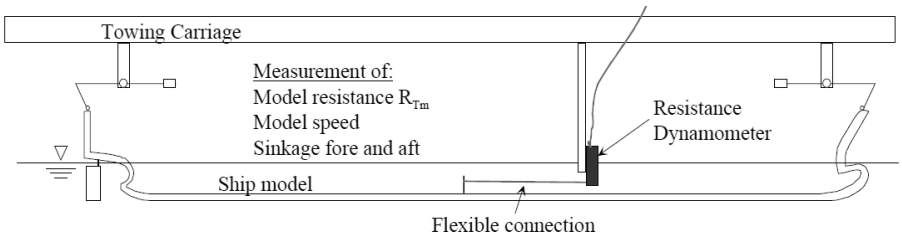

Figure 4.31: Test setup for self-propulsion tests, British method as shown in Steen et al. (2014).

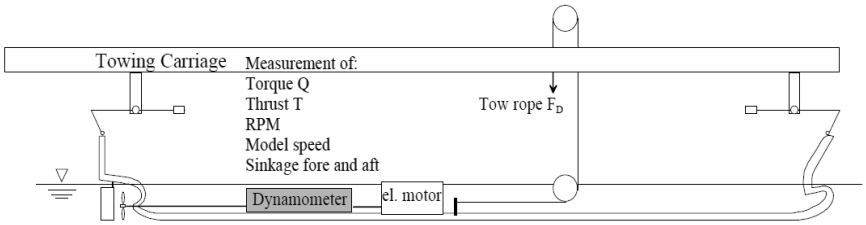

Figure 4.32: Test setup for self-propulsion tests, Continental method as shown in Steen et al. (2014).

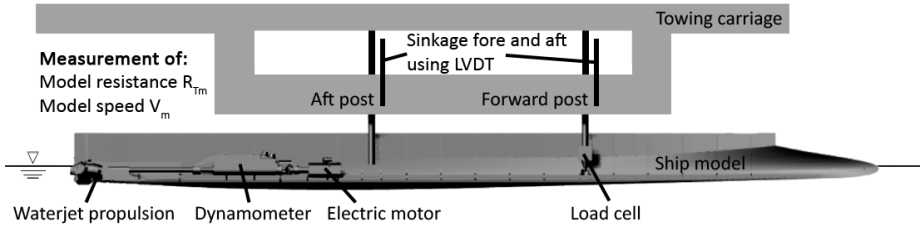

Figure 4.33: Setup for waterjet self-propulsion tests using constant speed method (British method).

In actual practice the constant speed method for different speeds and the constant loading method for different loadings are equivalent and both lead to values of drag (F), mode thrust (T_m), and model torque (Q_m) as functions of both model speed (V_m) and shaft speed (n_m). For this project the "British" constant speed method was chosen which allowed simulating the real operation conditions of trim, flow pattern and propulsor loads to be simulated.

Assumptions used in the waterjet energy model are as follows:

- The flow rate is assumed to be constant (i.e. using continuity).
- Temperature variations are assumed to be insignificant and are therefore neglected with the exception that test results were adjusted with corrections for different water temperatures on the testing dates.
- It is assumed that the vena contracta is insignificant or that the actual nozzle size results in a vena contracta matching the waterjet output area considered here. This assumption effectively sets the velocity and pressure at station 7 equal to that of station 6 (see Figure 2.1 in Chapter 2.2).
- The stream tube is assumed to have a rectangular cross section with a width of 1.3 times the impeller diameter as discussed in ITTC (1996), van Terwisga (1996) and Eslamdoost (2014). This is a typically used value for the calculation of the flow velocity in the stream tube.
- Waterjet performance evaluation was carried out using thrust identity, which sets the non-dimensional thrust equal for both model and full scale ship and is the current

ITTC standard as discussed in ITTC (2011a). This philosophy assumes that the thrust deduction fraction is the same for both model and full scale ship when the model thrust coefficient is equal to the full scale ship.

4.6.1 Setup and Instrumentation

Table 4.8 describes the quantities and units that were measured for the waterjet self-propulsion test and includes four sensors already used for the bare-hull resistance test (i.e. speed, sinkage and resistance) as discussed in Section 4.4.1. Boundary layer measurements used two PCA-8-KL pitot tubes supplied by United Sensors Corp. and two PX142-005D5V Differential Pressure Transducers (DPTs) supplied by Omega Engineering Inc. to measure velocities at defined vertical distances below the hull at the waterjet inlet. The vertical distances from the hull were defined in 10 mm increments considered small enough for good resolution of boundary layer velocity profile and set by the boundary layer traverse as discussed in Section 4.6.3. The 10 mm increments of the vertical distances from the hull were based on previous boundary layer measurements described in MARIN (2008), where a rake with multiple pitot-static tubes was used with increments of 10 mm for a boundary layer thickness of 73 mm. The measured velocities plotted against the vertical distances from the hull results in the boundary layer profile, which was then used to determine the wake fraction and the waterjet inlet velocity (V_I).

Table 4.8: Quantities And Units Measured For Waterjet Self-Propulsion Test.

Measurement	**Unit**	**Instrument**
Model speed (V_m)	m/s	Rotary sensor
Total resistance (R_T)	N	Load cell
Sinkage fore and aft (z_{SF}, z_{SA})	mm	LVDT
Running trim and running sinkage (t_v, z_v)	mm, deg.	Calculated value
Reference measurement at nozzle (P_n)	Volt	Kiel probe
Shaft speed (n)	RPM	Inductive proximity sensor
Impeller thrust (T_I)	N	Dynamometer
Shaft torque (T_Q)	Nm	Dynamometer
Boundary layer at waterjet inlet	ms/s	Pitot-static tube & DPT
Static pressure at stations 3, 4, 5 and 6	Pascal	Wall tab & DPT

A schematic representation of the waterjet self-propulsion test setup is given in Appendix C and a frame taken from test footage of a self-propulsion test run at a length Froude number 0.36 is shown in Figure 4.34.

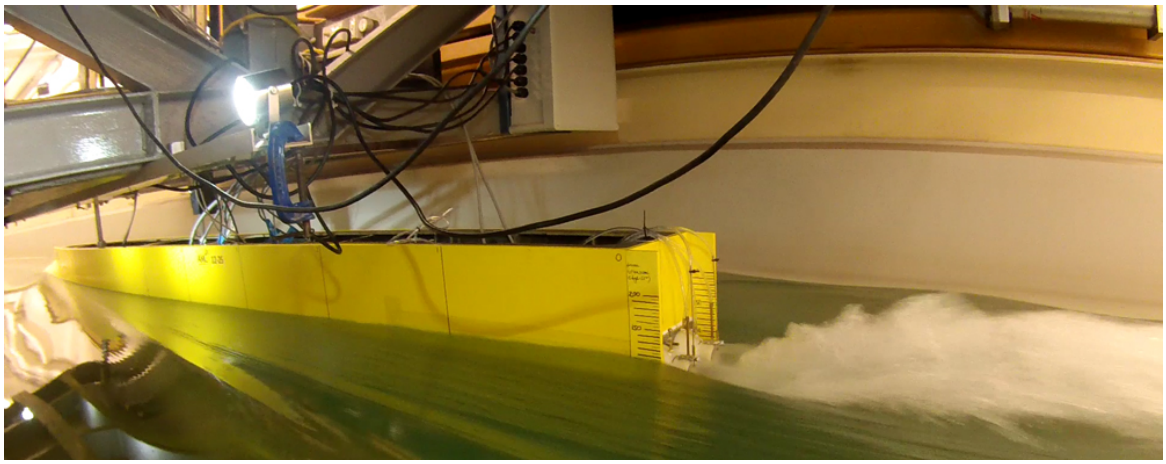

Figure 4.34: Frame taken from waterjet self-propulsion test footage with a displacement of 1,500 tonnes, level static trim, length Froude number 0.36 (V_m = 2.35 m/s.)

4.6.2 Test Program

The waterjet self-propulsion test program was divided into three test series as follows:

1. Pitot-static tube calibration measurements to create speed based calibrations of pitot-static tubes and differential pressure transducers as preparation for boundary layer velocity measurements.

2. Boundary layer measurements carried out to measure boundary layer velocity profiles for three speeds, which were set as length Froude numbers 0.3, 0.35 and 0.4 (see Section 4.6.3) used for determination of wake fractions (w) and waterjet inlet speeds using $V_I = (1 - w)V$. Compared to the tested speed range for the self-propulsion test, the three tested length Froude numbers can be considered as at the lower range, medium range and upper range speeds to provide a good comparison of boundary layer changes.

3. Waterjet self-propulsion test for waterjet performance estimation. The speed range for the waterjet self-propulsion tests ranged from length Froude number 0.24 to 0.4 in increments of 0.02 and for determination of accuracy and repeatability of results, measurements for every tested speed were repeated at least three times.

The boundary layer measurements and the waterjet self-propulsion test were carried out using a single displacement, 1,500 tones, and a single static trim, level (0 degrees), and the trim tab at the stern of the model was set at 5 degrees as determined in the trim tab optimisation test described in Section 4.4.7.

4.6.3 Boundary Layer Measurements

Pitot-static tubes were used to measure velocities. The probe measures the total and the static pressure at the location, with the difference in these two pressures being the dynamic pressure from which the velocity is calculated. In the setup for the boundary layer measurements, each pitot-static tube required only a single reading as the pitot-static tubes and the attached Differential Pressure Transducer (DPT) were calibrated in a separate test with respect to the carriage speed, such that the output of the pressure transducer was directly converted to velocity and did not require separate total and static pressure measurements. Two pitot-static tubes were used forward of the starboard side inlet for the boundary layer velocity profile data and this method for boundary layer measurements was previously used by Rispin (2007).

To measure boundary layer velocity profiles, two pitot-static tubes were installed one inlet diameter forward of the starboard model waterjet in line with the two corners of that inlet. This location spaced the two pitot-static tubes one inlet diameter apart, and they were mounted to a traverse as shown in Figure 4.35. The traverse restricts the pitot-static tubes to vertical movement only and allows the probes to be moved in 10 mm increments through two United Sensors Corp. Mounting Chucks (type USC-S8213-80) attached to aluminium inserts in the base of the hull. The traverse was not automated and the distances below the hull had to be set manually using a screw which fits into drilled holes in the boundary layer traverse railing system. The traverse had a travel of about 80mm which was sufficient to capture the boundary layer velocity profiles and the sensing end of the two pitot-static tubes below the hull location for reading of the boundary layer velocity profile at the starboard waterjet inlet is shown in Figure 4.36.

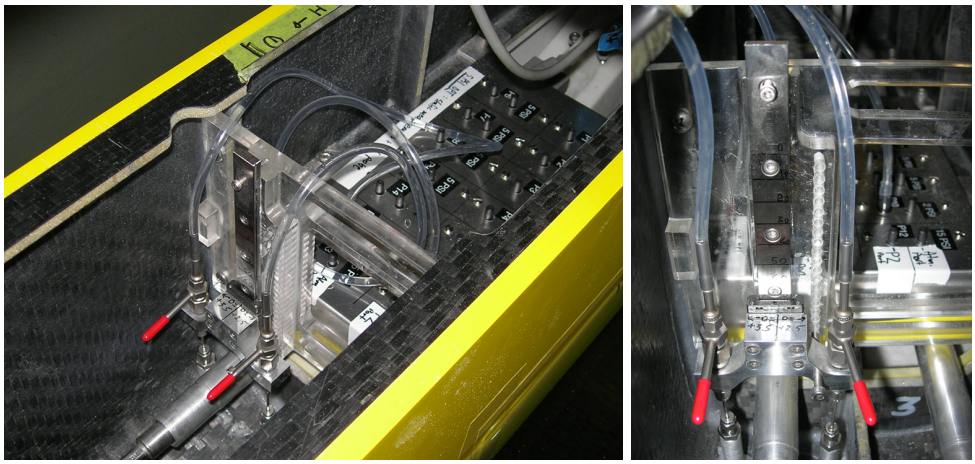

Figure 4.35: Boundary layer traverse setup showing the installation of the two pitot-static tubes and the railing system which allows the probes to be moved vertically in 10 mm increments below the model hull.

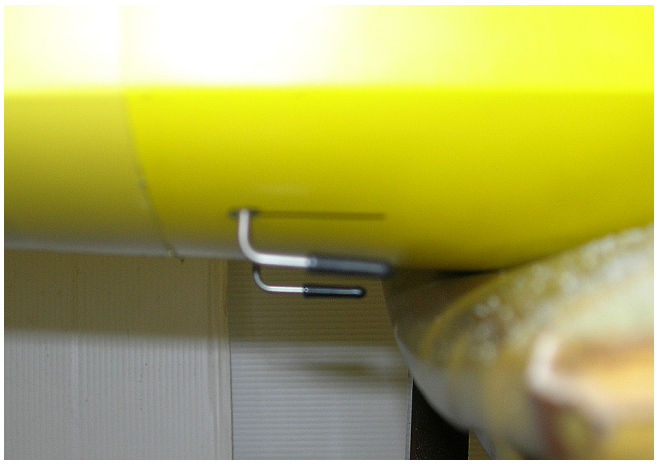

Figure 4.36: Two pitot-static tubes protruding from the hull for boundary layer velocity profile measurements. In this picture the outlets of the pitot-static tubes are covered to prevent contamination by dust.

Boundary layer traverse test runs were recorded using bare hull resistance conditions with covered waterjet inlets and nozzles. If the inlets were left open, the measured boundary layer velocity profile would be different due to the pressure gradient caused by the waterjet inlet flow, which would have to be measured accurately and would complicate the boundary layer measurement considerably. The amount of energy in the boundary layer flow upstream of the waterjet inlet is considered to be similar for the bare hull or with the inlets operating for the same vessel speed, thus making the use of the bare hull boundary layer data for performance estimations appropriate as discussed in Rispin (2007) and Jessup et al. (2008).

Results of the averaged (i.e. average of repeated runs) boundary layer velocity measurements for length Froude numbers 0.3, 0.35, and 0.4 are shown in Figure 4.37, where the measured boundary layer thicknesses (δ) were calculated as 44.2 mm for F_r = 0.3, 41.4 mm for F_r = 0.35, and 36.4 mm for F_r = 0.4 based on curves of best fit. A comparison of the non-dimensional speed $\frac{U}{U_0}$, where U_0 is ship speed, compared against the results of boundary layer measurements discussed in MARIN (2008) for a single speed of 35 knots for the 112 m JHSV wave-piercing catamaran is shown in Figure 4.38. The measured boundary layer thickness for the MARIN tests is substantially larger, being in the order of 73 mm, likely due to the larger model that was tested (6.5 m). The MARIN test was carried out for a single length Froude number of 0.57 (full scale speed 35 knots) while the length Froude numbers tested in the presented research consisted of 0.3, 0.35, and 0.4 (full scale speeds 17.6, 20.5, and 23.5 knots). A comparison of Reynolds numbers for the four presented data sets is given in the legend in Figure 4.38.

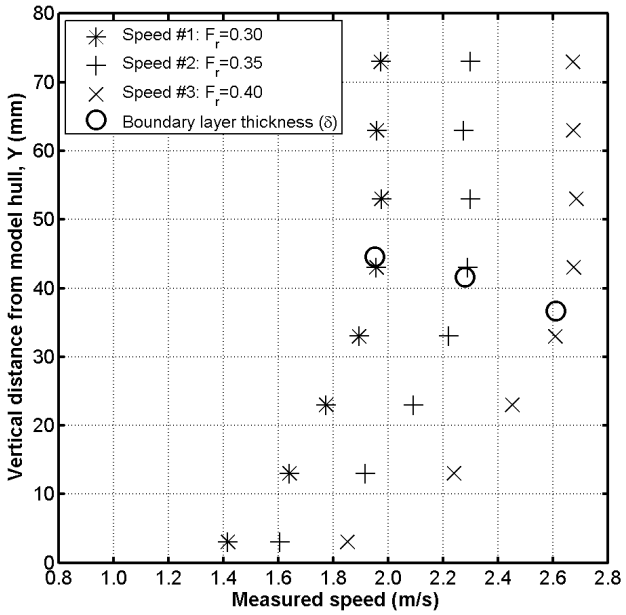

Figure 4.37: Boundary layer velocity profiles for length Froude numbers 0.3, 0.35, and 0.4 showing boundary layer thicknesses as 44.2, 41.4 and 36.4 mm based on curves of best fit.

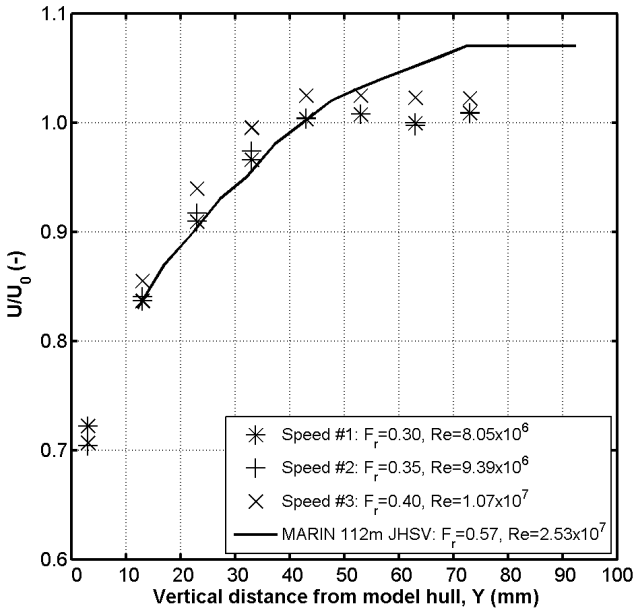

Figure 4.38: Boundary layer measurements using non-dimensional speed $\frac{U}{U_0}$ compared against the results of boundary layer measurements carried out by MARIN at a speed of 35 knots for the 112 m JHSV wave-piercing catamaran.

Inlet wake fraction can be determined using a power law trendline fitted to the velocity profile, with its defining equation and the R^2 fit. As discussed in Section 2.4, the boundary velocity profiles normally can be represented by a power law equation using a power law index of 7 for turbulent flow at model scale as discussed in Bulten (2006), MARIN (2008) and Duerr et al. (2014).

Equation 4.25 shows the characteristic boundary layer velocity profile using a power law equation where Y is the vertical distance from the hull, δ is the boundary layer thickness, U is the velocity at Y in the boundary layer, and V_0 is the ship speed (i.e. free-stream velocity). The $\frac{1}{n}$ power is significant because it defines the velocity profile in the boundary layer.

$$\frac{U}{V_0} = \left(\frac{Y}{\delta}\right)^{\frac{1}{n}} \tag{4.25}$$

It follows:

$$log10\left(\frac{Y}{\delta}\right) = n \times log10\left(\frac{U}{V_0}\right) + log10\left(\delta\right) \tag{4.26}$$

Carrying out the regression analysis, using the measured boundary layer data, has shown that the power law index is 6.65, as shown in Figure 4.39 for $F_r = 0.35$, which was used throughout the boundary layer analysis.

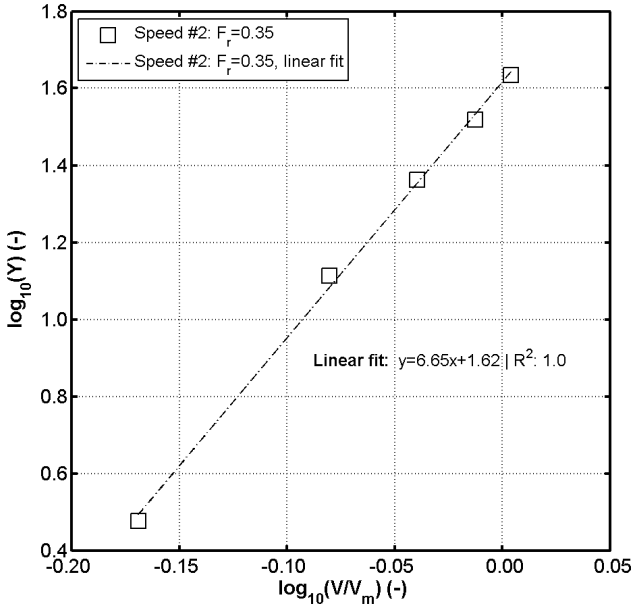

Figure 4.39: Boundary layer for $F_r = 0.35$ where the slope of linear fit equals power law index.

A comparison of the measured boundary layer velocities for length Froude numbers 0.3, 0.35, and 0.4 at a vertical distance from the hull (Y) with velocities calculated using power law (Equation 4.25) and a power law index $n = 7$ is shown in Figure 4.40. The correlation of the measured boundary layer velocities and velocities calculated using power law is good except at 3 mm distance Y of length Froude number 0.3, which is lower than the velocity calculated using the power law.

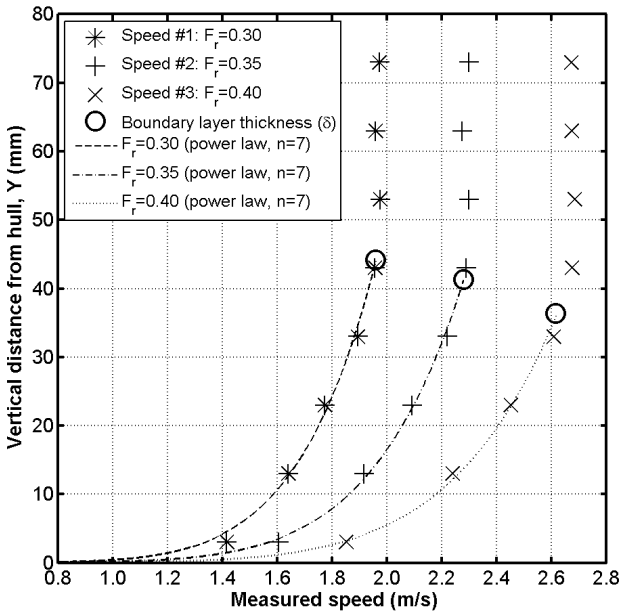

Figure 4.40: Measured velocities at a vertical distance from hull (Y) compared to calculated velocities using a power law index of $n = 7$.

Using a rectangular capture area, the volumetric flow rate inside boundary layer (Q_{BL}) was extracted from the boundary layer using Equation 4.27, where D is the width of the inlet, n is the power law coefficient, δ is the boundary layer thickness, and λ is the inlet width factor. A typical value for the inlet width factor is 1.3 for a rectangular capture area as discussed in van Terwisga (1996) and ITTC (2002).

$$Q_{BL} = \int_0^{\delta} dQ = \int_0^{\delta} V_S \left(\frac{Y}{\delta}\right)^{\frac{1}{n}} \lambda \, D dy = V_S \, \lambda \, D \, \delta \frac{n}{n+1} \tag{4.27}$$

Model scale momentum wake fraction (w_m) was determined using Equation 4.28, where n is the power law index, Q_J is measured volumetric flow rate, and Q_{BL} is volumetric flow rate inside the boundary layer.

$$w_m = 1 - \frac{V_m}{V_S} = 1 - \frac{n+1}{n+2}\left(\frac{Y}{\delta}\right)^{\frac{1}{n}} = 1 - \frac{n+1}{n+2}\left(\frac{Q_J}{Q_{BL}}\right)^{\frac{1}{n+1}} \tag{4.28}$$

Using this approach, a power law index of 6.65, measured flow rates, and calculated volumetric flow rate inside boundary layer, the momentum wake fractions were calculated for a length Froude number range of 0.24 to 0.4 and the results are shown in Table 4.9.

Table 4.9: Momentum Wake Fractions For A Length Froude Number Range Of 0.24 to 0.4.

$\mathbf{F_r}$	$\mathbf{V_m}$	$\mathbf{V_s}$	$\mathbf{w_m}$	**1-$\mathbf{w_m}$**	$\mathbf{V_{Im}}$
-	m/s	knots	-	-	m/s
0.24	1.56	14.1	0.18	0.82	1.28
0.26	1.70	15.4	0.18	0.82	1.39
0.28	1.83	16.5	0.18	0.82	1.50
0.30	1.96	17.7	0.18	0.82	1.60
0.32	2.08	18.8	0.18	0.82	1.71
0.34	2.22	20.1	0.18	0.82	1.82
0.36	2.35	21.3	0.18	0.82	1.94
0.38	2.48	22.4	0.17	0.83	2.06
0.40	2.62	23.6	0.16	0.84	2.19

Since the waterjet inlet will draw in considerable quantities of hull boundary layer flow, the inlet flow will have an overall momentum velocity that can be much less than the free-stream velocity or the speed of the ship. The lower inlet momentum velocity will affect waterjet performance and needs to be determined with a reasonable degree of accuracy. The boundary layer velocity profiles enable evaluation of the inlet wake fraction contribution (w_m), which defines the inlet speed (V_I) required for thrust calculations. Inlet speed was calculated using $V_{Im} = (1 - w_m)\, V_m$, where w_m is model momentum wake fraction, V_m is model speed (i.e. free-stream velocity), and V_{Im} is model inlet speed.

4.6.4 Self-Propulsion Points

Self-propulsion tests were carried out with a geometrically similar model of the ship and its propulsors. At each model speed (V_m) the shaft revolutions of the impeller shaft was changed such that the test is done at different values of towing force (drag). For each test run measurements were recorded of impeller shaft speed (n_m), shaft torque (Q_m), model speed (V_m), sinkage fore and aft (z_{SF} and z_{SA}), drag (R_{TM}), reference measurement to determine flow rate (using flow rate measurement results), and water temperature. At each tested speed, the values of thrust were plotted against the towing force (drag) as shown in Figure 4.41, where the linearity of these plots indicate a constant thrust deduction over a range of shaft speeds as investigated in Bose (2008) for a propeller propelled vessel. The resulting linear curve fits of the nine tested speeds, as well as the parallel distribution of the curve fits were an important result, as it showed that the tow force (i.e. drag) plotted against thrust can be used for waterjet as well as propeller performance estimation analysis.

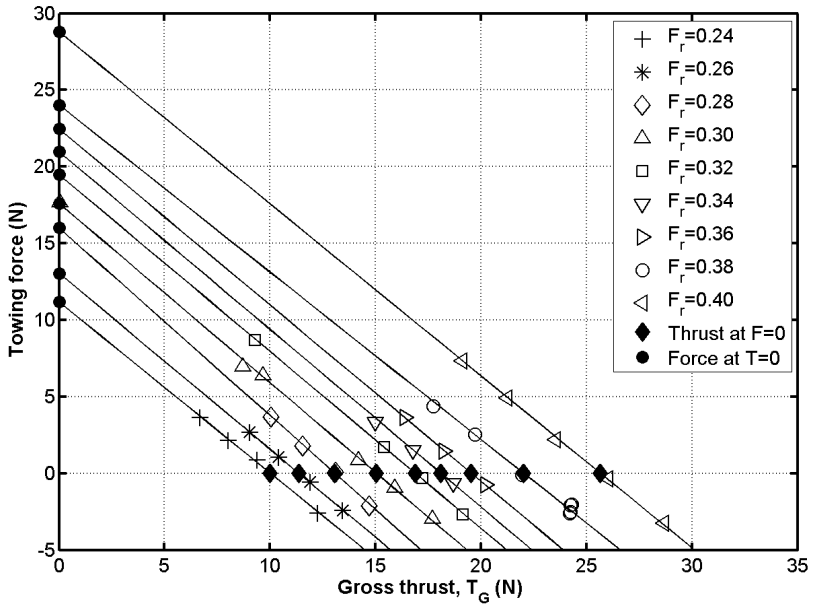

Figure 4.41: Towing force plotted against thrust using results of waterjet self-propulsion test at a displacement of 1,500 tonnes, level static trim, and nine measured speeds in the length Froude number range of 0.24-0.40.

Important values from Figure 4.41 were the cross-over of the thrust at zero drag ($T_{F=0}$) and the intercept of the fitted thrust curve with the y-axis called force at zero thrust ($F_{T=0}$). Following Bose (2008), the force at zero thrust ($F_{T=0}$) is normally somewhat greater than the towed resistance for a propeller driven vessel; but as shown in Figure 4.44, results of the waterjet self-propulsion test resulted in values of force at zero thrust ($F_{T=0}$), for all nine speeds tested, below the measured bare-hull resistance (R_{BH}). Thrust at zero drag ($T_{F=0}$) is the model self-propulsion point (i.e. no correction for skin friction). The towing force (F_D) was then used to find the thrust corrected for skin friction at the ship self-propulsion point, which was then used to scale model thrust to full scale thrust. At the self-propulsion point the propulsor is operating at the full scale point of operation and this means that the thrust coefficient (C_T) is the same for the model and full scale (i.e. thrust identity).

As discussed previously, the self-propulsion test was carried out using a load varied test method, which means that the thrust was systematically changed by varying the shaft speed while towing the model at a constant speed. The self-propulsion point was then determined by interpolating the data recorded for each measured speed. During testing the tow force was measured over a series of shaft speeds at both under-propelled (greater than resistance) and over-propelled (less than the resistance) values for a given model speed as shown in Figure 4.41, where the tow force is plotted against thrust. A linear fit was found to be appropriate for the results measured at different shaft speeds for each measured model speed and the point where the tow force (i.e. drag) becomes zero (i.e. thrust at zero drag, $T_{F=0}$) is called the model self-propulsion point. This point was then corrected for skin friction (i.e. Reynolds

number difference) to determine the full scale self-propulsion point. Results of the T-F plot (Figure 4.41) for nine tested speeds in the Froude number range of 0.24 to 0.4 are shown in Table 4.10.

Table 4.10: Results Of Towing Force (F_D), Force At Zero Thrust ($F_{T=0}$), Thrust At Model Self-Propulsion Point ($T_{F=0}$), and Thrust At Model Self-Propulsion Point Corrected For Skin Friction (T_{SPP}) For Nine Tested Speeds In The Froude Number Range of 0.24 To 0.4.

$\mathbf{F_r}$	$\mathbf{F_D}$	$\mathbf{F_{T=0}}$	$\mathbf{T_{F=0}}$	$\mathbf{T_{SPP}}$
-	N	N	N	N
0.24	2.4	10.0	11.2	7.8
0.26	2.8	11.4	13.0	8.9
0.28	3.2	13.1	16.0	10.4
0.30	3.6	15.0	17.6	12.0
0.32	4.0	16.9	19.5	13.4
0.34	4.5	18.1	21.0	13.9
0.36	5.0	19.5	22.5	15.2
0.38	5.5	22.0	24.0	16.7
0.40	6.1	25.7	28.8	19.6

Thrust at the self-propulsion point, corrected for skin friction, was found by applying the methodology described in Rispin (2007), where towing force (i.e. measured drag) was plotted against thrust at different shaft speeds and constant model speed as shown in Figure 4.42 for a length Froude number of 0.3. The intersection of the towing force (i.e. F_D = 3.6 N) curve and the thrust curve defines the model self-propulsion point adjusted for skin friction and therefore this is the full scale self-propulsion point for this measured model speed. The same methodology was also applied to find torque, shaft speed, heave, running sinkage and Kiel probe measurement at the self-propulsion point shown as an example for F_r = 0.3 in Figure 4.43.

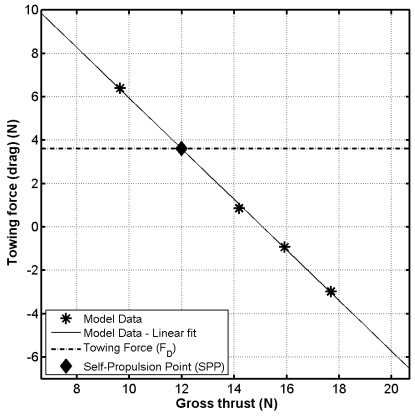

Figure 4.42: Model self-propulsion point corrected for skin friction, using towing force (F_D), for a length Froude number of F_r = 0.3. The corrected self-propulsion point is estimated by plotting towing force (i.e. measured drag) against thrust and adding a curve for calculated towing force (F_D). Intersection of F_D curve and plotted thrust curve defines full scale self-propulsion point at this model speed.

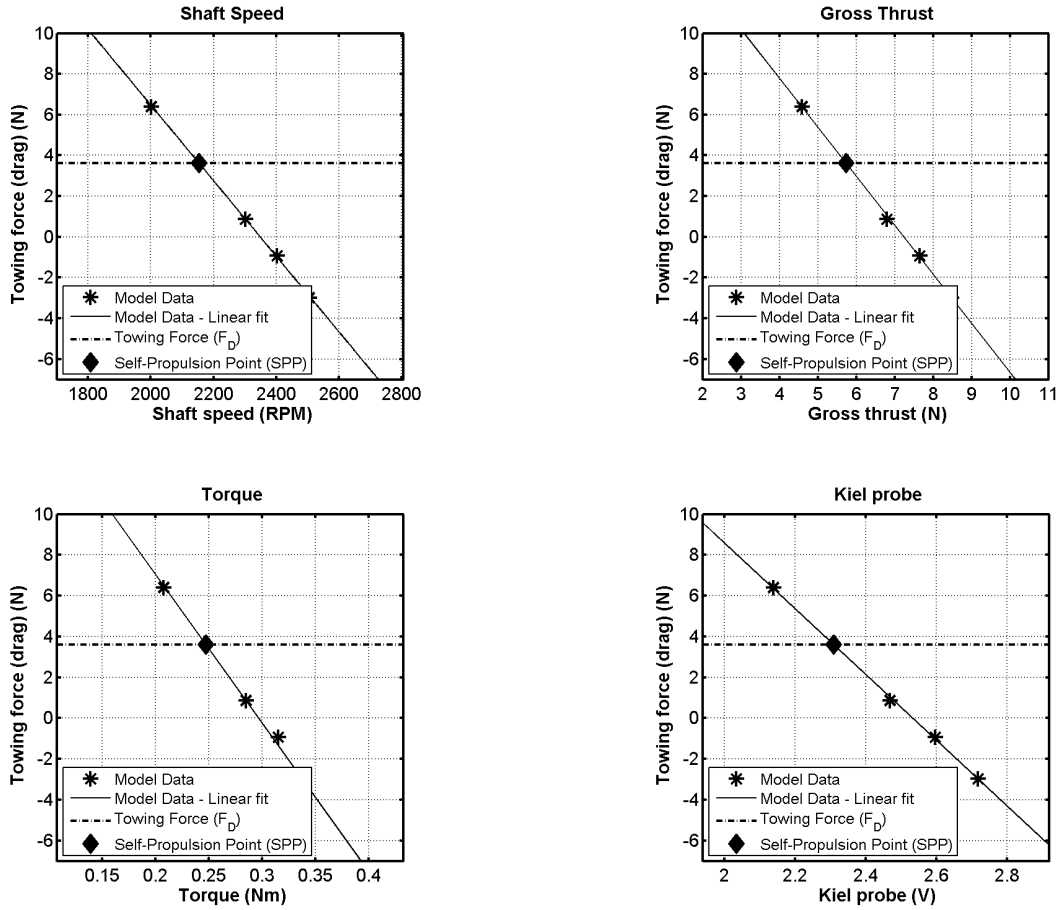

Figure 4.43: Determination of shaft speed (RPM), thrust (N), torque (Nm), and Kiel probe (V) measurement for a length Froude number of 0.3.

Final results of the calculated model waterjet performance values at the self-propulsion point are summarised in Table 4.11 showing results of a length Froude number range of 0.24 to 0.4.

Table 4.11: Calculated Performance Parameters At Self-Propulsion Point For A Length Froude Number Range Of 0.24 To 0.4 Showing Speeds, Thrust At Model Self-Propulsion Point, Shaft Speed, Torque, Heave, Trim, And Reference Kiel Probe Measurement Results.

$\mathbf{F_r}$	$\mathbf{V_m}$	$\mathbf{V_s}$	**Thrust**	**Shaft speed**	**Torque**	**Heave**	**Trim**	**Kiel probe**
-	m/s	knots	N	RPM	Nm	mm	degrees	V
0.24	1.56	14.1	10.0	1,784	0.2	-1.7	0.1	1.9
0.26	1.70	15.4	11.4	1,896	0.2	-2.1	0.1	2.0
0.28	1.83	16.5	13.1	2,027	0.2	-2.7	0.1	2.1
0.30	1.96	17.7	15.0	2,154	0.2	-3.5	0.1	2.3
0.32	2.08	18.8	16.9	2,260	0.3	-4.3	0.1	2.4
0.34	2.22	20.1	18.1	2,347	0.3	-5.0	0.1	2.5
0.36	2.35	21.3	19.5	2,436	0.3	-6.1	0.1	2.7
0.38	2.48	22.4	22.0	2,563	0.3	-7.1	0.2	2.8
0.40	2.62	23.6	25.7	2,731	0.4	-9.0	0.4	3.1

The Kiel probe measurement (in Volts) at the self-propulsion point for each speed was then used, together with Figure 4.28 from the flow rate measurement test results (see Section 4.5.4), to determine the mass flow. This varied from 2.4 to 4.1 Kg/s for the model port and starboard waterjet systems in the measured length Froude number range of 0.24 to 0.4, which corresponds to a full scale speed range of 14 to 24 knots.

A comparison of measurements from the waterjet self-propulsion test (see Figure 4.41) showing thrust at zero force ($T_{F=0}$), force at zero thrust ($F_{T=0}$), thrust at full scale self-propulsion point (T_{SPP}), towing force (F_D), and measurements from bare-hull resistance test is presented in Figure 4.44. A discussion about method of testing and extrapolation, presented in Bose (2008), mentions that the force at zero thrust ($F_{T=0}$) is expected to be somewhat greater than the bare-hull resistance.

Results of force at zero thrust ($F_{T=0}$) were found to be the same or less than the recorded bare-hull resistance. Differences between force at zero thrust ($F_{T=0}$) and recorded bare-hull resistance vary by about 9% at a length Froude number of 0.32 (ship speed 19 knots) and by about 13% at length Froude number of 0.38 (ship speed 22 knots) which is just above hump speed measured in resistance test. Eslamdoost (2014) reported model gross thrust values lower than bare-hull resistance values in the length Froude number range of 0.3 to 0.4 with a changeover, where the gross thrust becomes larger than bare-hull resistance, at a length Froude number of 0.43.

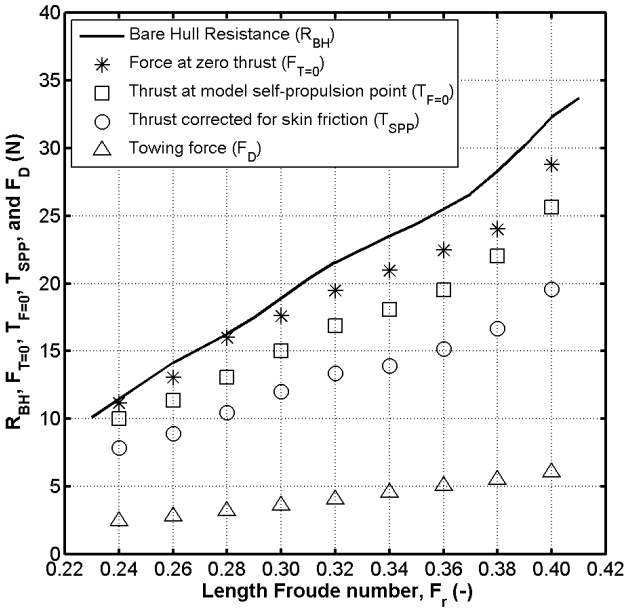

Figure 4.44: Comparison plot showing results recorded in self-propulsion test such as thrust at model self-propulsion point (thrust at zero force, $T_{F=0}$), force at zero thrust ($F_{T=0}$), thrust corrected for skin friction used for scaling to full scale thrust (T_{SPP}), towing force (F_D), and measurements from bare-hull resistance test. Bare-hull resistance was corrected for water temperature differences between resistance test and self-propulsion test, as well as shallow water effects using Schuster (1955) as discussed in Section 4.4.9.

Thrust calculated at the full scale self-propulsion point was then used for full scale extrapolation using Equation 4.41, shown in Section 4.6.6, and the resulting full scale thrust equates from 81 to 202 kN, for a single demihull, in the tested length Froude number range of 0.24 to 0.4.

4.6.5 Thrust and Thrust Deduction

Using the control volume defined in Section 2.2, and considering a fixed Cartesian coordinate system, the thrust force acting on the control volume can be determined by applying the momentum conversation low over the defined control volume (Figure 2.2). The sum of the forces acting on that control volume is equal to the change in momentum flux on that control volume as shown in Equation 4.29 and discussed by van Terwisga (1996) and Eslamdoost (2014). The left part of Equation 4.29 describes the net momentum flux through the control volume and the other three components consist of the external force acting on the surface of the control volume, the body force on the control volume, and the pump force acting on the fluid.

$$\iint_{A_1+A_8} \rho u_i \left(u_k n_k\right) dA = \iint_{A_1+A_2+A_6+A_8} \sigma_{ij} n_j dA + \iiint_{V_7} \rho F_{pi} dV + \iiint_{V} \rho F_i dV \quad (4.29)$$

Gross thrust (T_G) was defined by van Terwisga (1996) as "the force vector pertinent to the changes in momentum flux over the selected control volume, acting on its environment" and is basically the definition of the left hand side of Equation 4.29. Gross thrust is a force vector and the horizontal component (T_{Gx}) is called the gross thrust (T_G) as shown in Equation 4.30. As gross thrust is the reaction force applied by the control volume on its environment the negative sign changes the gross thrust to the same direction as the net thrust.

$$T_{Gx} = T_G = -\iint_{A_1+A_8} \rho u_i \left(u_k n_k\right) dA \quad (4.30)$$

Considering a uniform distribution for the intake and the jet velocity, Equation 4.30 can be simplified as shown in Equation 4.31, where T_{Gm} is model gross thrust, $\dot{m}$ is model mass flow rate, Q_{Jm} is model volumetric flow rate, A_{nm} is model nozzle area, V_{Jm} is model jet velocity, V_{Im} is model inlet velocity, and w_m is momentum wake fraction.

$$T_{Gm} = \dot{m}_m \left(V_{Jm} - V_{Im}\right) = \rho_m Q_{Jm} \left(V_{Jm} - V_{Im}\right) = \rho_m Q_{Jm} \left(\frac{Q_{Jm}}{A_{nm}} - (1 - w_m) V_m\right) \quad (4.31)$$

Obtaining the thrust deduction using waterjet self-propulsion test results only is discussed in detail in Section 4.4.8 and is based on procedures as published in Holtrop (2001), Bose (2008) and Øyan (2012) where thrust deduction is calculated using Equation 4.32, where force at zero thrust ($F_{T=0}$), towing force (F_M), and thrust at model self-propulsion point corrected

for skin friction (T_M). The definitions of $F_{T=0}$, F_M, and T_M are discussed in Section 4.6.4.

$$t = 1 - \frac{F_{T=0} - F_M}{T_M} \tag{4.32}$$

Using the results of the waterjet self-propulsion the resulting thrust deduction values were calculated as shown in Figure 4.45.

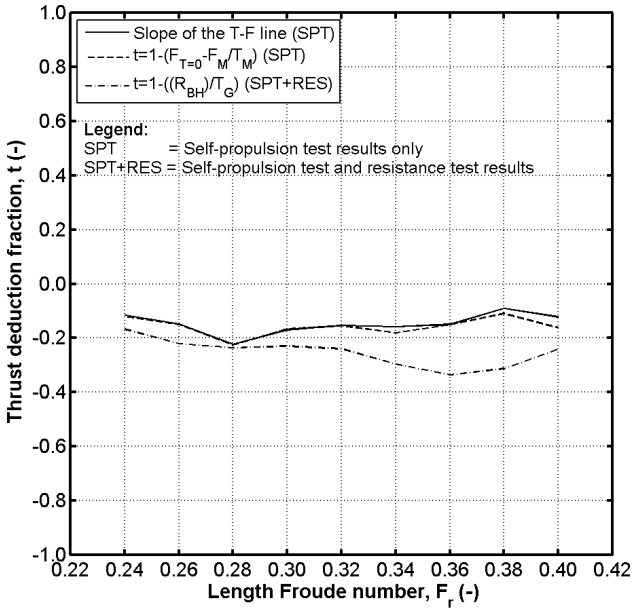

Figure 4.45: Comparison of thrust deduction results calculated using bare-hull resistance test results together with waterjet self-propulsion test results (SPT+RES) and thrust deduction calculated using only waterjet self-propulsion test results (SPT).

A comparison of thrust deduction fractions based on the slope of the T-F line (see Figure 4.41) and calculated by using Equation 4.32 showed that results varied by 4% to 24% increasing with speed. The general trend of the thrust deduction fractions based only on results of the self-propulsion test and results of the combined self-propulsion and bare-hull resistance test results showed a similar trend up to length Froude number of 0.32. At higher length Froude numbers than 0.32 thrust deduction fractions based only on results of the self-propulsion test were in the same range as those below length Froude number 0.32, but thrust deduction fractions based on combined self-propulsion and bare-hull resistance test results decreased to a maximum value of -0.32 at a length Froude number of 0.36. As shown in Figure 4.44, the measured bare-hull resistance was larger than the resistance of the self-propelled hull (i.e. force at zero thrust, $F_{T=0}$) for all tested speeds and this resulted in negative thrust deductions.

A force equilibrium called thrust-drag equilibrium exists between the hull and the propulsor. The delivered thrust from the propulsors should match the drag at each analysed speed, noting that this is delivered thrust and not theoretical waterjet thrust. Delivered thrust

takes the effect of the ship on the waterjet into account, as described by two hull-propulsor interaction coefficients known as thrust deduction and wake fraction.

Conventionally, the thrust deduction for a waterjet propelled hull is defined as the ratio between the bare-hull resistance and the gross thrust, where the gross thrust is the horizontal component of the momentum flux change in the waterjet system. For propeller propelled vessels the thrust deduction factor is defined as the ratio between the bare-hull resistance and the net thrust, where net thrust is the force transmitted through the propeller shaft. For a waterjet system, it is not only the impeller shaft transmitting the thrust force to the hull; a fraction of the thrust is also transferred to the hull through the waterjet ducting channel and for this reason the gross thrust, based on the momentum flux change, was measured instead.

Based on details given in Eslamdoost (2014), an investigation of negative thrust deduction is possible through analysis of the hull resistance increment and its intake drag where the main effective parameters on the resistance increment of a hull are trim, sinkage and local flow variations. When following ITTC recommended procedures, it was shown that only the intake induced pressure has a major effect on the trim angle and sinkage of the self-propelled ship. The pressure induced by the intake causes the hull to sink more which increases the hull resistance.

A change in transom submergence is the most important effect of the combined trim and sinkage change. There is a correlation between the hull transom submergence, its resistance and its effective waterline length. Increasing the submergence of the transom increases the hull resistance (due to lost hydrostatic pressure and a larger wetted hull area); while an increase in effective waterline length decreases the hull resistance. As a result of these effects there is an optimum transom area which increases with speed and is based on the ratio of the optimum transom area of the hull at rest to the maximum sectional area discussed in Larsson et al. (2010). When the combination of sinkage and trim changes cause the transom size to approach the optimum, the resistance will decrease. The means that if the hull is optimised for bare-hull conditions, it will not be optimum for the self-propulsion condition, the resistance will increase and this will contribute to a positive thrust deduction. If the hull is not optimised in bare hull conditions then, under the right circumstances, the optimum may be approached in the self-propulsion condition and there is a chance of a negative thrust deduction. Taking these restrictions into account it is best to optimise the hull for self-propulsion as discussed in Eslamdoost (2014).

Local flow changes also contribute to the hull resistance increment. Wave patterns are altered due to the change in the flow field in the area of the intake. This effect increases the hull resistance, since the waterjet suction lowers the wave trough in this region. In addition to the wave pattern change, ingestion of flow into the waterjet system increases the transom

wave and this will delay the length Froude number at which the transom clears (due to lost hydrostatic pressure). At the instant that the transom clears, the resistance increases considerably, and a large resistance may be obtained in the length Froude number range where the self-propelled hull transom is still wet but the bare hull resistance is cleared (i.e. no hydrostatic pressure is exerted on it).

Another effect which contributes to the thrust deduction fraction is the intake drag or thrust. As indicated by van Terwisga (1996), the intake drag is negligible except at the speed at which maximum trim occurs (i.e. hump speed).

4.6.6 Powering Prediction

The powering prediction method is based on the reasoning than an overall powering prediction can be broken down into predictions of the individual components in an undisturbed environment and the method is complemented with a correction for possible interaction effects. Overall performance of the hull/waterjet system can be expressed as a non-dimensional output, normally referred to as overall efficiency (η_{OA}) defined in ITTC (2011c) as shown in Equation 4.33, where η_0 is free-stream efficiency (Equation 4.34), and η_{INT} is the total interaction efficiency (Equation 4.35) accounting for a change in environment of the system.

$$\eta_{OA} = \eta_0 \eta_{INT} \tag{4.33}$$

Free stream efficiency (η_0) is determined by using Equation 4.34, where η_I is ideal efficiency, η_{Pump} is pump efficiency , and η_{Duct} is ducting efficiency.

$$\eta_0 = \eta_I \eta_{Pump} \eta_{Duct} \tag{4.34}$$

Interaction efficiency (η_{INT}) is determined from the results of waterjet self-propulsion test using Equation 4.35, where t is thrust deduction fraction, η_{eI} is energy interaction efficiency, and η_{mI} is momentum interaction efficiency.

$$\eta_{INT} = (1 - t)\,\frac{\eta_{eI}}{\eta_{mI}} \tag{4.35}$$

This approach is similar to the method used in propeller hydrodynamics where the free-stream efficiency is referred to as open water efficiency and the interaction efficiency is identified in the product of hull and relative rotative efficiency (η_R). A breakdown of the impeller delivered power into the power requirements and corresponding efficiencies of the components is schematised in Figure 4.46.

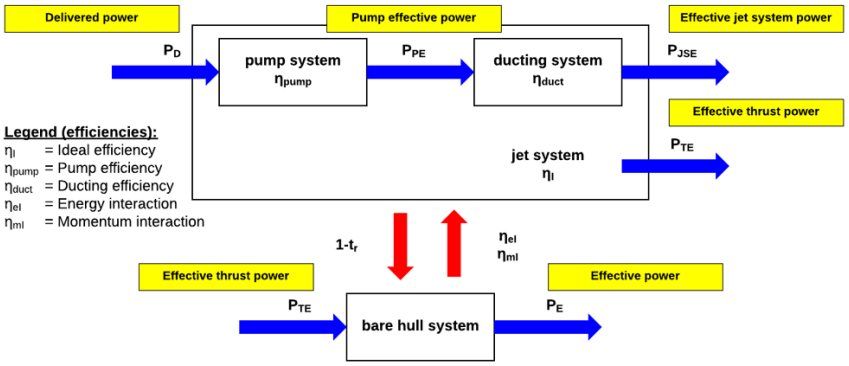

Figure 4.46: Power requirements introduced by waterjet-hull interaction.

When the overall propulsive efficiency (η_D) is known, the delivered power (P_D) delivered to the pump follows from the definition of the overall propulsive efficiency (η_D) shown in Equation 4.36, where P_E is effective power, P_D is delivered power and where it is assumed that the resistance-speed relation for the tested hull form is known.

$$\eta_D = \frac{P_E}{P_D} \tag{4.36}$$

A general definition of the effective power requirement (using bare-hull resistance results) that is delivered by the waterjet-hull system is then obtained from Equation 4.37, where R_{BH} is bare-hull resistance and V is ship speed. Bare-hull resistance was defined in accordance with ITTC High Speed Marine Vehicle Committee guideline 7.5-02-05-01, where resistance of the hull was measured whilst the additional weight of the waterjet system, including entrained water, was accounted for in the weight distribution.

$$P_E = R_{BH} V \tag{4.37}$$

Based on Ghadimi et al. (2013) the effective propulsion power (P_E) delivered by the system (using self-propulsion test results only) is given by Equation 4.38, where $F_{T=0}$ is force at zero thrust from self-propulsion test, and V is ship speed.

$$P_E = F_{T=0}\, V \tag{4.38}$$

To calculate full scale power, volumetric flow rate, size of intake area, and energy flux at momentum flux stations 1 and 7 are required. Due to scale effects of the boundary layer profile at the waterjet intake these quantities cannot be transferred directly from corresponding model scale values. However, the following procedure can be used indirectly to establish the required values. Full scale wake fraction is determined by scaling model wake fraction as discussed in Section 4.6.5, and the full scale thrust is determined by scaling the model scale thrust using Equation 4.38 as described by Bose (2008).

$$\frac{T_s}{T_m} = \frac{K_T\, \rho_s\, n_s^2\, D_s^4}{K_T\, \rho_m\, n_m^2\, D_m^4} = \frac{\rho_s}{\rho_m} \lambda^4 \frac{n_s^2}{n_m^2} = \frac{\rho_s}{\rho_m} \lambda^3 \tag{4.39}$$

Simplifying and rearranging to full scale thrust (T_s) results in Equation 4.40, where T_m is thrust at model self-propulsion point corrected for skin friction as discussed in Section 4.6.4, λ is the model to full scale ratio, ρ_s is sea water density, ρ_m is fresh water density, and the subscripts "s" and "m" on the variables denote the full scale and model scale values.

$$T_s = T_m \, \lambda^3 \, \frac{\rho_s}{\rho_m} \tag{4.40}$$

Full scale values of Q_J, E_1, E_7, M_1 and M_7 were computed using momentum theory and the delivered power (P_D) was then calculated using effective pump power (P_{PE}), pump efficiency (η_{Pump}), installation efficiency (η_{Inst}), energy flux at station 7 (E_1), energy flux at station 1 (E_1), nozzle efficiency (η_n), inlet efficiency (η_i), and outlet loss factor between station 5 and 7 (ζ_{57}) as discussed in Bose (2008) and shown in Equation 4.41. Assumptions are that the angle of the jet to the horizontal is 0°, rotation of the jet is zero, and that the height of the jet above the free surface (h_j) is 0.

$$\begin{aligned} P_D &= \frac{P_{PE}}{\eta_{Pump}\,\eta_{Inst}} = \frac{E_7\,(1+\varsigma_{57}) - \eta_i E_1}{\eta_{Pump}\,\eta_{Inst}} \\ &= \frac{\frac{E_7}{\eta_n} - \eta_i E_1}{\eta_{Pump}\,\eta_{Inst}} = \frac{\frac{1}{2}\rho Q_J \left\{ \frac{V_J^2}{\eta_n} - \eta_i V^2 \,(1-w)^2 \right\}}{\eta_{Pump}\,\eta_{Inst}} \end{aligned} \tag{4.41}$$

Effective pump power (P_{PE}) was calculated using Equation 4.42, where P_{JSE} is effective jet system power ($P_{JSE} = E_7 - E_1$), $H35$ is the increase of the mean total head across the waterjet pump shown in Equation 4.43), ζ_{13} are the internal losses for stations 1 to 3 (see Figure 2.1 in Section 2.1) calculated using Equation 4.44, ζ_{57} are internal losses for stations 5 to 7 calculated using Equation 4.45. Energy flux at any station (i) was calculated using Equation 4.46, where E_i is the local energy velocity at a particular location.

$$P_{PE} = P_{JSE} + \rho g Q_J H_{35} + \varsigma_{13} E_0 + \varsigma_{57} E_7 \tag{4.42}$$

$$H_{35} = \frac{1}{\rho g Q_J}[E_7\,(1+\varsigma_{57}) - E_1 + E_0 \varsigma_{13}] \tag{4.43}$$

$$\zeta_{13} = \frac{E_1 - E_3}{E_0} \tag{4.44}$$

$$\zeta_{57} = \frac{E_5 - E_7}{E_7} \tag{4.45}$$

$$E_i = \frac{1}{2}\,\rho \int_{QJ} V_{Ei}^2 \, d\, Q_J \tag{4.46}$$

Calculation of energy flux at station 3 (E_3) could be simplified if the velocity distribution just ahead of the pump is assumed to be uniform, but this is almost never the case as in reality the velocity is quite non-uniform with large velocity variations. The power associated with internal losses is given by:

$$P_{Internal\ Losses} = \varsigma_{13} E_0 + \varsigma_{57} E_7 \tag{4.47}$$

As there was no detailed investigation into installation efficiency (η_{Inst}), the value used here for all analysis purposes was 1. Full scale pump efficiency was determined using a set of waterjet unit benchmark data supplied by the manufacturer Wärtsilä, showing measured values of volumetric flow rate (Q_J), pump head (H_{35}), pump efficiency (η_{Pump}), flow coefficient (φ), and head coefficient (ψ) for a single full scale shaft speed of 568 RPM. This data was then extrapolated to the full scale shaft speeds established in the extrapolation of the model waterjet self-propulsion test and an example set of the extrapolated waterjet benchmark showing pump heads and pump efficiencies plotted against flow rate, is presented in Figure 4.47.

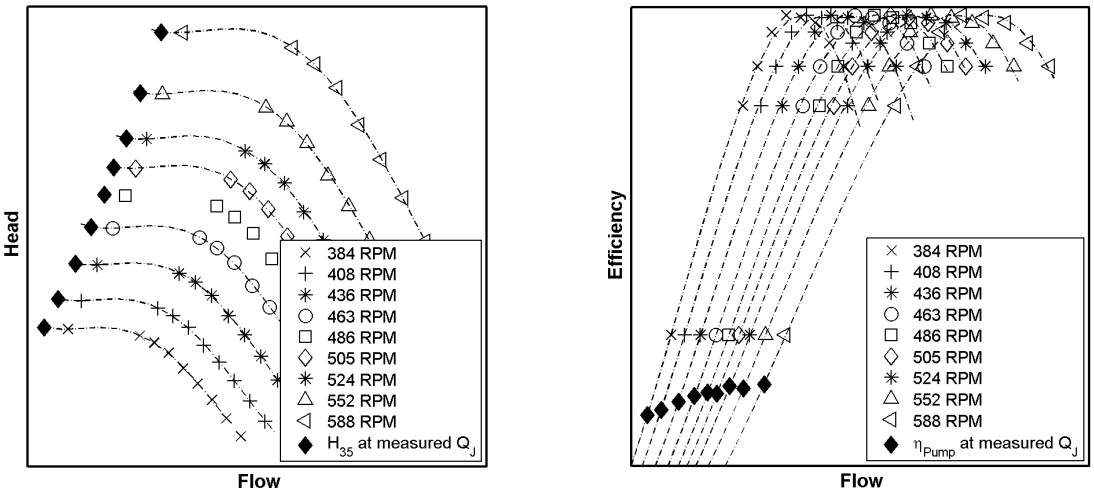

Figure 4.47: Scaled waterjet pump curve showing Wärtsilä supplied results for full scale pump head and pump efficiency plotted against flow rate. Pump heads and pump efficiencies determined using experimentally measured flow rates are indicated on pump head and pump efficiency curves.

The performance of the prototype waterjet system (waterjet unit benchmark data supplied by Wärtsilä) was then evaluated by assuming geometric and dynamic similitudes of the measured results in the presented experimental results. The scaled pressure head, volumetric flow rate were then obtained using Equation 4.48 and Equation 4.49, as discussed in Fujisawa (1995), where H is pump head, Q is volumetric flow rate, n is shaft speed, D is nozzle diameter, and where the quote denotes the a value transformed into the scaled condition.

$$\frac{H'}{H} = \left(\frac{n'}{n}\right)^2 \left(\frac{D'}{D}\right)^2 \tag{4.48}$$

$$\frac{Q'}{Q} = \left(\frac{n'}{n}\right)\left(\frac{D'}{D}\right)^3 \tag{4.49}$$

Using calculated full scale shaft speeds, scaled benchmark data, and full scale volumetric flow rates; pump efficiencies resulted in a range of 59-62% for the tested length Froude number range of 0.24 to 0.4 and a shaft speed range of 384-588 RPM. Pump efficiencies established using extrapolated results of the model waterjet self-propulsion test and full scale waterjet unit benchmark data resulted in pump efficiencies lower than stated in literature of about 70% for comparable waterjet pumps as discussed in Bulten (2006). Alternatively, delivered power can also be calculated as defined in ITTC Waterjet System Performance guidelines, presented in ITTC (2005b), using pump head (H_{35}) and volumetric flow rate shown in Equation 4.50, where ρ is fluid density, g is gravitational constant, Q_J is volumetric flow rate, and H_{35} is pump head between momentum flux station 3 and 5.

$$P_D = \frac{P_{PE}}{\eta_{Pump}\,\eta_{Inst}} = \frac{\rho\, g\, Q_J\, H_{35}}{\eta_{Pump}\,\eta_{Inst}} \tag{4.50}$$

Calculated results of delivered power for each measured speed are discussed, together with other results, in Section 4.6.10 as well as in Chapter 5, where the calculated delivered power is compared with sea trials performance data.

4.6.7 Overall propulsive efficiency

Overall propulsive efficiency (η_D), also called quasi-propulsive coefficient, of the waterjet propulsion system is of prime importance as it is a measure of useful work (i.e. effective power, P_E) compared to the total work (i.e. delivered power, P_D). A general definition of overall propulsive efficiency is defined in Equation 4.51, where P_E is effective power and P_D is delivered power.

$$\eta_D = \frac{useful\ work}{total\ work} = \frac{P_E}{P_D} \tag{4.51}$$

Effective power (P_E) can either be calculated using the measured bare-hull resistance (R_{BH}) and ship speed (V) as shown in Equation 4.52 or by using the force at zero thrust ($F_{T=0}$) measured in the self-propulsion test (see Section 4.6.4) together with ship speed (V) as shown in Equation 4.53.

$$P_E = R_{BH}V \tag{4.52}$$

$$P_E = F_{T=0}V \tag{4.53}$$

Another method is to use a more detailed numerical determination of overall propulsive efficiency presented in Bose (2008) and shown in Equation 4.54, where ΔM is the change in

momentum flux, V is ship speed, and P_{PE} is effective pump power. Change in momentum flux is defined as $\Delta M = M_7 cos(\alpha) - M_1$, where α is the angle between the shaft line of the jet and the horizontal plane, and M_1 and M_7 are axial components of the momentum, due to the axial components of the velocities at momentum flux stations 1 and 7.

$$\eta_D = \frac{P_E}{P_D} = \frac{\Delta\ MV}{P_{PE}}\ \eta_P\ \eta_{inst} = \frac{2\left(\frac{V_J}{V}cos\alpha - (1-w)\right)\eta_{Pump}\ \eta_{Inst}}{\left(\frac{V_j^2}{V^2\eta_n} - \eta_i(1-w)^2\right) + \left(\frac{2\,h_j\,g}{V^2}\right)} \tag{4.54}$$

Calculation of delivered power (P_D) is discussed in Section 4.6.6 and the calculation of overall propulsive efficiency, using the discussed methods, resulted in overall propulsive efficiencies presented in Figure 4.48.

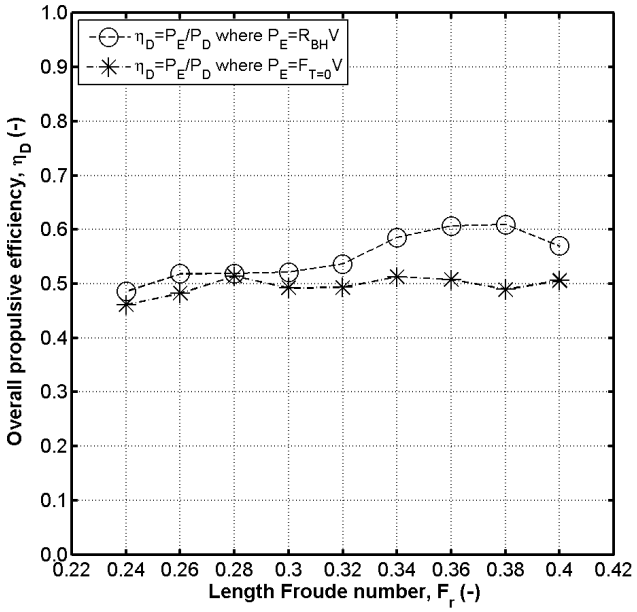

Figure 4.48: Overall propulsive efficiencies calculated using $\eta_D = P_E/P_D$, where effective power (P_E) is either calculated as $P_E = R_{BH}V$ using bare-hull resistance (R_{BH}) from resistance test and ship speed or calculated as $P_E = F_{T=0}V$ using force at zero thrust ($F_{T=0}$) from waterjet propulsion test and ship speed.

As shown in Figure 4.48, overall propulsive efficiency (η_D) varied from 46 to 51% when effective power was calculated using the force at zero thrust ($F_{T=0}$) results from waterjet self-propulsion test and from 48 to 60% when effective power was calculated using bare-hull resistance (R_{BH}) results. The differences in overall propulsive efficiency were based on the differences in measured bare-hull resistance and force at zero thrust from waterjet propulsion test discussed in Section 4.6.4.

4.6.8 Heave and Running Trim Comparison

Results for heave and running trim measured in the resistance test were discussed in detail in Section 4.4.9, but the same measurements were included in the waterjet self-propulsion testing to allow the comparison of heave and running trim behaviour of the model catamaran in the resistance and propelled conditions. Heave and running trim results for the waterjet propelled condition were determined at the self-propulsion point of each tested speed and the comparison of heave and trim results is shown in Figure 4.49.

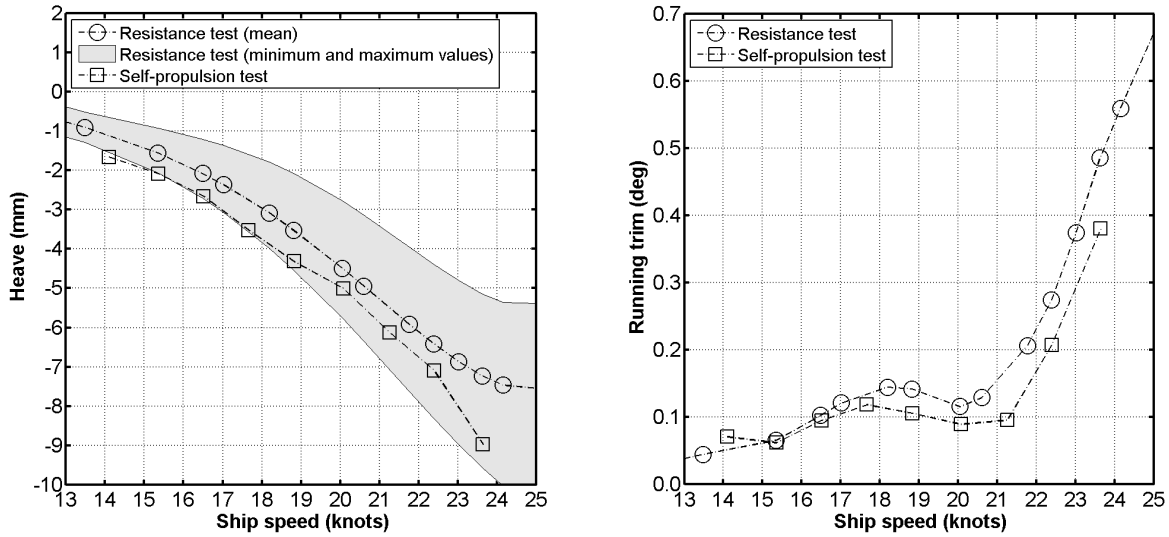

Figure 4.49: Comparison of heave and running trim using results from resistance test and waterjet self-propulsion test. Test results are shown for a single condition only which is light displacement, 1,500 tonnes, and level static trim, the condition tested in the self-propulsion test. The grey area in the heave plot shows the area of highest and lowest measured heave values based on averaged repeated measurements of the vertical travel on the forward and aft towing tank carriage posts where downward movement of carriage posts results in negative heave.

Comparing heave and running trim results shows that heave in the propelled condition is slightly lower than heave in the resistance condition and that reflects also on running trim as the running trim for propelled condition is lower than in the resistance condition. As both heave and trim are slightly different for the resistance and the propelled case that would mean that there is a small change in resistance as well which would come into play when using the combined resistance and self-propulsion results in calculations such as thrust deduction. The small differences in heave, running trim and resistance would suggest that when using combined test results of resistance and self-propulsion tests, the initial conditions of the two vessels are different. Whereas normally it is assumed to be the same when extrapolating test results for performance estimations. As the differences are small, it is proposed that the combined tests can still be used as good engineering approximations.

4.6.9 Data Reduction and Extrapolation

As described in Section 4.6.4, the thrust at the full scale self-propulsion point (T_m) was used to extrapolate to full scale thrust (T_s) using Equation 4.40. Scaling the calculated model momentum wake fraction (w_m) to full scale wake fraction (w_s), the full scale inlet velocity was calculated using $V_{Is} = (1 - w_s)\, V_s$ where full scale speed was extrapolated from model speed using Froude scaling such that $V_s = V_m\sqrt{\lambda}$ where λ was the model scale to full scale ratio. Full scale volumetric flow rate (Q_{Js}) was determined using the definition of full scale gross thrust shown in Equation 4.55, where A_{ns} is the full scale nozzle area, w_s is full scale wake fraction, V_s is ship speed, and solving equation for volumetric flow rate.

$$T_{Gs} = \dot{m}_s\,(V_{Js} - V_{Is}) = \rho_s Q_{Js}\,(V_{Js} - V_{Is}) = \rho_s Q_{Js}\left(\frac{Q_{Js}}{A_{ns}} - (1 - w_s)V_s\right) \tag{4.55}$$

Full scale volumetric flow rate (Q_{Js}) was then converted to full scale mass flow rate ($\dot{m}$) by using sea water density together with volumetric flow rate such that $\dot{m}_s = \rho_s Q_{Js}$, where $\dot{m}_s$ is full scale mass flow rate and ρ_s is sea water density.

Effective pump power (P_{PE}) was calculated using the method discussed in Section 4.6.6, with energy flux at stations 1 and 7 and the calculated full scale flow rate. Delivered power (P_D) was determined using $P_D = \frac{P_{PE}}{\eta_{Pump}\,\eta_{Inst}}$ where installation efficiency (η_{Inst}) in the absence of more detailed data was assumed to be 1 and the pump efficiency was taken from waterjet benchmark results supplied by the manufacturer Wärtsilä. As delivered power (P_D) was calculated directly behind the pump system (see Figure 4.46) a typical bearing loss of 2% was taken into account for the bearing located on the shaft at the entry into the inlet duct.

To calculate overall propulsive efficiency (η_D) the general definition of $\eta_D = \frac{P_E}{P_D}$ was used where effective power (P_E) was either calculated as $P_E = R_{BH}V$ using bare-hull resistance results or $P_E = F_{T=0}V$ when just self-propulsion test results were used as discussed in Section 4.6.7.

4.6.10 Test Results

In this section the results of the waterjet performance analysis are presented and discussed. The waterjet self-propulsion and flow rate measurement tests served several purposes; to develop experience at the AMC in testing methods for waterjet propelled vessels, to compare relevant data with bare-hull resistance tests in order to evaluate the testing method, to evaluate the use of the of the momentum flux method as outlined by ITTC, and to assess propulsive performance of a waterjet propelled catamaran. Performance test results can be broken down into results for power, flow rate, velocities, and the calculation of model scale and thrust coefficients (K_T) to ensure thrust identity.

There are several different waterjet power related values (see Figure 4.46) that can be calculated such as delivered power (P_D), effective pump power (P_{PE}), effective jet system power (P_{JSE}), effective power (P_E), gross thrust (T_G), and overall propulsive efficiency (η_D). Power results were calculated using the measurements of the waterjet self-propulsion tests and a comparison of results, for a single waterjet propulsion unit, with overall propulsive efficiency, calculated with either using measured bare-hull resistance (R_{BH}) or force at zero thrust ($F_{T=0}$), is shown in Figure 4.50. Effective pump power (P_{PE}), effective jet system power (P_{JSE}), delivered power (P_D), and effective thrust power (P_{TE}) show a small decrease in power in the hump speed region.

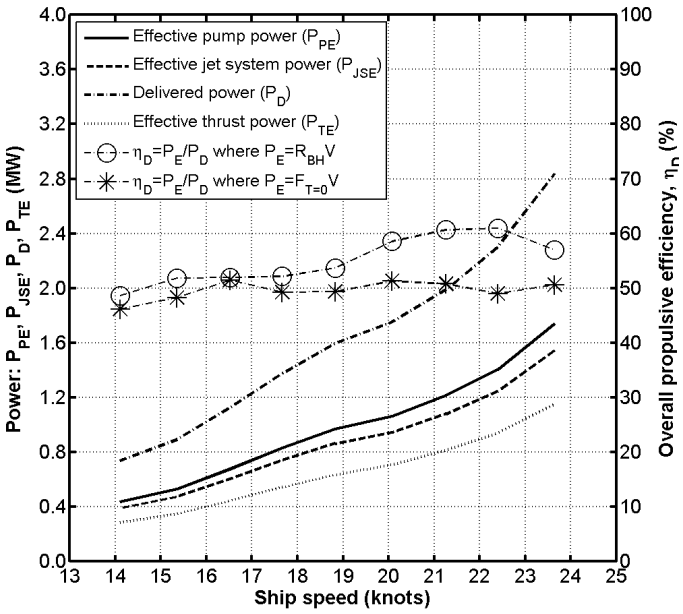

Figure 4.50: Comparison of a single waterjet propulsion unit showing effective pump power (P_{PE}), effective jet system power (P_{JSE}), delivered power (P_D), effective thrust power (P_{TE}) with overall propulsive efficiency (η_D).

Comparing calculated delivered power (P_D) to the residual resistance coefficient (C_{Rs}) from the bare-hull resistance test, shown in Figure 4.51, shows a slight reduction in delivered power at a length Froude number of 0.32 but there is no dramatic change in power at the hump speed, which is at a length Froude number of 0.37 as discussed in Section 4.4.9.

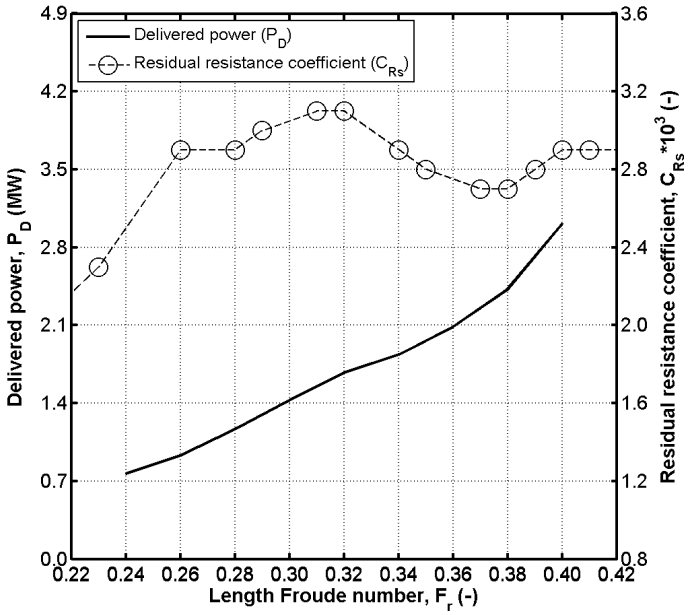

Figure 4.51: Full scale residual resistance coefficient (C_{Rs}) from bare-hull resistance test, and calculated delivered power (P_D) for a single waterjet propulsion system.

A comparison of overall propulsive efficiency (η_D) with residual resistance coefficient (C_{Rs}), shown in Figure 4.52, shows an increase of efficiency at hump speed which is in correlation with the slightly lower delivered power at that speed shown in Figure 4.51. There is an increase of overall propulsive efficiency (for $\eta_D = \frac{P_E}{P_D}$ where $P_E = R_{BH}V$) of about 7% in the length Froude number range between 0.32 and 0.38, which is due to the decrease in resistance at hump speed (see Section 4.4.9).

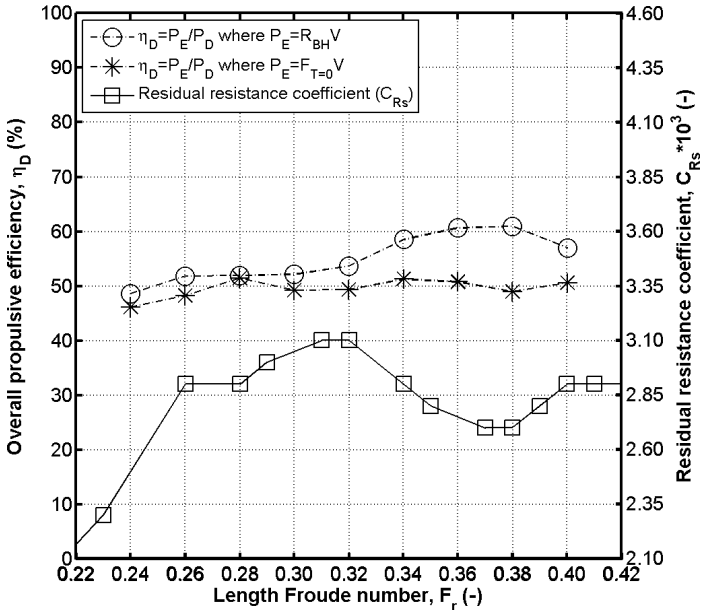

Figure 4.52: Full scale comparison of overall propulsive efficiency (η_D), where effective power (P_E) is either calculated using $P_E = R_{BH}V$ or $P_E = F_{T=0}V$, with residual resistance coefficient (C_{Rs}) showing an increase of efficiency in the hump speed region.

As the model waterjets are only used as a means to provide the thrust at the model self-propulsion point and not to model the actual waterjet itself, the most important results from the waterjet propulsion test are the flow rates and the combined thrust of both model waterjets. As discussed in Section 4.6, the thrust at the model self-propulsion points was corrected by using a towing force (F_D) to account for the excessive frictional resistance. A comparison of the measured model scale bare-hull resistance with force at zero thrust ($F_{T=0}$), thrust at model self-propulsion point ($T_{F=0}$), and thrust corrected using towing force (T_{SPP}) is shown in Figure 4.53 in relation to ship speed. As shown in Section 4.6.4, the results of the bare-hull resistance and the force at zero thrust ($F_{T=0}$) vary by about 9% at a ship speed of 19 knots and by about 13% at a ship speed of 22 knots.

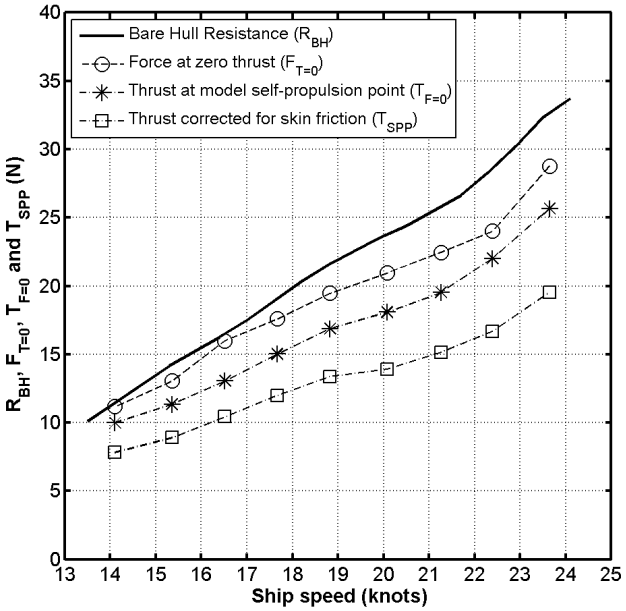

Figure 4.53: Comparison plot showing results recorded in self-propulsion test such as thrust at model self-propulsion point (thrust at zero force, $T_{F=0}$), force at zero thrust ($F_{T=0}$), and thrust corrected for skin friction used for scaling to full scale thrust (T_{SPP}). Bare-hull resistance (R_{BH}) was corrected for water temperature differences between resistance test and self-propulsion test, as well as shallow water effects using Schuster (1955) as discussed in Section 4.4.9.

A more detailed, logical breakdown of the thrust based waterjet performance extrapolation is given in Chapter 6 and a comparison of the calculated delivered power against power measured in full scale sea trials is given in Chapter 5.

4.6.11 Uncertainty Analysis Results

An ITTC based self-propulsion uncertainty analysis, using the results of the waterjet self-propulsion test measurements, was carried out using the methodology discussed in a general form in Appendix D. Bias and error components taken into account for the waterjet self-propulsion uncertainty analysis are outlined in Section D.3 of Appendix D. Based on the ITTC recommended waterjet uncertainty analysis total jet thrust uncertainties (U_{TJx}) were calculated for a length Froude number range of 0.24 to 0.4, ship speed 14 to 24 knots, based on the results of the waterjet self-propulsion test. A non-dimensional form of jet thrust (K_{TJx}) was used to carry out the jet thrust uncertainty analysis based on the flow rate data reduction equation (Equation D.24) shown in Appendix D and the resulting total jet thrust uncertainties are given in Figure 4.54.

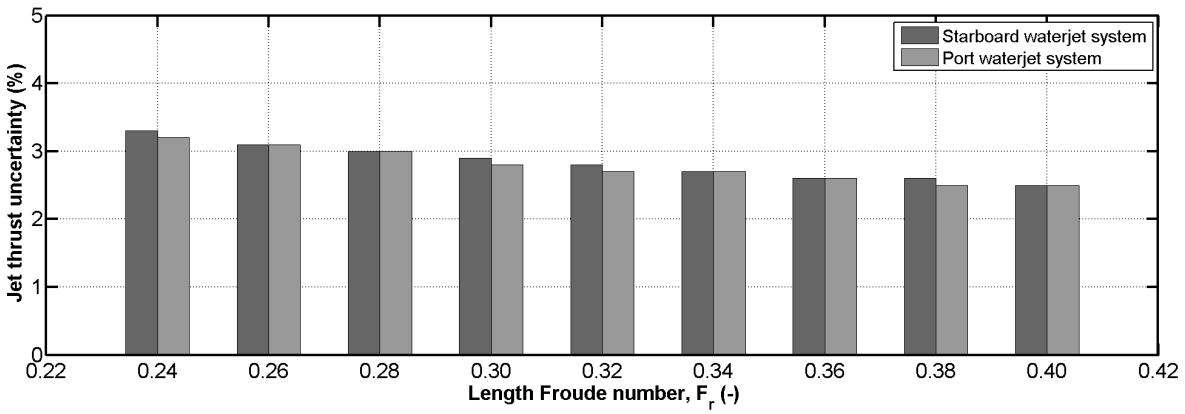

Figure 4.54: Thrust uncertainty results for waterjet self-propulsion test for a length Froude number range of 0.24 to 0.4, ship speed 14 to 24 knots.

The total jet thrust uncertainties are based on the uncertainty equation shown on in Equation 4.56 where the variable U_{TJx} is total uncertainty in in relation to jet thrust T_{Jx}, B_i are bias or systematic errors, and P_i are precision or random errors.

$$U_{K_{T_{Jx}}} = \sqrt{\left(B_{K_{T_{Jx}}}\right)^2 + \left(P_{K_{T_{Jx}}}\right)^2} \tag{4.56}$$

Bias errors are calculated using Equation 4.57 where subscripts are for volumetric flow rate (Q_J), nozzle diameter (D), shaft speed per second (n), pump centre inclination to horizontal (α), water density (ρ), and water temperature (t_w).

$$B_{K_{T_{Jx}}} = \sqrt{(\theta_{Q_J} B_{Q_J})^2 + (\theta_D B_D)^2 + (\theta_n B_n)^2 + (\theta_\alpha B_\alpha)^2 + (\theta_\rho (B_\rho + \theta_{\rho tw} B_{tw}))} \tag{4.57}$$

Breakdown of bias error components required for total jet thrust uncertainty:

- θ_{QJ}, θ_D, θ_n, θ_α, θ_ρ, and $\theta_{\rho tw}$ are volumetric flow rate (Q_J), nozzle diameter (D), shaft

speed per second (n), pump centre inclination to horizontal (α), and water density (ρ), and water temperature (t_W) sensitivity coefficients.

- B_{QJ} is volumetric flow rate bias based on standard deviation of flow rate measured in flow rate measurement test.
- B_D is nozzle diameter bias.
- B_n is shaft speed bias.
- B_α is pump centre inclination to horizontal bias.
- B_ρ is water density bias.
- B_{tw} is water temperature bias.

Based on the jet thrust uncertainty analysis the components adding the largest uncertainty to the result are flow rate (41%), nozzle diameter (9%), and water temperature (16%) as shown in Figure 4.55 for port and starboard waterjet propulsion system at a length Froude number of 0.24.

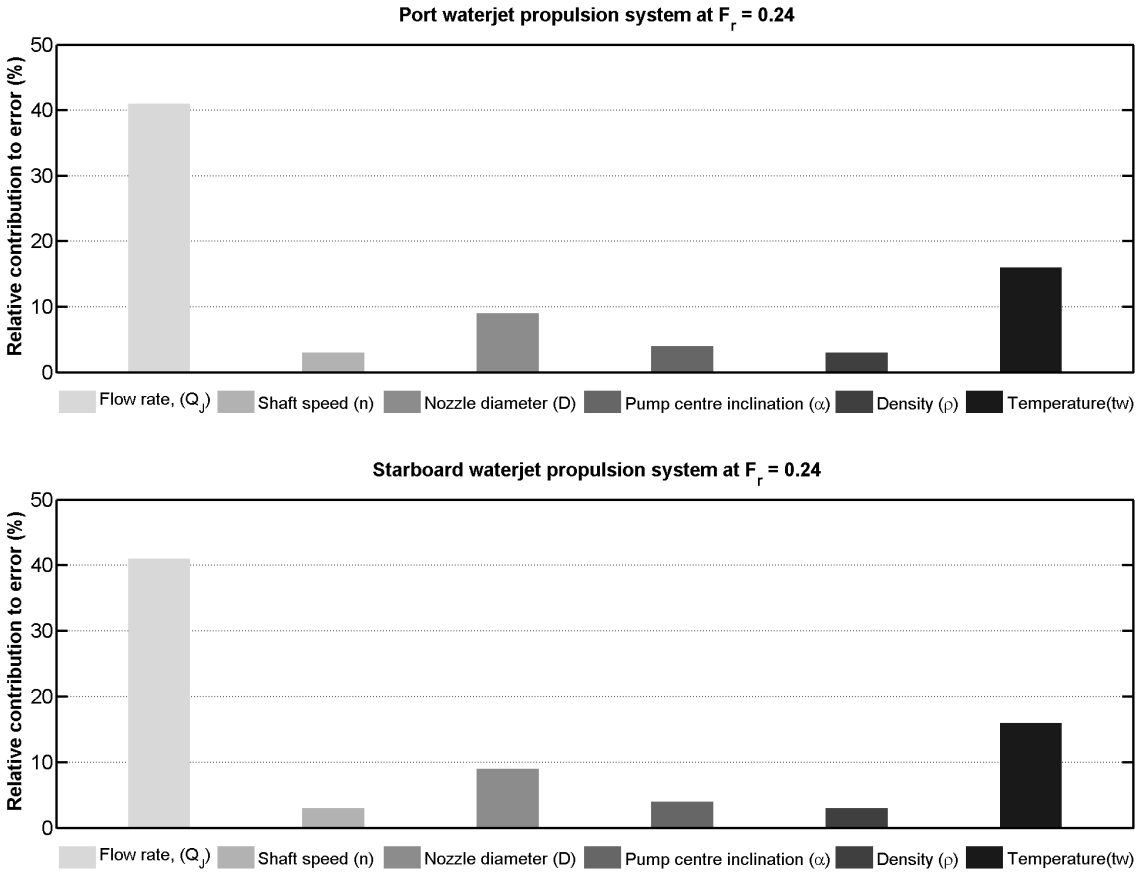

Figure 4.55: Relative importance of error in jet thrust sources for port waterjet propulsion system.

A tabulated summary of all total jet thrust uncertainties, bias errors, precision errors, relative contribution of parameter to error in percent, and a length Froude number range of 0.24 to 0.4 is given in Table 4.12.

Table 4.12: Relative Contributions To Error, Bias Errors, Precision Errors And Total Jet Thrust Uncertainties For Port And Starboard Waterjet Propulsion Systems And A Length Froude Number Range Of 0.24 to 0.4.

Speed	**Relative contribution to error**						**Total uncertainty**			
$\mathbf{F_r}$	$\mathbf{Q_J}$	**n**	**D**	$\boldsymbol{\alpha}$	$\boldsymbol{\rho}$	$\mathbf{t_w}$	$\mathbf{B_{TJx}}$	$\mathbf{P_{TJx}}$	$\mathbf{U_{TJx}}$	**% to** $\mathbf{T_{Jx}}$
-	%	%	%	%	%	%	-	-	-	%
Port waterjet propulsion system										
0.24	41	3	9	4	3	16	0.2119	0	0.2119	3.200
0.26	40	3	10	5	3	17	0.2074	0	0.2074	3.100
0.28	38	3	10	4	3	17	0.2015	0.0446	0.2064	3.000
0.30	38	3	11	3	4	19	0.1950	0	0.1950	2.800
0.32	37	3	11	3	4	19	0.1895	0	0.1895	2.700
0.34	36	3	11	4	4	20	0.1873	0.0265	0.1892	2.700
0.36	35	3	11	4	4	20	0.1845	0.025	0.1862	2.600
0.38	35	3	12	2	4	21	0.1809	0	0.1809	2.500
0.40	33	5	12	1	4	21	0.1781	0.0215	0.1794	2.500
Starboard waterjet propulsion system										
0.24	41	3	9	4	3	16	0.2055	0	0.2055	3.3
0.26	40	3	10	5	3	17	0.2015	0	0.2015	3.1
0.28	39	3	10	4	3	17	0.1943	0.0274	0.1962	3.0
0.30	38	3	11	3	4	18	0.1873	0	0.1873	2.9
0.32	37	3	11	3	4	19	0.1832	0.0282	0.1854	2.8
0.34	37	3	11	4	4	20	0.1812	0	0.1812	2.7
0.36	36	3	11	4	4	20	0.1788	0.0248	0.1805	2.6
0.38	35	3	12	2	4	20	0.1755	0.0231	0.1770	2.6
0.40	34	5	12	1	4	21	0.1728	0	0.1728	2.5

Chapter 5

Performance Validation and Comparison to Propeller Propulsion

Powering sea trials presented in Griggs et al. (2005) for a 98 m wave-piercing Incat catamaran (HSV-2) were carried out by the US Navy in the Gulf of Mexico off the coast of Ingleside (Texas, USA) from 15 to 19 November 2004. Recorded data included three displacements in shallow water (10.7 to 15.2 m), three displacements in deep water (>914 m), a speed range of 10 to 40 knots, and sea trial runs carried out using two or four running waterjets at the same time. As conditions on the day of the sea trials were for a certain water depth, wind, and waves, measured power results had to be corrected (Figure 5.1) to for these conditions so that the resulting power could be compared to the experimental test conditions which had no wind, no ambient waves and a correction for water depth.

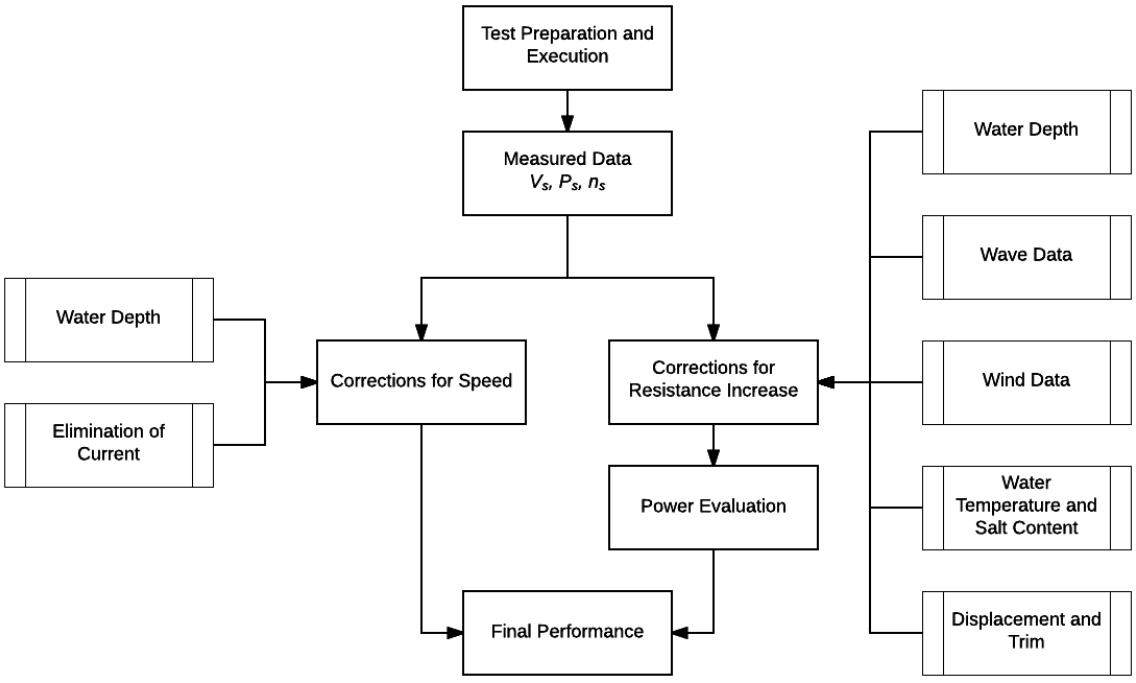

Figure 5.1: Flowchart of speed/power sea trials analysis.

The following three sections discuss the corrections applied to the sea trials data for the comparison with the measured experimental model test data, the comparison of the corrected power with power results established with model testing and discussed in Chapter 4, and a comparison of waterjet and propeller performance results.

5.1 Correction of Sea Trials Data for Waves, Wind and Water Depth

Correction of sea trials data is described in ITTC guideline 7.5-04-01-01.2 and describes corrections for waves, wind, water temperature, and water depth. Powering sea trial conditions, as described in the powering sea trials report, are listed in Table 5.1. Shallow water in the powering sea trials data was 35-50 feet (in metric units 10.7 to 15.2 m), and deep water >3,000 feet (in metric units >914 m). Scaling water depth from experimental testing to full scale, using a measured water depth of 1.5 m and Froude scaling with a model to full scale ratio of 21.6, equates to 1.5 x 21.6 = 32.4 m.

Table 5.1: Trial Conditions Described In Power Sea Trials Report For 98 m Wave-Piercing Incat Catamaran (HSV-2), Carried Out By The US Navy In The Gulf Of Mexico Off The Coast Of Ingleside, Texas, From 15 to 19 November 2004.

Δ	**Water depth**	**Wave height**	**Wave period**	**Wind speed**	**True wind direction**
(long tons)	(ft)	(ft)	(s)	(knots)	(degrees)
1,501	35-50	3-4	8	25.4	82
1,459	35-50	2-3	9	16.4	125
1,804	35-50	2-3	8	7.5	244
1,476	>3,000	5	9	22	90
1,776	>3,000	3-5	5	12.3	61
1,744	>3,000	3-5	7	8.5	94

Investigations for shallow water corrections for the sea trial results were based on calculations of depth to draft ratio and a comparison to generally accepted depth to draft ratios for shallow and deep water. The total beam of the full scale 98 m catamaran was 26.4 m, water depth varied from 10.7 to 15.2 m for shallow water and >914 m for deep water, experimentally tested speed range was 14 to 24 knots which equated to 7.3 to 12.2 m/s in full scale, and draft extrapolated from model scale to full scale was 2.9 m for a displacement of 1,500 tonnes. Calculated depth to draft ratio for a displacement of 1,500 tonnes in shallow water was 5.3 and for deep water 318.3. A ship's behaviour depends on the depth of the navigation area and a general distinction between shallow and deep water based on depth to draft ratio is given by Vantorre (2003) as shown in Table 5.2, where h is water depth and T is draft.

Table 5.2: Definition Of Shallow And Deep Water Based On Depth To Draft Ratio As Given By Vantorre (2003).

Water depth	**Depth to draft ratio (h/T)**
Deep water	h/T > 3
Medium deep water	1.5 < h/T < 3
Shallow water	1.2 < h/T < 1.5
Very shallow water	h/T < 1.2

Based on this definition, and using the calculated depth to draft ratio of 5.3 (shallow water) and 318.3 (deep water) both tests were carried out in what is considered deep water and therefore do not require shallow water corrections. Using a comparison of beam, draft and speed to water depth as defined by Bose (2008) and further investigated by Haakenstad (2012) effects of shallow water is negligible for the following water depths as shown in Equation 5.1 and Equation 5.2 (whichever is the largest), where B is beam, T is draught, and U is the speed of the vessel.

$$h > 3\,(B\,T)^{0.5} \tag{5.1}$$

$$h > \frac{2.75\,U^2}{g} \tag{5.2}$$

Using Equation 5.1, Equation 5.2, and the sea trials speed range of 9 to 38 knots (4.6 to 19.7 m/s) results in a value of 26.1 using $3\,(B\,T)^{0.5}$. Comparing this to an averaged shallow water depth of 13 m (averaged using 35 feet = 10.7 m and 50 feet = 15.2 m) it can be stated that for the shallow water condition tested in sea trials, shallow water effects would have to be considered. Using the same considerations for the deep water condition, calculation of $3\,(B\,T)^{0.5}$ and $\frac{2.75\,U^2}{g}$ yield values lower than the water depth of >914 m for all tested speeds and therefore no shallow water effects would have to be considered. Applying the same method to the experimental condition in model scale, using a water depth of 1.5 m, results in shallow water effects above a speed range of about 2.3 m/s (full scale 21 knots) which is in the resistance hump speed region. Considering the experimental condition (deep water) and the available sea trial conditions (shallow and deep water) the condition accurately representing the experimental condition is the sea trials deep water condition.

Using Table 5.1, the two displacements in the 1,500 tonnes range are either shallow water with a displacement of 1,501 long tons (1,525 metric tonnes), or deep water with a displacement of 1,476 long tons (1,500 metric tonnes) and power correction analysis was carried out using both displacements as the water depth tested in model scale (i.e. 32.4 m) was not considered to be shallow water but could also not be considered deep water. A comparison of uncorrected total shaft power for four waterjet propulsion systems, two for each demihull, using shallow water and deep water measurements is shown in Figure 5.2, where shallow water measurements

show a significant change in power requirements in the speed range of 19 to 29 knots while power requirements for deep water just show a steady increase of required power.

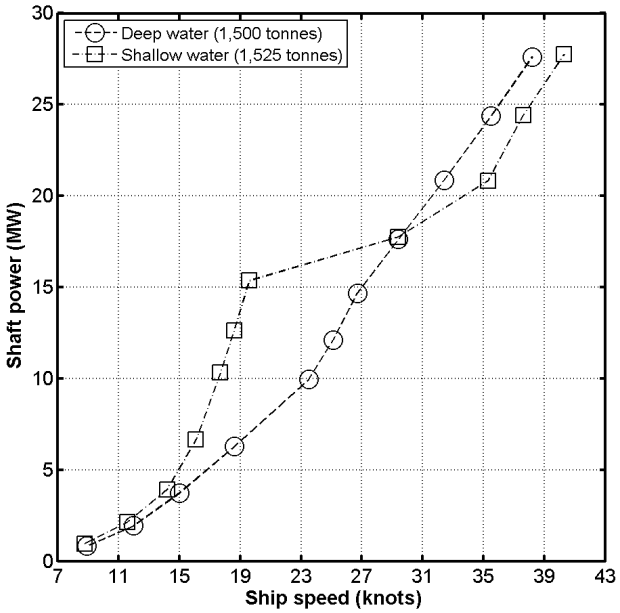

Figure 5.2: Comparison of uncorrected full scale total shaft power for a displacement of about 1,500 metric tonnes in shallow and deep water for a speed range of 10-40 knots. Data for the comparison of the full scale shaft power was taken from the powering sea trials report provided by Griggs et al. (2005).

Using the direct power method, discussed in ITTC guideline 7.5-04-01-01.2, measured power is directly corrected with the power increase due to added resistance in the trial conditions, as shown in Equation 5.3, where P_{SC} is corrected power, P_{SM} measured power, and ΔP is required correction for power calculated using Equation 5.4, where ΔP is resistance increase, V_s is ship speed, η_S is shaft efficiency (using a typical 2% for shaft losses), and η_D is overall propulsive efficiency.

$$P_{SC} = R_{SM} + \Delta P \tag{5.3}$$

$$\Delta P = \frac{\Delta R V_S}{\eta_S \eta_D} \tag{5.4}$$

As the available data does not include overall propulsive efficiencies for the full range of speeds measured in the sea trial runs (10 to 38 knots) values based on a curve fit was used. Resistance increase (ΔR) is then calculated using Equation 5.5, where R_{AA} is the resistance increase due to relative wind, R_{AS} is resistance increase due to deviation of water temperature and water density, and R_{AW} is resistance increase due to waves.

$$\Delta R = R_{AA} + R_{AS} + R_{AW} \tag{5.5}$$

The resistance increase due to relative wind (R_{AA}) was calculated using Equation 5.6, where

A_{XV} is area of maximum transverse section exposed to the wind, C_{AA} is wind resistance coefficient, V_{WR} is relative wind speed, ρ_A is air density (1.204 Kg/m^3), and $\psi_W R$ is relative wind direction (0 degrees means heading wind).

$$R_{AA} = \frac{1}{2}\rho_A V_{WR}^2 C_{AA}\left(\psi_{WR}\right) A_{XV} \tag{5.6}$$

Wind resistance coefficient (C_{AA}) was calculated using Equation 5.7, where C_{DA} is the air drag coefficient ($C_{DA} = 0.446$ as described in Section 4.4.8), A_{VS} is projected area of the ship above the water line to the transverse plane (1,147 m^2), S_S is wetted surface area (1,409 m^2), and ρ_A is air density (1.204 Kg/m^3). The calculated value for wind resistance coefficient (C_{AA}), using the stated values, results in $C_{AA} = 0.0004$.

$$C_{AA} = C_{DA}\frac{\rho_A A_{VS}}{\rho_S S_S} \tag{5.7}$$

The resistance increase due to deviation of water temperature and water density (R_{AS}) was calculated using Equation 5.8, where C_F is frictional resistance coefficient (actual water temperature), C_{F0} is frictional resistance coefficient (reference water temperature), C_{T0} is total resistance coefficient (reference water temperature), R_{AS} is resistance increase due to deviation of water temperature and water density, R_F is frictional resistance (actual water temperature), R_{F0} is frictional resistance (reference water temperature), R_{T0} is total resistance (reference water temperature), S is wetted surface area, V_s is ship speed, ρ is Water density (actual water temperature), and ρ_0 is water density (reference water temperature).

$$\begin{aligned} R_{AS} &= R_{T0}\left(1 - \frac{\rho}{\rho_0}\right) - R_F\left(1 - \frac{C_{F0}}{C_F}\right) \\ R_F &= \frac{1}{2}\rho S V_S^2 C_F \\ R_{F0} &= \frac{1}{2}\rho S V_S^2 C_{F0} \\ R_{T0} &= \frac{1}{2}\rho_0 S V_S^2 C_{T0} \end{aligned} \tag{5.8}$$

The resistance increase due to waves (R_{AW}) can be calculated using Equation 5.9, but as there was insufficient information on sea state at the time of the sea trials a simplified correction method was used. The simplified correction method is given in ITTC Analysis of Speed/Power Trial Data (Procedure 7.5-04-01-01.2) as shown in Equation 5.10, where B is beam of the ship (26.4 m), $H_{W1/3}$ is significant wave height (4 or 5 feet, depending on whether shallow water or deep water condition is used as shown in Table 5.1), and L_{BWL} is distance of the bow to 95% of maximum breadth on the waterline (43.2 m).

$$R_{AW} = 2\int_0^{2\Pi}\int_0^{\infty} \frac{R_{wave}\left(\omega\ \alpha\ V_S\right)}{\zeta_A^2} E\left(\omega\ \alpha\right) d\omega d\alpha \tag{5.9}$$

$$R_{AWL} = \frac{1}{16}\rho\, g\, H_{W1/3}^2 \sqrt{\frac{B}{L_{BWL}}} \tag{5.10}$$

Corrections of the ship performance due to the effects of shallow water for selected speeds can be determined using Equation 5.10, where A_M is midship section area under water (26.3 m^2), H is water depth, V is ship speed, and where ΔV is the decrease of ship speed due to shallow water. This decrease of speed only applies when $\frac{A_M}{H^2}$ is smaller or equal to 0.05.

$$\frac{\Delta V}{V} = 0.1242\left(\frac{A_M}{H^2} - 0.05\right) + 1 - \left(tanh\left(\frac{gH}{V^2}\right)\right)^{\frac{1}{2}} \tag{5.11}$$

For the two investigated cases (i.e. displacement of 1,500 tonnes in shallow and deep water as shown in Table 17), the $\frac{A_M}{H^2}$ ratios were calculated as 0.23 or 0.12 (water depth either 35 or 50 feet) for the shallow water condition, and 0.0003 for the deep water condition (water depth 3,000 feet or >914 m) resulting in a decrease of ship speed only when investigating shallow water condition. Corrected, averaged powering results from sea trials, using a displacement of 1,500 tonnes for a speed range of 9 to 38 knots is given in Table 5.3, where the change in uncorrected to corrected power decreases with speed.

Table 5.3: Corrected Sea Trials Power For A Speed Range Of 9 To 38 Knots And A Displacement Of 1,500 Tonnes. All The Stated Values Were Calculated For The Catamaran (i.e. Two Demihulls With Two Water Propulsion Systems In Each Demihull). Stated Ship Speeds And Power Results Are Based On Averaged Sea Trial Runs At A Set Speed.

$\mathbf{V_s}$	$\mathbf{V_s}$	$\mathbf{R_{AA}}$	$\mathbf{R_{AW}}$	$\mathbf{R_{AS}}$	$\boldsymbol{\Delta R}$	$\boldsymbol{\Delta P}$	$\mathbf{P_{SC}}$
knots	m/s	kN	kN	kN	kN	MW	MW
8.9	4.6	3.4	30.4	0.8	34.6	0.3	0.8
12.0	6.1	3.4	30.4	1.3	35.1	0.4	1.9
15.0	7.7	3.4	30.4	2.0	35.8	0.5	3.7
18.6	9.6	3.4	30.4	2.9	36.7	0.6	6.3
23.5	12.1	3.4	30.4	4.3	38.1	0.7	9.9
25.1	12.9	3.4	30.4	4.9	38.7	0.7	12.1
26.7	13.7	3.4	30.4	5.5	39.3	0.8	14.7
29.4	15.1	3.4	30.4	6.5	40.3	0.9	17.6
32.4	16.7	3.4	30.4	7.6	41.4	0.9	20.8
35.5	18.2	3.4	30.4	8.7	42.5	1.0	24.4
38.2	19.7	3.4	30.4	9.9	43.7	1.1	27.6

5.2 Discussion of Measured Power compared to Sea Trials Power Results

Experimental testing was carried out using a single catamaran demihull only as discussed in Section 4.2 and to compare the extrapolated experimental power to sea trial results the estimated power has to be doubled (to account for two demihulls). Using corrected sea trials

data presented in Table 5.3, a comparison of sea trials power results compared to extrapolated power from experimental model testing is shown in Figure 5.3. As discussed in Section 5.1, the extrapolated power from model testing was expected to be in line with the deep water sea trials power and Figure 5.3 confirms this assumption. The extrapolated power from model testing underestimates the corrected deep water sea trials power in the speed range of 14 to 19 knots by about 5%, fits within 3% in the speed range of 19 to 21 knots, and overestimates corrected deep water sea trials power above 21 knots by 11% at 23.6 knots. The overestimation of power in the range above 21 knots is due to shallow water effects in the experimental testing at this speed, as stated in Section 5.1. Results in Figure 5.3 show that delivered power, calculated using a simplified waterjet testing method based on flow rate measurements and thrust, and extrapolated to full scale can estimate the power estimated in sea trials powering runs accurately within about 11%, which will include losses (e.g. inlet, pump, and nozzle losses) not accounted for in experimental measurements, and assumptions made for shaft, bearing, and installation efficiencies.

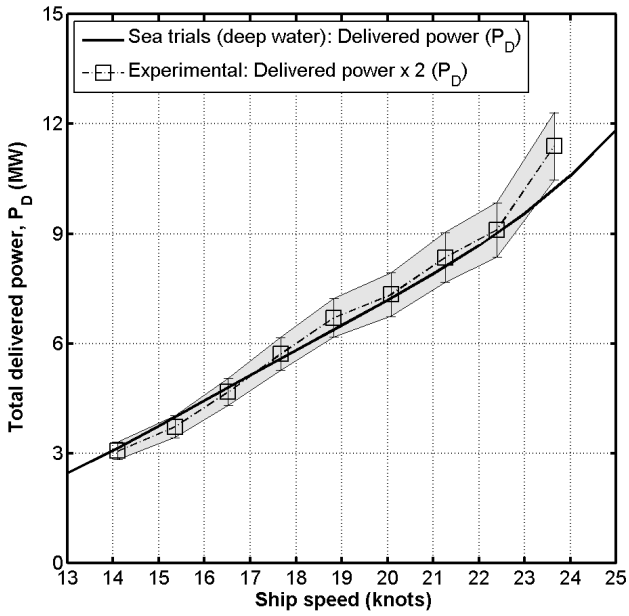

Figure 5.3: Comparison of shallow and deep water corrected sea trials power with double the delivered power (for two demihulls) extrapolated from model tests for a single demihull. The sea trials deep water power results fit the extrapolated power from model testing very well with a maximum overestimation of 11% at 23.6 knots and an underestimation of about 5% in the speed range of 14 to 19 knots. Error bars are based on results of flow rate uncertainty analysis used for momentum flux based power calculations.

5.3 Comparison to Propeller Performance Test Results

As part of the overall performance studies for medium-speed catamarans, a study testing propeller performance at medium-speed was carried out at AMC from 2012 to 2015 and the results and discussion of these tests are presented in Kamal (2015). The propeller propulsion

tests were carried out in parallel with the waterjet testing, using the same testing facilities but with a model of a new 130 m catamaran hull form which was optimised for medium-speeds. A comparison showing particulars, ratios and coefficients of the vessels tested with waterjet and propeller propulsion is given in Table 5.4. As stated in Section 4.1, the model to full scale ratio for the waterjet propulsion model is 21.6 and for the propeller propelled model 29.

Table 5.4: Comparison Of Vessels And Models Used For Waterjet And Propeller Model Testing Where "FS" Stands For Full Scale And "MS" For Model Scale And Subscript "DH" Stands For Single Demihull. Comparison Of Particulars Are Only Shown For Conditions Tested For Propulsive Performance Estimations; 1,500 t For 98 m Waterjet Propelled Vessel, 2,500 t And 3,640 t For 130 m Propeller Catamaran.

		98 m Catamaran Waterjet, (1,500 t)		**130 m Catamaran** Propeller, (2,500 t)		**130 m Catamaran** Propeller, (3,640 t)	
Particular	**Unit**	**FS**	**MS**	**FS**	**MS**	**FS**	**MS**
L_{WL}	m	92.9	4.3	124.8	4.3	122.6	4.23
$B_{WL,DH}$	m	4.5	0.21	6.35	0.22	6.4	0.22
T	m	3.3	0.15	3.23	0.11	4.1	0.14
S_{DH}	m^2	704.5	1.51	995.8	1.18	1,216.9	1.45
Δ	t	1,500	145	2,500	100	3,640	146
s/L	-	0.238		0.197		0.2	
$B_{WL,DH}/T$	-	1.364		1.97		1.56	
$L/B_{WL,DH}$	-	20.64		19.53		19.15	
C_B	-	0.592		0.476		0.552	
$\boldsymbol{\lambda}$	-	**21.6**		**29**		**29**	

Accurate comparison of propeller and waterjet performance powering estimations adds a few challenges to the experimental testing program. For the propeller and waterjet testing described in the research presented in this thesis, the propeller and waterjet powering estimations were carried out by two different researchers using slightly different models. The creation of a single, modular model that would allow to switch propulsion systems was considered, but rejected, as the time and effort to create a modular model (i.e. that would allow to adjust the stern shape as well as the propulsion system type) was not considered cost effective. For this reason, the propeller and waterjet powering performance testing was carried out using two different models which were scaled to be of the same length and beam.

Another consideration, that has to be taken into account when comparing powering predictions for propeller and waterjet propulsion systems is that for propeller propulsion direct measurements for power can be carried out (i.e. measured thrust, torque, shaft speed) while for waterjet propulsion some variables have to be measured indirectly (i.e. thrust) which adds more uncertainty to powering results. Appendage drag is also a variable that has to be taken into account, as the propeller propulsion adds a rudder and an a-frame for the propeller shaft

which adds drag to the overall resistance while only appendage for the waterjet propulsion is the trim tab. Comparison of the propeller and waterjet powering estimations presented in this thesis is limited to effective power (P_E), delivered power (P_D), overall propulsive efficiency (η_D), as well as scaled resistance results (i.e. scaled resistance due to the different full scale displacements of the propeller and waterjet driven models). A more detailed comparison of the propeller and waterjet powering estimations is given in Kamal (2015).

The propulsion train for the waterjet propelled vessel consisted of two waterjets for each demihull (see Section 4.1) while for the propeller propelled vessel there was only a single propeller and a comparison of the propulsion arrangement for the waterjet and propeller model demihulls is shown in Figure 5.4. The propeller model also included a rudder as an appendage while the waterjet model did not have any appendages except the trim tab. As stated in Section 4.2, only a single demihull was tested for the waterjet and propeller models to allow the model size to be increased to fit all the necessary propulsion equipment and measurement instrumentation. Waterjet and propeller propelled models were designed to be of approximately the same model length but using different model to full scale ratios as shown in Table 5.4.

Figure 5.4: Propulsion arrangements for single demihull models used for experimental waterjet and propeller testing. Vessels selected for experimental testing were a 98 m Incat wave-piercing catamaran with waterjet propulsion (left picture) and a newly developed medium-speed 130 m Incat wave-piercing catamaran with propeller propulsion (right picture).

A comparison of the full scale length to displacement ratio $\left(\frac{L_{WL}}{\nabla^{\frac{1}{3}}}\right)$ for the propeller and waterjet propelled vessels (see Table 5.5) shows that the displacements of the vessels cannot be directly compared as the length to displacement ratios are not the same. The closest comparison for both vessels in terms of length to displacement ratio would be the 1,500 tonnes displacement for the waterjet vessel and 3,640 tonnes for the propeller vessel.

Table 5.5: Comparison Of Length To Displacement Ratio $\left(\frac{L_{WL}}{\nabla^{\frac{1}{3}}}\right)$ For Propeller And Waterjet Propelled Vessels Showing Displacements Used For Propulsion Testing.

Waterjet vessel		**Propeller vessel**	
Displacement	$\frac{L_{WL}}{\nabla^{\frac{1}{3}}}$	**Displacement**	$\frac{L_{WL}}{\nabla^{\frac{1}{3}}}$
tonnes	-	tonnes	-
1,500	10.3	2,500	11.7
1,804	9.5	3,640	10.1

To investigate how the resistance results in terms of displacement for the 98 m and 130 m Incat wave-piercing catamarans compare, the resistance results of the 130 m catamaran were scaled to the 98 m catamaran and the resulting resistance compared to length Froude number is presented in Figure 5.5. Scaled displacements result in 1,031 tonnes (2,500 tonnes) and 1,583 tonnes (3,640 tonnes). One difference that should be noted when comparing the extrapolated results for the waterjet and propeller vessel is that for the propeller vessel ITTC'57 model ship correlation line was used for the ITTC 1978 extrapolation and the Grigson friction line for the waterjet vessel extrapolation as discussed in Section 4.4.3.

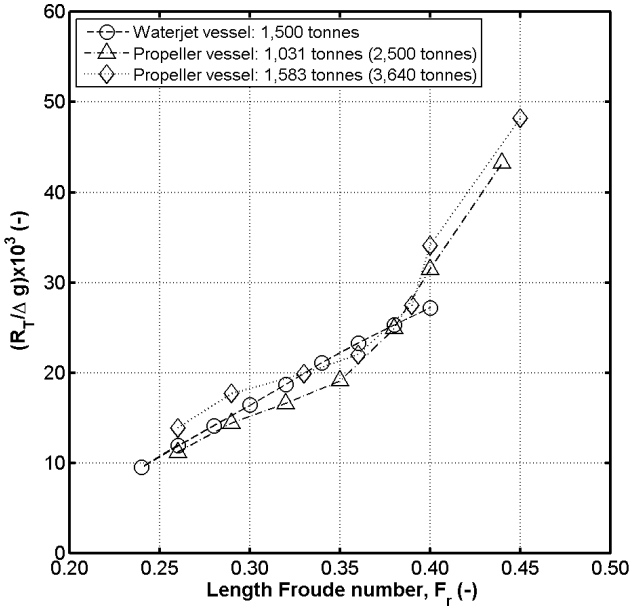

Figure 5.5: Comparison of dimensionless resistance, in terms of displacement, for the 98 m and scaled 130 m Incat wave-piercing catamarans.

As discussed in Chapter 2, the experimental testing for propeller and waterjet propulsion were carried out to establish recommendations in regard to which tested propulsion system was more applicable or efficient for new medium-speed Incat catamarans to be built in the future. To investigate if waterjet or conventional screw propeller propulsion was more applicable for medium-speed wave-piercing catamarans a comparison of extrapolated effective power (P_E),

delivered power (P_D), and overall propulsive efficiency (η_D) was conducted and extrapolated results are shown in Figure 5.6, where overall propulsive efficiency and powering results are shown in relation to length Froude number.

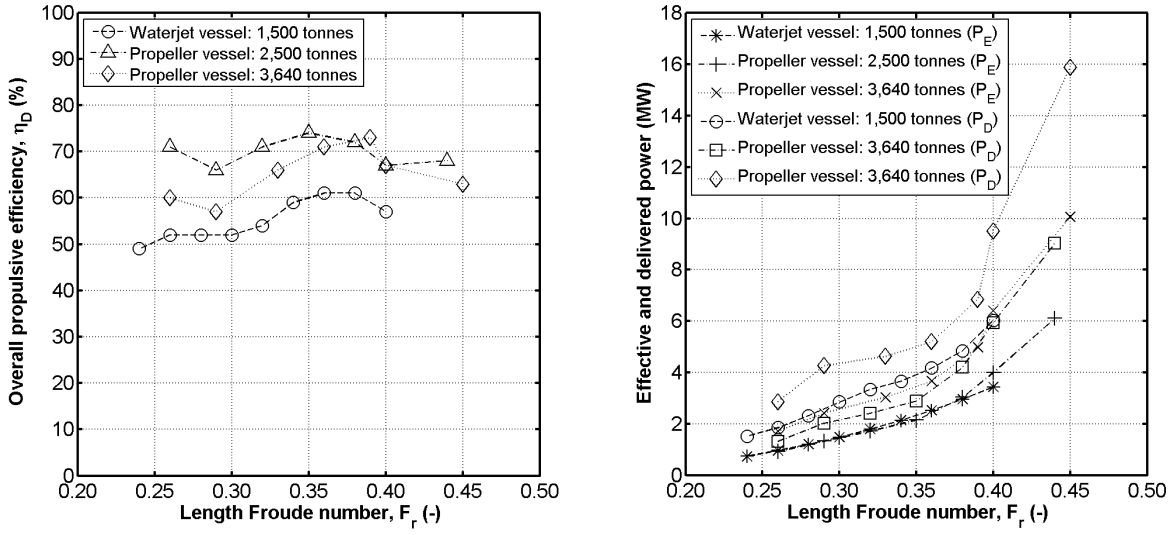

Figure 5.6: Comparison of overall propulsive efficiency as well as effective power and delivered power for a single demihull for waterjet and propeller vessels tested in experimental testing of propulsive research.

Based on the comparison shown in Figure 5.6, propeller propulsion is likely the more efficient propulsion system for medium-speed wave-piercing catamarans but as the overall propulsive efficiencies for both propulsion systems are within 60-70% at hump speed, other aspects need to be taken into account as well when selecting a propulsion system, such as draft of the vessel (propeller increases draft), appendage drag (propeller requires a rudder and struts), maintenance (waterjet propulsion equipment is located in the hull), safety (waterjet impeller is enclosed), acoustic signatures (lower for waterjet propulsion).

Chapter 6

Thrust Based Extrapolation Method

This chapter introduces a thrust based method for waterjet performance extrapolation. The main objective of the new testing procedure is to allow waterjet performance estimates based only on the waterjet self-propulsion test and a limited range of input and output parameters. Estimated power results are then compared to available sea trials data or full scale Computational Fluid Dynamics (CFD) studies. A simpler testing method for waterjet powering estimates would allow for easier and faster testing of waterjet models for hull series comparison studies and CFD validation purposes. For this study, thrust was not measured directly, but was calculated (see Section 3.5) based on measured flow rates, wake fraction for inlet velocity, and nozzle dimensions as shown in technical drawings supplied by waterjet unit manufacturer Wärtsilä.

The first section of this chapter outlines the typically used ITTC waterjet testing method based on generic waterjet propulsive performance prediction guidelines. The second section outlines the required testing for the proposed thrust based waterjet testing as well as the required input and output. The third and last section details the steps required for data reduction and extrapolation for the proposed thrust based waterjet performance estimation.

6.1 Differences from the Standard ITTC Procedure

Waterjet propulsive performance prediction is usually carried out using an ITTC based approach and can be refined by using adjustments and corrections based on the testing facility carrying out the experimental testing. The procedure, given by ITTC waterjet propulsive performance prediction guidelines 7.5-02-03-01.1, 7.5-02-05-03.1, 7.5-02-05-03.2, and 7.5-02-05-03.3, is meant to be used as a guide in the prediction of powering performance of waterjet driven vehicles using propulsion tests and describes the self-propulsion test itself and the extrapolation procedure from model scale to full scale. The ITTC procedure is generally applicable for propulsive performance prediction for marine vehicles driven by waterjets with

flush intakes and the procedure is kept as generic as possible, so that to test other waterjet configurations only minor adaptations are required. To collect all parameters for a waterjet performance analysis, the standard ITTC procedure requires results of three separate tests which are: bare-hull resistance test, waterjet system test (or pump loop test), and waterjet self-propulsion test. A waterjet system test (or pump loop test), using a larger scale waterjet propulsion system than used for the self-propulsion test, is carried out for cavitation purposes and determination of pump characteristics such as flow and head coefficient. Therefore, for the standard ITTC method, three different tests and two differently scaled model waterjet units are required, which illustrates the complexity of this testing method.

The main difference between the introduced thrust based extrapolation method and the generic ITTC procedure is that only the self-propulsion test (see Section 4.6) has to be carried out for the estimation of power. The only additional requirement is that flow rate or thrust has to be measured (directly or indirectly), and for the research presented in this thesis this was achieved by measuring flow rate independent of the self-propulsion test by carrying out a static flow rate measurement test as described in Section 4.5. If the testing facility is able to measure velocity, thrust, or flow rate directly in the self-propulsion test, this would simplify testing as the static flow rate measurement test could be avoided.

Measured quantities, which need to be measured directly or calculated include: volumetric flow rate (Q_J), static pressure at capture area (one position on the hull at the centreline of the capture area), sinkage of the nozzle, and velocity distribution in the capture area. Additional measurements include quantities such as model speed, resistance (or external tow force), impeller torque and rate of revolutions, water temperature, fore and aft sinkage or running trim and sinkage.

Bare-hull resistance tests are carried out with closed inlets and nozzles, and depending whether testing is carried out with or without water in the waterjet tunnel, a correction for the entrained water is to be included. For the waterjet self-propulsion testing inlets and nozzles are opened and no correction for entrained water has to be taken into account. Additional tests (which can be part of the three main tests or carried out as separate tests) are for example boundary layer measurements (to determine momentum wake fraction used to calculate inlet velocity), trim tab tests optimisation tests (for optimal trim tab angle for experimental testing) or calibration tests.

6.2 Required Testing for Thrust based Waterjet Power Estimation

Required experimental testing for the thrust based extrapolation method presented in this study consisted of a flow rate measurement test, as described in Section 4.5, and a waterjet

self-propulsion test as described in Section 4.6 and schematic representation of the tests is shown in Figure 6.1. As discussed in Section 4.4, a bare-hull resistance test was carried out as well but this test was conducted to collect a full resistance data set for this vessel, as this hull had not been model tested before, and for determination of thrust deduction in conjunction with results of the waterjet self-propulsion test. Another use for the bare-hull resistance data in this research was to investigate drag-thrust equilibrium and to calculate effective power for comparison with effective power estimated using force at zero thrust ($F_{T=0}$) established in self-propulsion test as discussed in Section 4.6.6. A flow chart showing a summary of output parameters of the static flow rate measurement test, boundary layer measurement test, and waterjet self-propulsion test is shown in Figure 6.2 and waterjet self-propulsion test measurements are discussed in detail in Section 4.6.

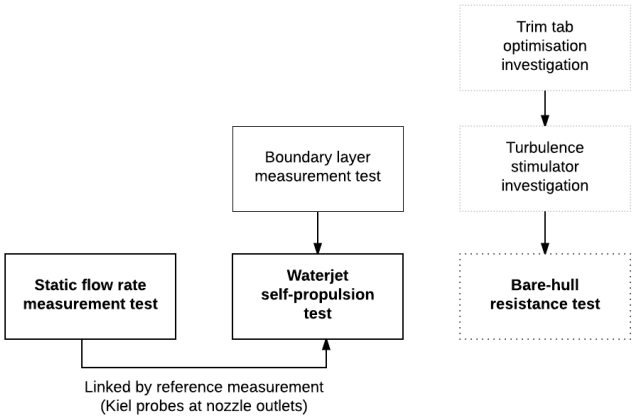

Figure 6.1: Testing required for thrust based power estimation method carried out for the presented research. For this project a bare-hull resistance test was carried out as well, but this was done to collect a full resistance data set for the 98 m Incat and for determination of thrust deduction in conjunction with results of the waterjet self-propulsion test. The static flow rate measurement test and the self-propulsion test are linked by a reference measurement using a single Kiel probe at each nozzle.

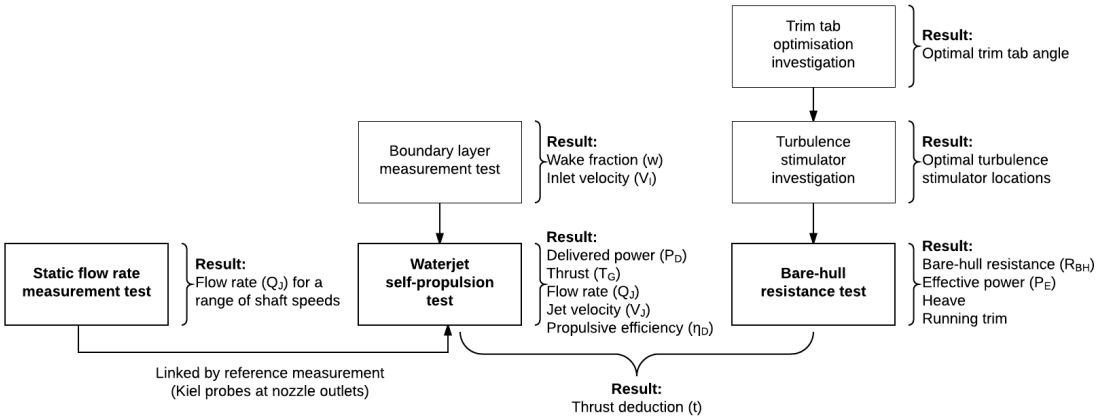

Figure 6.2: Output parameters of the static flow measurement test, boundary layer measurements and waterjet self-propulsion test. The reference Kiel probe measurements carried out in the static flow rate measurement test and self-propulsion test are used to link both test together to determine flow rate used for performance estimation.

Flow rate results calculated using static flow rate measurement and waterjet self-propulsion test were then used to determine gross thrust (see Section 3.5) using Equation 6.1, where $\dot{m}$ is mass flow rate, ρ is fluid density, Q_J is volumetric flow rate, A_n is nozzle area, V_J is jet velocity, w is wake fraction, and V_I is inlet velocity.

$$T_G = \dot{m}\,(V_J - V_I) = \rho Q_J\,(V_J - V_I) = \rho Q_J \left(\frac{Q_J}{A_n} - (1-w)V\right) \tag{6.1}$$

Output parameters of the resistance related tests:

- **Trim tab investigation:** Optimal trim tab angle for a defined speed, resulting in an angle of 5 degrees downward of vessel baseline as discussed in Section 4.4.7.
- **Turbulence stimulator investigation:** Placement and number of lines of turbulence stimulators on wave-piercing bow, resulting in two lines of turbulence stimulators as discussed in Section 4.4.5.
- **Bare-hull resistance test:** Model speed, aft and forward sinkage used to calculate sinkage (heave) and running trim, and model resistance and results are given in Section 4.4.9.

Using the measured output parameters from the static flow rate measurement test, boundary layer measurement test, waterjet self-propulsion test, and to a lower degree the bare-hull resistance test, data can be reduced and extrapolated to full scale and a breakdown of the steps required is discussed in Section 6.3.

6.3 Data Reduction and Extrapolation

As discussed in the previous section, the experimental model testing carried out with the static flow rate measurement test, boundary layer measurement test, and waterjet self-propulsion test resulted in various parameters which were used to calculate powering performance, extrapolation to full scale and validation with powering sea trials data as discussed in Section 5.2. When investigating momentum changes based on energy fluxes at different waterjet stations, flow rate is the most important parameter and had to be measured as accurately as possible to lower uncertainty in power estimations. To measure flow rates, several methods were available as discussed in Section 4.5 and the thrust based extrapolation method used an indirect flow rate measurement method in the form of a static flow rate measurement test, where the expelled water from the waterjet was measured as a function of time, resulting in mass flow rate.

As the flow rate was not directly measured in the self-propulsion test, but by using a separate test, a connection between the two tests had to be defined. The linkage of static flow rate

measurement test and waterjet self-propulsion test was achieved by using a Kiel probe at each waterjet nozzle outlet (port and starboard) to measure the pressure at this location. The same measurements were then recorded in the waterjet self-propulsion test and using these pressure measurements and the results of the static flow rate measurement test allowed the determination of the mass flow rate in the waterjet self-propulsion test and a schematic representation is shown in Figure 6.3. As the reference measurement at the nozzle, was determined by the flow rate at this location, no pressure differences were expected, so that the pressure at this location for the flow rate measurement test accurately represent the condition for the waterjet self-propulsion test.

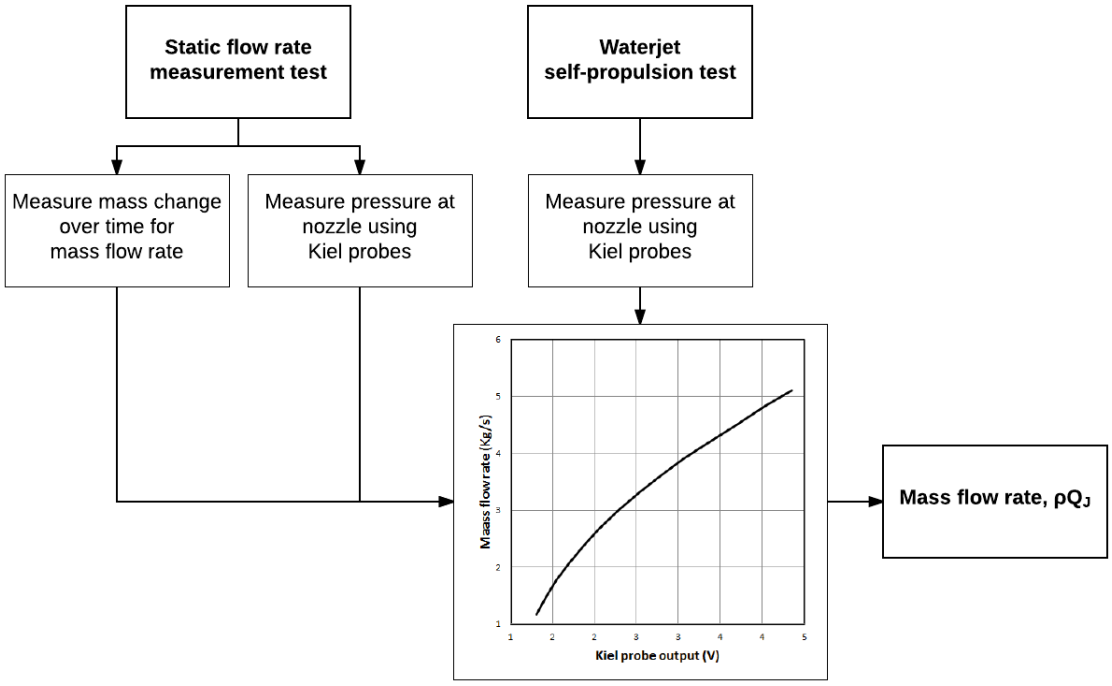

Figure 6.3: Methodology for linking static flow rate measurement test and waterjet self-propulsion test to determine flow rates. The output of the static flow rate measurement test was a plot showing Kiel probe output plotted against mass flow rate. The measured reference Kiel probe measurements from the waterjet self-propulsion test were then used together with the Kiel probe vs. mass flow rate plot to determine flow rates for each self-propulsion test run.

The next step was then to use recorded self-propulsion test results, and the procedure to establish the self-propulsion point for each speed, as described in Section 4.6.4, to determine the mass flow rate for each speed. After the mass flow rate for each speed in the waterjet self-propulsion test was determined, and using the wake fractions estimated using boundary layer measurements discussed in Section 4.6.3, gross thrust (T_G) could then be calculated using Equation 6.1. A schematic representation of the required steps to calculate gross thrust (T_G) is shown in Figure 6.4.

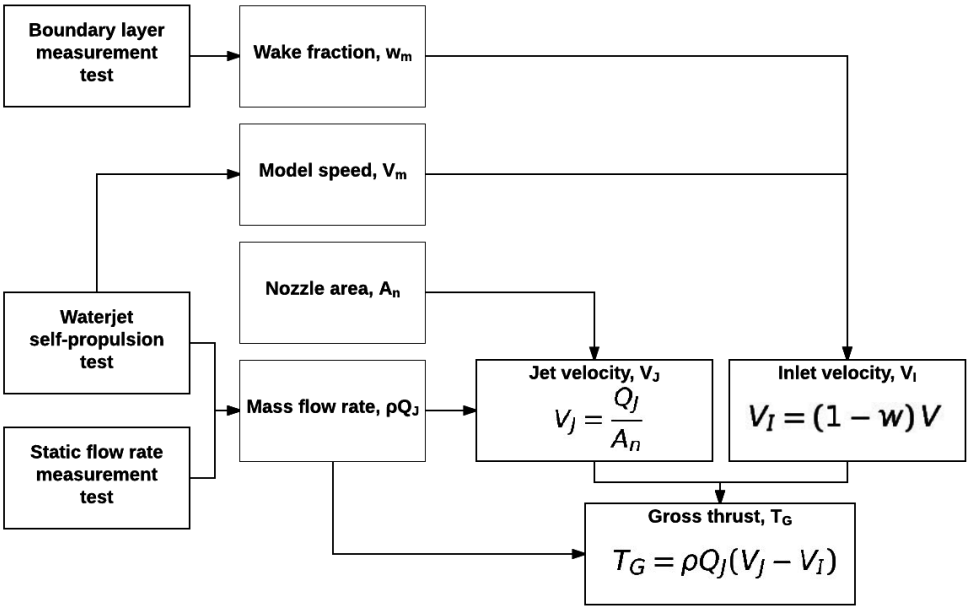

Figure 6.4: Schematic representation of steps required to establish gross thrust (T_G) using static flow rate measurements, waterjet self-propulsion, and boundary layer measurements. Nozzle area (A_n) was calculated using the model nozzle diameter which was scaled using full scale nozzle diameter as supplied by waterjet unit manufacturer Wärtsilä and cross checked measuring physical model scale nozzle diameter.

Applying procedure outlined in Figure 6.4 for each speed measured in the waterjet self-propulsion test resulted in all model scale thrust results for the tested speed range. Model thrust was then scaled to full scale thrust using Equation 6.2, where T_{Gs} is full scale thrust, T_{Gm} is model scale thrust, λ is model to full scale ratio (21.6), and where ρ_s and ρ_m are salt water and fresh water densities.

$$T_{Gs} = T_{Gm}\, \lambda^3\, \frac{\rho_s}{\rho_m} \tag{6.2}$$

Full scale flow (Q_{Js}) rates were then calculated using methodology as discussed in Section 4.6.9, where the equation for gross thrust ($T_G = \rho Q_J (V_J - V_I)$) was used to determine volumetric flow rate (Q_J) using as input the full scale thrust scaled from model scale (T_{Gs}), sea water density (ρ_s), and the full scale nozzle area (A_{ns}) as shown in Equation 6.3.

$$T_{Gs} = \dot{m}_s\,(V_{Js} - V_{Is}) = \rho_s Q_{Js}\,(V_{Js} - V_{Is}) = \rho_s Q_{Js}\left(\frac{Q_{Js}}{A_{ns}} - (1 - w_s)V_s\right) \tag{6.3}$$

Alternatively volumetric flow rate (Q_J) can also be scaled to full scale by using Froude scaling as discussed in Rispin (2007) and shown in Equation 6.4, where Q_{Js} is full scale volumetric flow rate, Q_{Jm} is model scale volumetric flow rate, and ρ_s/ρ_m is salt water density to fresh water density.

$$Q_{Js} = Q_{Jm}\lambda^{2.5}\frac{\rho_s}{\rho_s} \tag{6.4}$$

The next step of the extrapolation was then to calculate full scale jet velocity (V_{Js}), using the determined volumetric flow rate and inlet velocity (V_{Is}). To determine the full scale inlet

velocity using the definition of inlet velocity $V_{Is} = (1 - w_s)V_s$, full scale wake fraction (w_s) had to be known. Model wake fraction was scaled to full scale using Equation 6.5, where w_s is full scale wake fraction, w_m is model scale wake fraction, C_{Fs} is full scale frictional resistance coefficient, and C_{Fm} is model scale frictional resistance coefficient.

$$w_s = w_m \frac{C_{Fs}}{C_{Fm}} \tag{6.5}$$

Energy fluxes at momentum flux station 7 and 1 were then used to calculate effective pump power (P_{PE}) as discussed in Bose (2008) and shown in Equation 6.6, where ρ is fluid density, Q_J is volumetric flow rate, V_J is jet velocity, η_n is nozzle efficiency taken as 0.98, and η_i is inlet efficiency ($\eta_i = \frac{E_3}{E_1}$) which is a measure of loss incurred from flow entering the waterjet inlet and calculated using energy at station 1 and 3 discussed in Delaney et al. (2009) and Takai et al. (2011), V is ship speed, and w is wake fraction.

$$P_{PE} = \frac{1}{2}\rho Q_J \left(\frac{V_J^2}{\eta_n} - \eta_i V^2 \left(1 - w\right)^2 \right) \tag{6.6}$$

Effective pump power (P_{PE}) and pump efficiency (η_{Pump}) based on waterjet unit benchmark test (see Section 4.6.5) supplied by manufacturer Wärtsilä were then used to calculate delivered power (P_D) as shown in Equation 6.7.

$$P_D = \frac{P_{PE}}{\eta_{Pump}\, \eta_{Inst}} \tag{6.7}$$

Overall propulsive efficiency (η_D) discussed in Section 4.6.7 was then calculated using Equation 6.8, where P_E is effective power $P_E = R_{BH}V$ using bare-hull resistance (R_{BH}) and ship speed (V), and P_D is delivered power as shown in Equation 6.7.

$$\eta_D = \frac{useful\ work}{total\ work} = \frac{P_E}{P_D} = \frac{R_{BH}V}{\frac{P_{PE}}{\eta_{Pump}\, \eta_{Inst}}} \tag{6.8}$$

Chapter 7

Conclusion and Future Work

This study set out to investigate waterjet propulsive performance prediction using self-propulsion testing of a catamaran in the Australian Maritime College (AMC) towing tank. The reason and motivation for this research was to propose a simpler, thrust based waterjet powering extrapolation method for accurate powering predictions. This project sought to gain knowledge in experimental model testing and to propose a new thrust based extrapolation method for waterjet powering prediction. An expected outcome of this thesis was to answer the main research questions:

- Which is the most accurate extrapolation method for a waterjet propeller ship model?
- What is the minimum requirement for successful waterjet self-propulsion test?
- What does the waterjet thrust plotted against towing force look like for a waterjet propulsion system compared to the same plot for a propeller propelled vessel?
- What is the speed at which thrust breakdown occurs for the 98 m Incat catamaran ferry? Thrust breakdown was defined as the point where head rise, torque and efficiency decrease due to cavitation.

While carrying out experimental research using model testing and analysis of test results new areas of interest requiring further investigation came to light and some are included in the recommendations for future work (see Section 7.1). The new questions to be answered in the discussion of the waterjet powering prediction results are:

- What is useful work (i.e. effective power, P_E) for waterjet propulsion in relation to overall propulsive coefficient (OPC) where overall propulsive efficiency is defined as $\eta_D = \frac{P_E}{P_D}$?
- What is thrust deduction for waterjet propulsion and can thrust deduction be negative?

Recommendations and proven methods for estimating waterjet powering performance were given by The Specialist Committee on Validation of Waterjet Test Procedures (ITTC) and, as a base for a complete powering prediction, required three tests to be carried out which are bare-hull resistance test (resistance components), waterjet system test (cavitating environment, head and flow rate coefficients), and waterjet self-propulsion test (non cavitating environment, flow rates, effective jet system power). One of the objectives of this study was to propose a new, thrust based extrapolation method using just the results of the waterjet self-propulsion test. The proposed thrust based extrapolation method presented in Chapter 6 allowed the full scale powering sea trial power to be predicted within 5% at hump speed and within 11% at 24 knots due to increased shallow water effects at high-speed. Results from the recommended ITTC based testing method, discussed in Section 6.1, would expected to be more accurate, as the waterjet unit performance parameters would be establish using an additional waterjet system test, which is not required for the thrust based method. The thrust based extrapolation method requires more testing (i.e. other models) and a wider range of speeds and thrust to establish overall validity, as only a single set of propulsion test results was used to validate the new method, as indicated in recommendations for future testing in Section 7.2.

Minimum measurement requirements for a successful waterjet propulsion test, as used for this study, were model speed, forward and aft sinkage (used to calculate heave and running trim), drag (for resistance in bare-hull resistance test and for self-propulsion points in waterjet self-propulsion test), static pressures (for pump head, H_{35}), shaft speed, shaft torque, impeller thrust, and most important flow rate at the waterjet outlet (i.e. nozzle) to determine thrust. As the new, proposed extrapolation method was thrust based, thrust had to be measured as accurately as possible (i.e. for lowest errors and uncertainty) using either direct thrust of flow rate measurements in self-propulsion test or indirect flow rate measurements used in combination with the waterjet self-propulsion test in the form of a static flow rate measurement test. Together these measurements allowed the determination of required power and overall propulsive efficiency.

Testing a single demihull and using only the results of waterjet self-propulsion testing was demonstrated to be a suitable and accurate (within 10%) tool for waterjet powering prediction for medium-speed wave-piercing catamarans. When comparing results of extrapolated full scale waterjet powering results with propeller powering results it was demonstrated, that the overall propulsive efficiency of the propeller propulsion was about 10% higher in the hump speed region at a length Froude number of 0.36. Powering requirements in terms of displacement also put propeller propulsion ahead of the waterjet propulsion but another consideration had to be taken into account which was, that the tested models were of about the same length but the full scale vessels were not. Additional considerations to be taken into

account are the increase of draft when using propeller propulsion, more extensive maintenance as propeller and shaft are outside the vessel, and the increase in acoustic signature (i.e. noise) of the propeller when compared to a waterjet unit. As shown in Section 5.3, when scaling the extrapolated full scale resistance results of the tested 130 m propeller vessel to the 98 m waterjet vessel the resistance results varied by less than 10%.

Limitations of the research are the restricted speed range tested (i.e. hump speed range) of length Froude number range of 0.24-0.4 or 14-24 knots full scale. Another limitation was that due to the extensive setup required for testing and the limited testing time only a single displacement and static trim was tested. The static flow rate measurement test was carried out twice; to validate the results of the first test, to extend the shaft speed range, and to decrease uncertainty in flow rate measurements as this parameter was defined as the main parameter of the powering prediction and was to be measured as accurately as possible. Calculated uncertainties for static flow rate measurements varied from 2-4% dependent on shaft speed as discussed in Section 4.5.5.

Thrust breakdown occurs when the mass flow through the waterjet system collapses due to extreme cavitation. Therefore, as thrust breakdown requires cavitation, results from a non-cavitating towing tank test will not give any reasonable answer to the speed range where thrust breakdown occurs. There was a small measured drop in thrust at about 19.5 knots (i.e. a length Froude number of about 0.33 as shown in Figure 4.53 in Section 4.6.10) but if this was directly related to a breakdown in thrust could not be determined. Using just the available experimental test data was not enough to establish the speed at which thrust breakdown occurs and a separate waterjet pump test would have to be carried out using a cavitation tunnel and a larger model of the waterjet for model testing. Research carried out by Bulten (2006) for three different sized waterjets, which used the geometry of the same waterjet unit (Lips Jet 120E) as used for this study, determined that thrust breakdown occurs at a ship speed of 17 to 38 knots depending on the size of the waterjet.

When investigating thrust deduction for propeller propulsion there is a physical explanation, such that the propeller creates a low pressure area behind the hull which increases the normal pressure forces (i.e. pressure drag) and the ship hull experiences a backward suction. This can also be indirectly measured through the bare-hull resistance, from bare-hull resistance test, and thrust of propeller (i.e. thrust measured in propeller self-propulsion test using a self-propulsion propeller dynamometer). For waterjet propelled vessels there is no physical explanation for thrust deduction since waterjet thrust cannot be measured directly and thrust deduction also cannot be measured through bare-hull resistance of vessel and impeller thrust of waterjet. The term thrust deduction is commonly used (or misused) for waterjet propelled vessels to express the difference between the bare-hull resistance of the vessel and the calculated thrust of the waterjet and accordingly the thrust deduction factor depends on

how the waterjet thrust was calculated. Sources of deviation for thrust deduction in relation to waterjet propulsion are:

- effect of inlet opening on vessel resistance;
- effect of transom ventilation and transom resistance;
- neglected friction and pressure related stresses in momentum balance;
- new, partially developed boundary layer aft of inlet lip;
- boundary layer model.

Considering all the deviations possible in the calculation of thrust deduction for waterjet propelled vessels, thrust deduction is not as meaningful as for propeller propelled vessels and should be considered more as a correlation factor, which depends on how accurate thrust measurements, using direct or indirect thrust measurements, were carried out in the waterjet performance testing and analysis of the test results. To allow for the comparison of thrust deduction of waterjet propelled vessels the commonly used definition of thrust deduction fraction of $t = 1 - \frac{R_{BH}}{T_G}$ should be used as this allows comparison of thrust deduction fraction results with published results from other waterjet propulsion performance studies.

As the waterjet powering prediction was carried out in the hump speed region, a bare-hull resistance test was carried out for a length Froude number range of 0.1 to 0.5 (full scale speed 6 to 28 knots), showing that the hump speed of the measured displacements (1,500 and 1,804 tonnes) was at a length Froude number of about 0.37. Considering the hump speed established in the bare-hull resistance test the speed range to be tested for the waterjet self-propulsion test was set as length Froude number range of 0.22 to 0.42 (full scale speed 14 to 24 knots) which also included some lower speed used to validate Computational Fluid Dynamics (CFD) in another part of the resistance and propulsion research and discussed in Haase (2015).

Answering the question of which extrapolation method is more accurate: the thrust based extrapolation method presented in this study or the general ITTC method for determination of waterjet propulsive performance presented in ITTC (2011c) would lead to the conclusion that the ITTC based method using three tests (bare-hull resistance test, waterjet system test, waterjet self-propulsion test) would be more accurate. The reason is, that in the thrust based extrapolation method the waterjet unit performance parameters were taken from waterjet unit benchmark test data supplied by the manufacturer which were measured in model scale and then scaled to full scale and therefore already include scaling errors. Further scaling errors are introduced when scaling the waterjet unit benchmark results to conditions that were not directly measured in the benchmark test as discussed in Section 4.6.6. The ITTC based

method establishes the actual waterjet unit performance parameters using the waterjet system test (also called pump loop test) which measures impeller torque coefficient (K_Q), head coefficient (K_H), and flow coefficient (K_{QJ}) which will be more accurate than the waterjet unit benchmark data used for the thrust based extrapolation method. The disadvantage of the ITTC based method is that it requires three different tests and the model waterjet propulsion system in two different scales: a larger scale model for the waterjet system test and a smaller scale model for the waterjet self-propulsion test. This means a lot of testing in different facilities, but the resulting performance results can be very accurate. The thrust based extrapolation method on the other hand requires less testing and only a single model waterjet propulsion system for the waterjet self-propulsion test, but will not be as accurate as the ITTC based method. The thrust based extrapolation could be used to limit testing time required for series testing of waterjet propelled vessels when the impact of decrease of accuracy is balanced against the increase of testing time required for the full ITTC based waterjet performance testing method.

Based on the experiences collected in the experimental waterjet propulsion testing in the AMC towing tank and model test basin a list of recommendations for future waterjet testing was written up and is presented as two separate lists, where the first list, presented in Section 7.1, gives a set of general recommendations while the second list, presented in Section 7.2, gives a set of AMC specific recommendations for future waterjet testing. The topics discussed for the recommendations are stock waterjet, changes of test setups, changes in instrumentation and equipment, and guidance (i.e. lessons learned or as a how to) for waterjet propulsion testing, and improvements in terms of accuracy in measurements of velocities in boundary layer measurement tests.

7.1 General Recommendations for Future Waterjet Testing

Based on experience gained in the project, experimental testing, and data analysis, a set of general recommendations for future waterjet testing was created to allow for more accurate performance estimates of waterjet propelled models which are as follows:

- The thrust based extrapolation method was used for extrapolation of these experimental tests and to validate the applicability of the method further extrapolations using other existing data or result of future waterjet testing should be carried out. This will also require full scale validation results in the form of full scale powering data or results of full scale Computational Fluid Dynamics (CFD) investigations.
- The selected size of the model and propulsors made pressure measurements difficult, and consequently gave poor results in terms of measured values as well as repeatability.

To rectify this, larger models should be employed if possible, or a larger testing facility at another institution. If model size cannot be increased due to shallow water and blockage restrictions in the AMC towing tank, an investigation should be considered to find more appropriate pressure transducers.

- Alternative methods for torque and thrust measurements should be investigated as the results from self-propulsion dynamometers gave poor results of impeller thrust but good results of shaft torque. Alternatively how multiple propulsion systems can be installed and calibrated should be investigated to allow for constant impeller thrust and shaft speeds.

- Alternative flow measurement techniques should also be investigated. As flow rate measurement of the jet is crucial for accurate thrust predictions, the flow rate measurement test (i.e. "Bucket Test") could be replaced with direct flow measurement using Laser Doppler Velocimetry (LDV) as recommended by ITTC (2011c) to minimise errors and uncertainties. An alternative flow rate measurement method was described in Eslamdoost (2014), where a T-junction was used to redirect the nozzle discharged flow perpendicular to the nozzle exit. An axial momentum flux balance equation was then used to establish volumetric flow rate. This method of flow rate determination requires two tests to be are carried out at each speed: the first test (without T-junction) determines sinkage, trim and pump revolution at the self-propulsion point and the second test, carried out at the established shaft speed at the self-propulsion point, measures flow rate using the T-junction.

- Add additional measurements at momentum flux stations 3 and 5 (see Figure 2.1) to more accurately determine losses such as ζ_{13}, ζ_{57} at inlet and outlet or other between momentum flux relevant waterjet stations. More accurate determination of ζ_{13}, ζ_{57} would result in greater accuracy when determining effective pump power ($P_{PE} = P_{JSE}+\zeta_{13}E_0+\zeta_{57}E_7$), delivered power ($P_D = P_{PE}/(\eta_{Pump}\eta_{Inst})$) and therefore overall propulsive efficiency ($\eta_D = P_E/P_D$). To allow a more accurate determination of pump effective power (P_{PE}), a better estimate of nozzle efficiency (η_n) and inlet efficiency (η_i) would be useful. To achieve this instrumentation has to be added to allow measurement of speeds at momentum flux stations 3 and 5 to allow for more accurate determination of inlet and outlet losses (ζ_{13} and ζ_{57}) as well as the calculation of momentum flux (E_3 and E_5) as well as inlet efficiency (η_i).

- To allow more accurate results of experimentally established boundary layers and momentum wake fractions a new, detailed boundary layer test should be carried out, using the project demihull and the same setup as used for the boundary layer measurement presented in this study but testing a bigger range of speeds. This would allow re-

finement of the boundary layer measurement technique using pitot-static tubes and boundary layer traverse, as discussed in detail in Section 4.6.3.

- 10 mm increments of distance below the hull were used to measure boundary layer velocities, but taking into account the changes of velocities between zero distance from the hull and the free stream speed at the distance of the boundary layer thickness (see Figure 4.37 in Section 4.6.3) it is recommended, for future testing, to use smaller increments (e.g. 5 mm) in change of vertical distance from the hull below the boundary layer thickness but to increase measured increments after reaching the boundary layer thickness. This will allow a more accurate determination of the speed changes below the vertical distance at the boundary layer thickness.

- Record additional measurements, in either self-propulsion test or in an additional test, to make estimates for transom stern drag, or pressure, and to establish the speed at which the transom changes from wet to dry. Initial estimates can be made using results presented in Haase (2015) which includes measurements at which speed the transom changes from wet to dry and transom stream behaviour tested at different speeds in the AMC towing tank using visual streamers attached to the trim tab.

7.2 AMC Related Recommendations for Future Waterjet Testing

A set of AMC related recommendations for future waterjet testing was created to allow for the adjustment of experimental waterjet testing techniques and to minimise test setup related errors and the list is as follows:

- As there are currently no stock waterjets available for testing, effort should be put into designing and fabricating precision stock waterjets, in different sizes, for use in experiments which incorporate instrumentation for measurements. A good example for typical waterjet stock models is discussed in ITTC (2002) and a 3D rendering is shown in Figure 2.4 in Section 2.2 of this thesis.

- Motors used for waterjets propulsion should be chosen to have the requisite power with controllers able to accurately maintain a given shaft speed for multiple engines, using a Controller Area Network (CAN) bus for the electric engines to communicate with each other without the need for a host computer. The currently available electric motors, Dunkermotoren model BG-75x25 CI, did not work well when controlled using CAN and were controlled individually (each using its own control computer), which resulted in slightly different set shaft speeds for the port and starboard waterjet propulsion system of the tested, single catamaran demihull.

- Speed range for future waterjet self-propulsion testing should be extended to a wider range of tested speeds (i.e. low-speed range and high-speed range) and therefore measured thrust than presented for this research to allow validation of thrust based extrapolation method for a wider range of speeds than just in the hump speed range.

Appendix A

Model Building and Design

As one the restrictions of the model was weight, the selected method of construction for the catamaran demihull model was carbon fibre sandwich construction using wet layup and it was built within the requirements and the structural design manufacturing tolerances as required by ITTC (2011d). To define the shape of the model hull, a 3D surface model of the 98 m Incat wave-piercing catamaran (hull 61) HSV-2 *Swift* (provided by the vessel's designer Revolution Design Pty Ltd) was used. A rendering of the single model demihull is shown in Figure A.1.

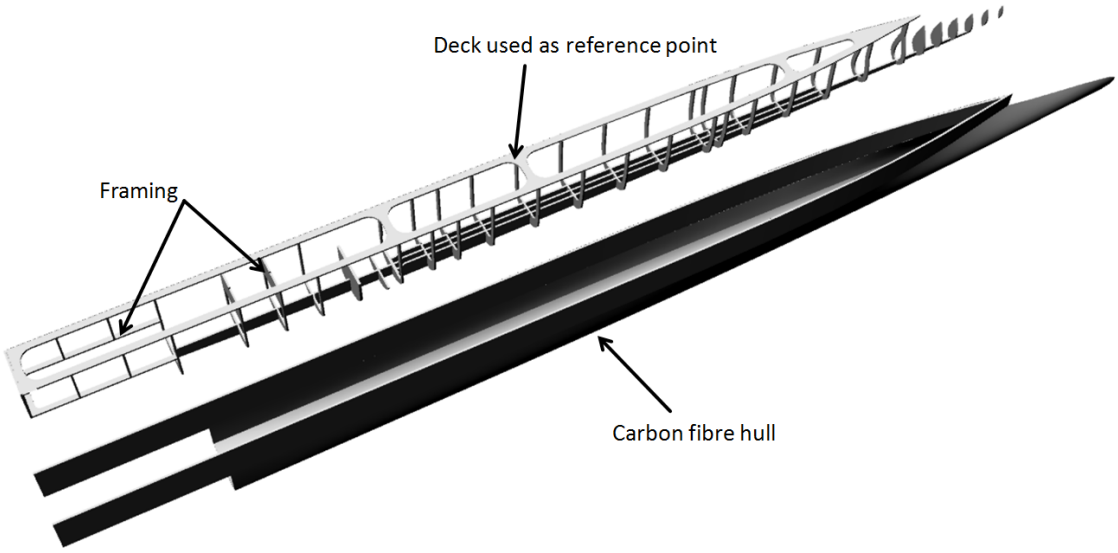

Figure A.1: Demihull model showing the structural construction (top) and the carbon fibre hull (bottom). To allow for ease of measurements inside the deck level was established as a reference plane. The gap at the stern allows for the addition of the waterjet tunnels created using 3D printing methods.

The model itself was constructed in four steps by Mr Stuart Phillips. The first step was the assembly of the structural framing using a series of frames cut from a carbon fibre sandwich plate, with a thickness of 7 mm (using one layer of carbon fibre on each side of the sandwich

material) as shown, with the finished structural frame, in Figure A.2. The structural framing consisted of 22 lateral frames and one main longitudinal frame onto which the lateral frames were situated using a slotting system for accurate positioning. The deck plate was cut from 7 mm carbon fibre sandwich (the same plate as the lateral frames) and included openings to allow access to the interior of the model hull for assembly of the propulsion system, sensors, attachment of carriage posts. The deck was used as the model's measurement reference surface. The second step was the creation of a wooden male plug used as a basis for creating the female mould for laying up of the final carbon fibre hull. The wooden plug used for the female mould consisted of a central board and a series of frames cut 3 mm shy of the shell extent, as shown in assembled form in Figure A.3. The frames were then covered with thin strips of wood to form the shape of the outer hull of the model and the finished plug is shown in Figure A.4.

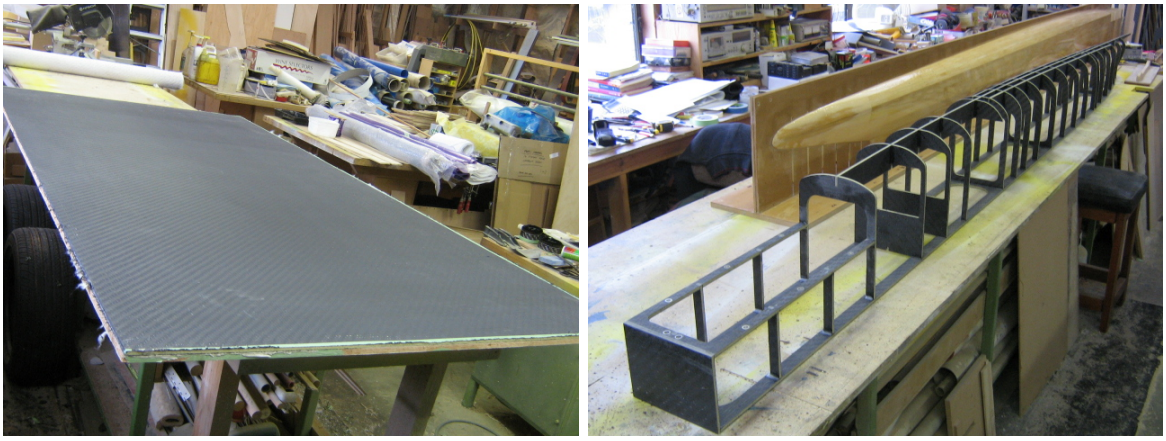

Figure A.2: Left picture shows 7 mm carbon fiber sandwich used for the model's structural frames. The plate consists of one layer of carbon fiber on each side of the sandwich material. The right picture shows the assembled structural frame of the model.

Figure A.3: Assembled frames and centre board for plug used to create female mould photographed in the workshop of the model builder.

Figure A.4: Finished plug used for the creation of the female mould.

The third step was to use the wooden male plug to create a fibreglass female mould. This female mould was then used to lay up the model hull using a carbon fibre and sandwich construction method. The assembly of the final hull shell and the previously constructed structural framing is shown in the left photo in Figure A.5. The finished demihull model of the wave piercing catamaran, without the waterjet tunnels fitted, was delivered by model builder in September 2012, as shown in the right photo in Figure A.5.

Figure A.5: Finished plug used for the creation of the female mould (left) and finished single demihull model of 98 m INCAT wave piercing catamaran HSV-2 *Swift* (right).

After painting, the final hull surface was marked on the starboard side (the location of still and video cameras in the selected testing setup) with station numbers and waterlines for two selected testing displacements. Two rows of turbulence stimulation stimulators were attached to the wave piercing bow, as described in Section 4.4.5, to promote flow separation. The last step was the attachment of the 3D printed waterjet tunnel section onto the hull as described in more detail in Appendix B.

Appendix B

Model Waterjet Propulsion System

As defined by ITTC (2011c) the intake and nozzle geometry need to be scaled geometrically to ensure similar flow conditions at the intake and the nozzle as would occur on the full scale ship. A pump of convenience or a stock waterjet can be used to deliver the required flow rate and the position of the pump need not to be identical to that of the prototype waterjet system, as long as the kinematic similarity of the flow at the intake (momentum flux station 1 and 2) and in the nozzle area (momentum flux station 6 and 7) is ensured. Since there was no off the shelf stock waterjet or applicable pump available, the model waterjet used for testing consisted of a geometrically scaled waterjet tunnel, based on drawings of the waterjet model LIPS LJ120E (supplied by the waterjet unit manufacturer Wärtsilä) and the addition of a scaled impeller and stator which allows the supply of the expected thrust.

Using previously published manufacturing methods for model waterjet units, such as by Rispin (2007), the manufacturing method for the production of the model waterjet units chosen was 3D prototyping (i.e. 3D printing). This manufacturing method allowed for the required tolerances and dimensional accuracies as well as the desired flexibility in part creation. To accommodate the scaled waterjet tunnel in 3D printers, considering a limited maximum working volume, the waterjet tunnel needed to be split into two parts, which were then connected using the flanges shown in Figure B.1, bolts as well as adhesive (i.e. epoxy, made from a class of synthetic thermosetting polymers) to create a watertight seal. As shown in Figure B.1, two different nozzles were printed: one which allowed the mounting of sensors at predefined positions as well as flush nozzles which were used for waterjet tests without any mounted sensors.

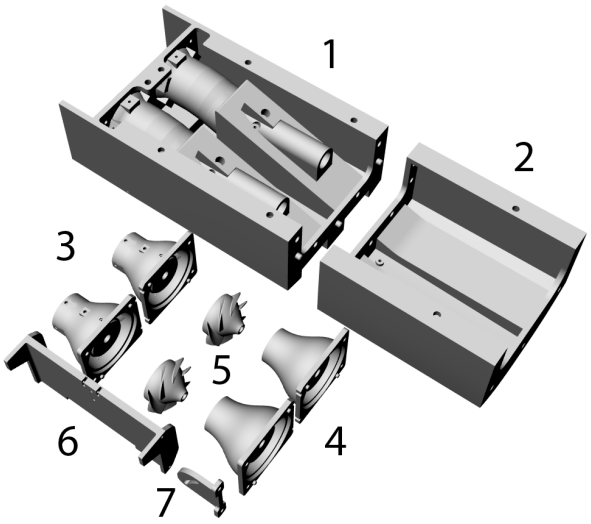

Figure B.1: 3D printed waterjet tunnels (1 and 2), impellers (5), nozzles (3 and 4), trim tab (6) and a centre piece (7), which allowed the adjustment of the trim tab to different angles.

The model waterjet was designed to use two brushless DC motors (Dunkermotoren BG-75x25 CI) and the completed propulsion assembly is shown in Figure B.2 where two dynamometers (Cussons, model R31-1; maximum torque 4 Nm and maximum thrust 100 N) were used for thrust and torque measurements.

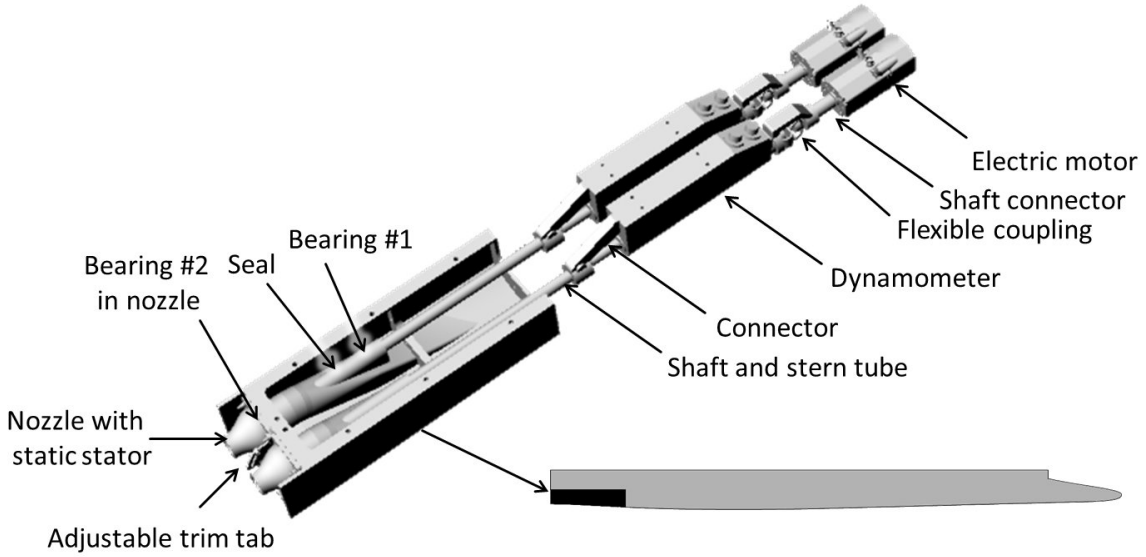

Figure B.2: Model waterjet propulsion system used for flow rate measurement and self-propulsion testing. Also shown is the position in the carbon fibre hull where the 3D printed waterjet tunnel is attached.

The parts list for the two model waterjet propulsion system consisted of:

- (2x) DC brushless electric motor (Dunkermotoren BG-75x25 CI)
- (2x) Custom manufactured shaft connector

- (2x) Flexible coupling (Dynamometer accessory)
- (2x) Dynamometer (Cussons Ship Model Self-Propulsion Dynamometer Type R31)
- (2x) Custom manufactured stern tube + shaft
- (2x) Oil seal
- (4x) Deep groove ball bearing (one before and one after the waterjet pump)
- (2x) Rapid prototype (3D printed) waterjet tunnel

As the material used for 3D printing ended up being white, the parts were painted yellow (after fairing the waterjet tunnel assembly to the hull) the same colour as the hull and a stern view of the finished hull is presented in Figure B.3 and Figure B.4.

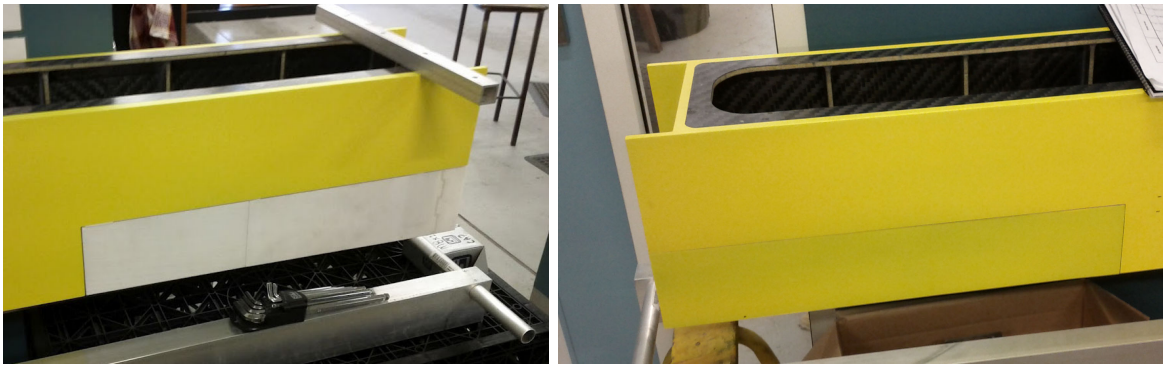

Figure B.3: 3D printed waterjet tunnel attached to the carbon fibre demihull model. The left picture shows the waterjet tunnel attached for the first time to check fit and surface and the picture on the right shows the waterjet tunnel faired into the hull and painted the same colour as the model hull.

Figure B.4: Stern view of model demihull showing the model waterjet propulsion system, waterjet inlets, trim tab, and Kiel Probes used for reference measurements. The vertical markers at the stern were used to visualise the transom immersion depths.

Appendix C

Schematic Test Layouts

This content of this appendix describes the experimental test setup of the static flow rate measurement test, and waterjet self-propulsion test, data acquisition system using schematic layouts of the experimental setups. These schematics are intended as general test overviews and were used for setting up the experimental testing in the experimental test facilities. Abbreviations used in the schematic layouts are: Data acquisition system (DAQ), differential pressure transducer (DPT), Kiel probe (KP), linear variable differential transformer (LVDT), and pitot-static tube (PST).

Flow Rate Measurement Test

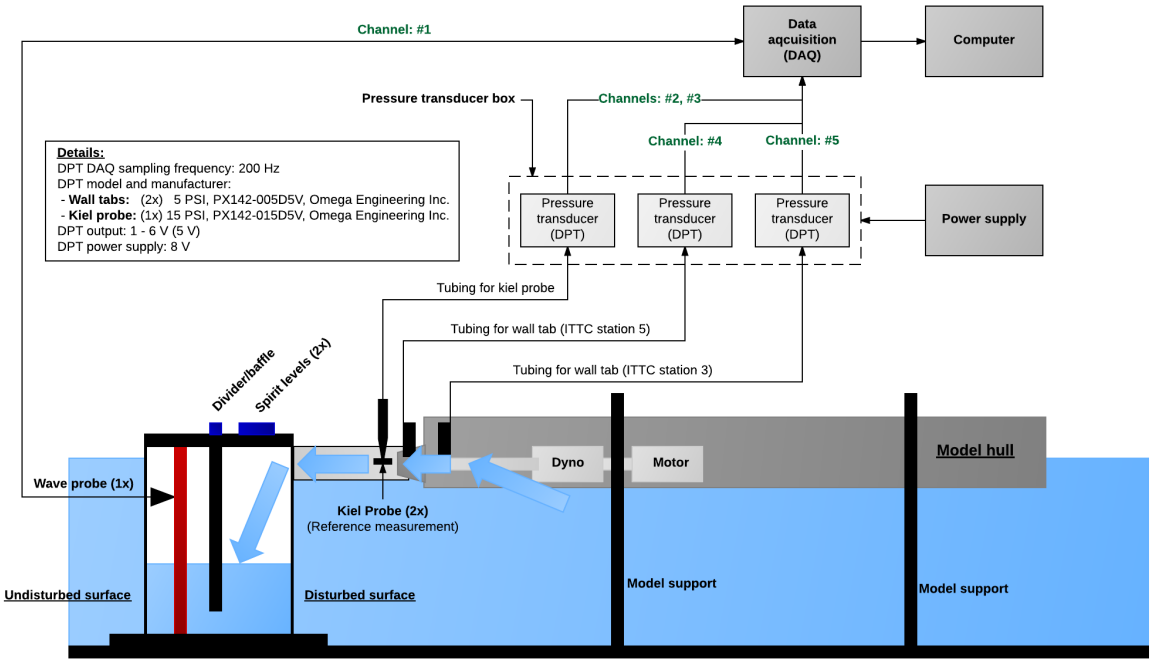

Figure C.1: General schematic layout of static flow rate measurement test carried out in AMC model test basin.

Flow Rate Measurement Test

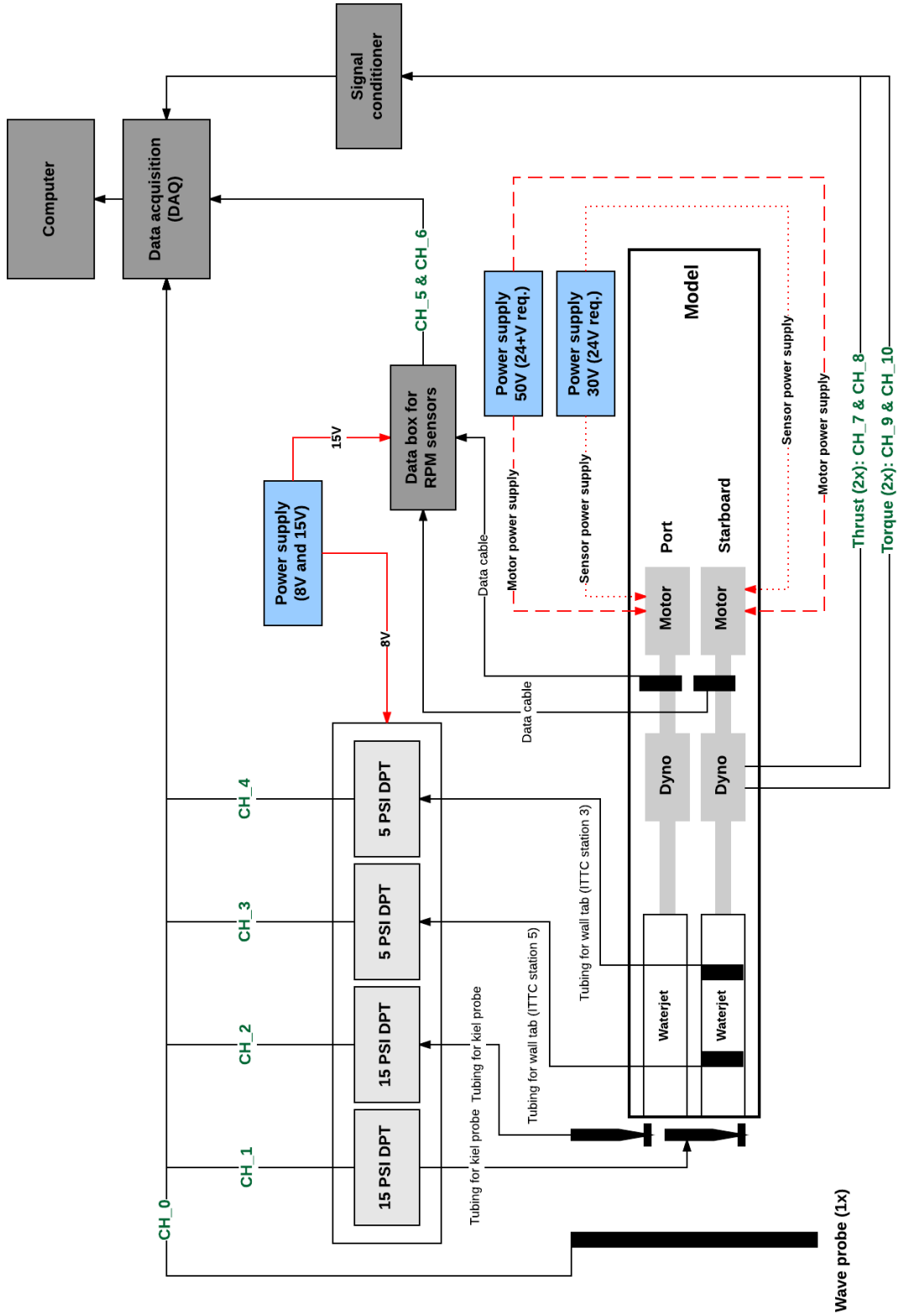

Figure C.2: Data acquisition system layout of static flow rate measurement test carried out in AMC model test basin.

Waterjet Self-Propulsion Test

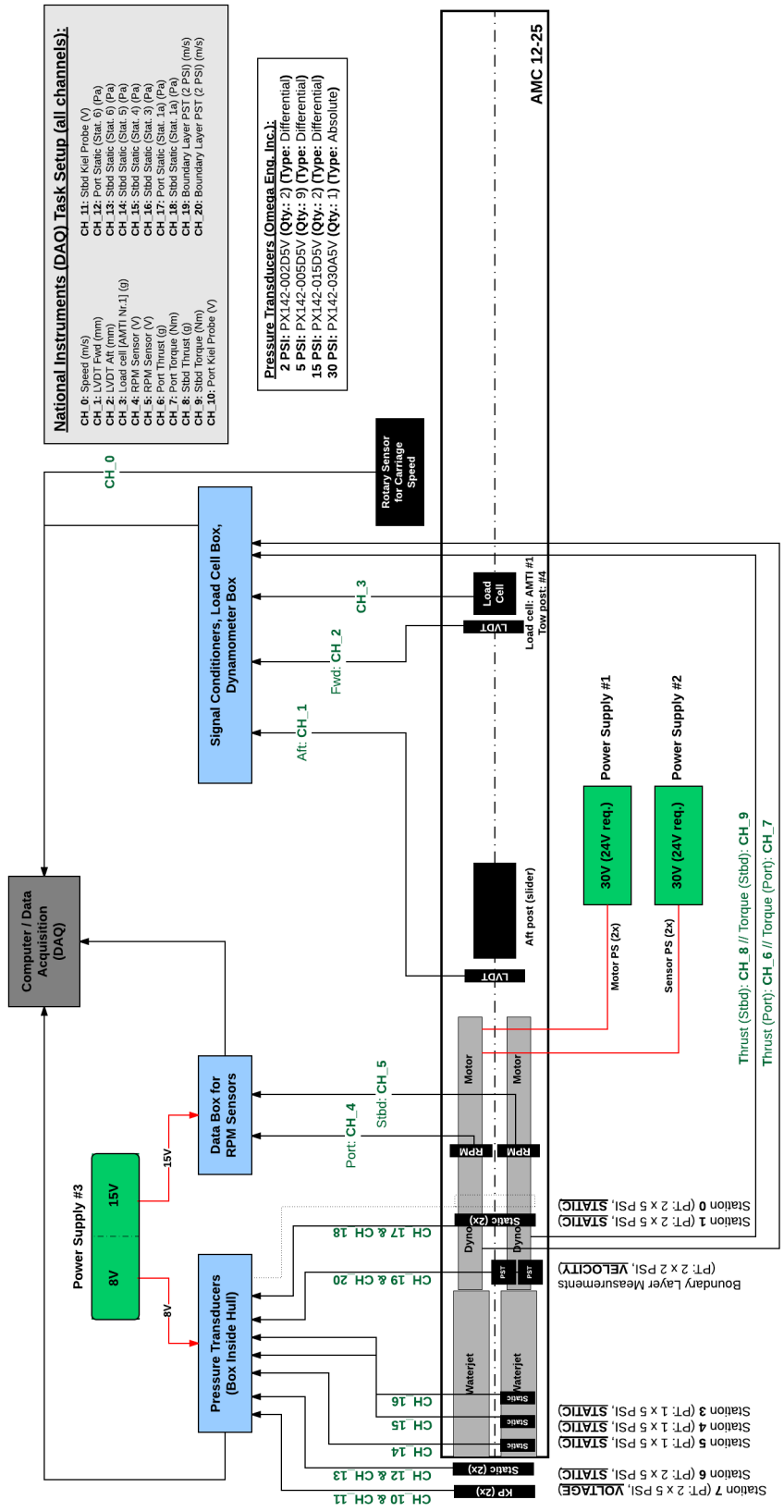

Figure C.3: Data acquisition system layout of static flow rate measurement test carried out in AMC towing tank.

Appendix D

Uncertainty Analysis

Uncertainty analysis is important to establish a baseline of confidence for any data set and for the presented work it was used to establish accuracy of resistance, flow rate, and self-propulsion test results. A standard deviation based method was used to establish baseline errors for these tests and for this many testing runs in all experimental tests were repeated at least three times to determine repeatability. Resistance and waterjet self-propulsion uncertainty analysis were based on ITTC recommended procedures and uncertainty analysis for flow rates was based on the 95% confidence, large-sample approach for assessing random uncertainty, as recommended by the American Society of Mechanical Engineers (ASME PTC 19.1-2005).

The main aim of an uncertainty analysis is to give a quantitative answer as to how reliable a measured or calculated value is. Uncertainty is the statistical representation of error and the word error is used to show the difference between a measured result and the true value. Uncertainties are generally quantified in terms of confidence intervals. For example a confidence interval of 2σ (where σ is standard deviation) means that 95% of all readings of a particular measurement will be within 2σ from the true value. This also means that the probability that the true value will be within the confidence interval is 0.95.

Two types of errors are considered when carrying out an uncertainty analysis: bias (β) and precision errors (ε) shown in Figure D.1 in relation to total error (δ). Bias errors are systematic errors which are not revealed by repetition of the experiments, while precision errors (i.e. random errors) are the scatter in the results which is found by comparing the results of repeated measurements. Bias errors cannot be measured but have to be estimated based on qualified assumptions, where calibrations are the key to reducing errors.

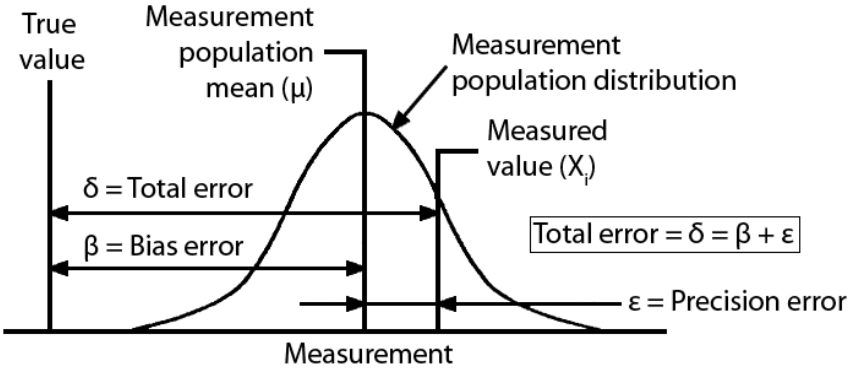

Figure D.1: Total measurement error based on bias (systematic) and precision (random) errors.

A basic uncertainty consists of the following parts where, based on recommendations by Lin (1990) and van Terwisga (1996), results of steps 4, 5, and 6 should be declared separately:

1. Identification of all error sources.
2. Determination of the individual precision (statistically) and bias (based on best possible estimates) errors for each source identified in step 1.
3. Determination of sensitivities of each error source (from step 2) to the end result.
4. Creation of total precision uncertainty intervals from step 2 and step 3.
5. Creation of total bias uncertainty intervals from step 2 and step 3.
6. Combination of total precision and bias uncertainty intervals from step 4 and step 5.

Accuracy of measurements can be increased by:

- Improving calibration procedures by carrying out calibrations more careful and include more of the test setup in the calibration.
- Acquiring more accurate, sensitive transducers to improve accuracy of measurements.
- Redesigning test setup by refining measurement setup for better accuracy, use of a larger model to decrease scaling errors, or more accurate manufacture of model.
- Improving test execution by using longer waiting times between runs (important for calm water testing).
- Increasing number of repeated runs. This will increase total number of runs which is time consuming and expensive but at the same time would increase accuracy.

The following three sections describe the methodology and theory used for bare-hull resistance, flow rate measurement, and waterjet self-propulsion test uncertainty analysis and results are presented in Section 4.4.10 for bare-hull resistance test, Section 4.5.5 for static flow rate measurement test, and Section 4.6.11 for waterjet self-propulsion test.

D.1 Bare-hull Resistance Test

The uncertainty analysis carried out for model scale bare-hull resistance test results was based on ITTC guidelines for uncertainty analysis in resistance towing tank tests as defined in ITTC (2008). For resistance uncertainty analysis, the test system can be grouped into five groups as shown in Figure D.2, and each group is related to one to a set uncertainty sources. The uncertainty analysis presented here is limited to resistance measurements (i.e. direct measurement uncertainty).

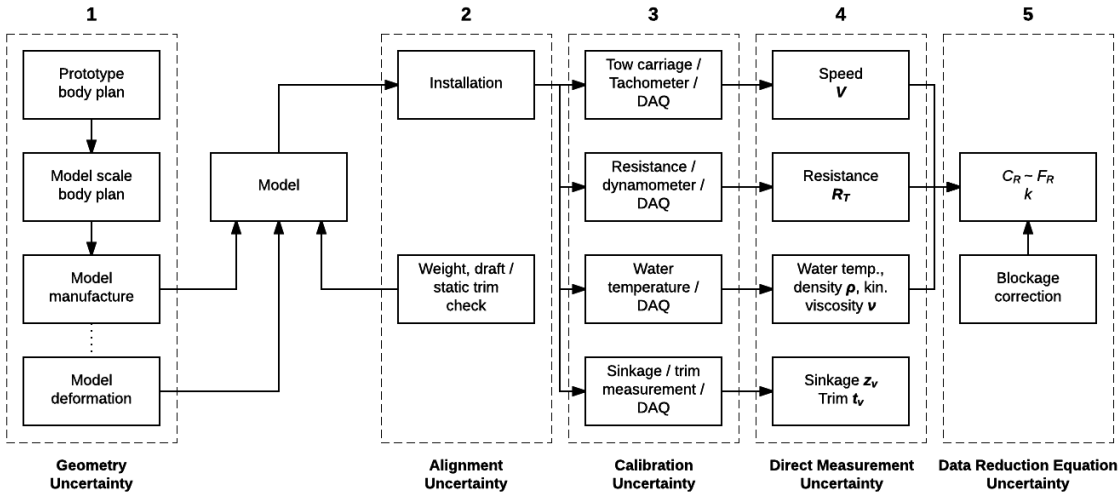

Figure D.2: Schematic layout of bare-hull resistance measurement system showing geometry, alignment, calibration, direct measurement, and data reduction equation uncertainty groups.

Errors are the difference between the measured value and the true value (error = measured value-true value) while uncertainty is the statistical representation of error (i.e. the expected error of a measurement). The confidence interval used for the resistance uncertainty analysis is 95%, which means that 95% of all readings of a measurement will be within 2 standard deviations (σ) from the true value. Included in the uncertainty analysis are precision errors which are the scatter in the experimental results from repeated measurements and bias errors which as systematic errors not found from repeated measurements.

Possible bias error sources for resistance uncertainty analysis are:

- Scale effects such as Reynolds effects, cavitation (important for foils and propulsors), surface tension and spray, and air pressure ratio.

- Model inaccuracies such as inaccurate draft/ballasting, rough model surface, inaccurate shape, or model deformations.
- Test setup errors such as influence of model connections (i.e. model not aligned correctly, towing position too high in model, load cell not measuring forces exactly on the horizontal direction), uncertainty of calibrations, and systematic errors in measurements systems.
- Calibration errors.
- Errors based on environmental modelling such as temperature layers in the water.
- Tank wall effects such as blockage which influences steady velocity and pressure around a forward moving model and wave reflections (i.e. reflected waves from imperfect wave damping devices and reflected waves from tank walls).

The purpose of the bare-hull resistance test is to measure data at a range of length Froude numbers for the temperature corrected, at 15°C, resistance coefficient (C_{T15}). As discussed in Section 4.4, the measurement system consists of a rotary sensor to measure carriage speed, two Linear Variable Differential Transformers (LVDTs) to measure forward and aft sinkage (i.e. heave and running trim calculations), and a load to measure drag. The main resistance data reduction equation is given by Equation D.1, where C_T is the measured total resistance coefficient measured during the model test and is the preferred variable.

$$C_{T15C} = C_T - (C_F - C_{F15C})(1 + k) \tag{D.1}$$

C_{F15C} and C_F are frictional resistance coefficients at 15°C and measured tank temperature respectively and k is the form factor. Total resistance coefficient (C_T) is calculated using Equation D.2, where $M_x g$ is the force in the axial direction calibrated for model inclination in Newtons, ρ is the towing tank water density determined using measured towing tank temperature, V is towing carriage speed (i.e. model speed), and S is the wetted surface area.

$$C_T = \frac{M_x g}{\frac{1}{2}\rho S V^2} \tag{D.2}$$

Resistance coefficient (C_{T15}) is the preferred results as it calibrates all the results to the same temperature and the temperature of 15°C is recommended by ITTC 1978 as a standard to enable comparisons of tests at different testing facilities. Frictional resistance coefficient (C_F) is calculated, as recommended by ITTC 1978, using the flat plate friction line:

$$C_F = \frac{0.075}{(log_{10} R_n - 2)^2} \tag{D.3}$$

where Reynolds number $Re = VL_{WL}/\nu$ and Prohaska's method as described in ITTC (1996) as shown in Equation D.4, where only low length Froude number resistance data ($0.1 \leq \mathrm{F_r} \leq 0.2$) are used to determine k and m is the slope of a curve fit through the used subset of data.

$$\frac{C_T}{C_F} = m\frac{F_r^4}{C_F} + (1+k) \tag{D.4}$$

For the resistance uncertainty analysis presented here the form factor (k) was established using Prohaska's method discussed in Lindgren et al. (1978) and ITTC (2011b) and the use and results of Prohaska's method are provided in Section 4.4.4. A form factor (1+k) of 1.1 will be used here when using ITTC 1957 friction line shown in Equation D.3.

The need for the density (ρ) and kinematic viscosity (ν) on temperature (T) was accounted for by measurement of the towing tank water temperature and using tables provided by the 2011 ITTC fresh and sea water properties guideline 7.5-02-01-03. The measurement system for water temperature was daily thermometer readings of at about mid draft of the model. End to end calibration was used for the resistance test before and after data recoding. The load cell and signal conditioner were statically calibrated to determine voltage to mass relationship in the form of a calibration factor.

A resistance analysis was carried out for a length Froude number range of 0.2 to 0.5. The basis of the analysis is conversion of the resistance data reduction equation (Equation D.1) to functional form:

$$C_{T15C} = C_{T15C}\left(M_x, \rho(T), V, S, C_F, C_{F15C}, k\right) \tag{D.5}$$

and the expression of the uncertainty analysis Equation D.6, Equation D.7, and Equation D.14, where the sensitivity coefficients (θ_i) are evaluated analytically with derivatives of Equations D.1 to D.4, where B represents bias (systematic) errors and P represents precision (random) errors.

$$U_{C_{T15C}} = \sqrt{\left(B_{C_{T15C}}\right)^2 + \left(P_{C_{T15C}}\right)^2} \tag{D.6}$$

$$B_{C_{T15C}} = \sqrt{\left(\theta_S B_S\right)^2 + \left(\theta_V B_V\right)^2 + \left(\theta_{M_x} B_{M_x}\right)^2 + \left(\theta_\rho \left(B_\rho + \theta_{\rho tw} B_{tw}\right)\right)} \tag{D.7}$$

Breakdown of components required for total C_T bias at 15°C calculated using Equation D.7:

- θ_S, θ_V, θ_{M_x}, θ_ρ, and $\theta_{\rho_{tw}}$ are wetted surface (S), speed (V), total mass resistance (M_x), water density (ρ), and water temperature (ρ_{tw}) sensitivity coefficients (Equation D.8 to Equation D.12).
- B_S is wetted surface bias $B_S = \sqrt{B_{S1}^2 + B_{S2}^2}$ where B_{S1} is assumed error in hull form based on 0.5% error in wetted surface area and B_{S2} is error in displacement based on 0.5% error in displacement.

- B_V is speed bias based on standard deviation of speed measured in resistance test.
- B_{M_x} is total resistance mass bias (see Equation D.13).
- B_ρ is water density bias.
- B_{tw} is water temperature bias.

Sensitivity coefficients for wetted surface (S), speed (V), total mass resistance (M_x), water density (ρ), and water temperature (ρ_{tw}) are calculated using:

$$\theta_S = \frac{\partial C_T}{\partial S} = \frac{M_x g}{\frac{1}{2}\rho V^2}\left(-\frac{1}{S^2}\right) \tag{D.8}$$

$$\theta_V = \frac{\partial C_T}{\partial V} = \frac{M_x g}{\frac{1}{2}\rho S}\left(-\frac{2}{V^3}\right) \tag{D.9}$$

$$\theta_{M_x} = \frac{\partial C_T}{\partial M_x} = \frac{g}{\frac{1}{2}\rho V^2 S} \tag{D.10}$$

$$\theta_\rho = \frac{\partial C_T}{\partial \rho} = \frac{M_x g}{\frac{1}{2}V^2 S}\left(-\frac{1}{\rho^2}\right) \tag{D.11}$$

$$\theta_{\rho tw} = \frac{\partial \rho}{\partial t_w}\left(t_w = 15°C\right) = \left|0.0638 - 0.0173 t_w + 0.0001897 t_w^2\right| \tag{D.12}$$

Total resistance mass bias (B_{Mx}), used in Equation D.7, can be broken down into uncorrelated elemental errors (i.e. B_{Mx1} = resistance calibration bias, B_{Mx2} = resistance curve fit bias, B_{Mx3} = resistance load cell misalignment bias, and B_{Mx4} = resistance towing force inclination bias) which are combined using Equation D.13, where the bias limits for all B_{Mx} elements are estimated for each measured variable using the best information available at the time of testing.

$$B_{M_x} = \sqrt{B_{M_{x1}}^2 + B_{M_{x2}}^2 + B_{M_{x3}}^2 + B_{M_{x4}}^2} \tag{D.13}$$

Precision limit of the average of M samples is calculated using Equation D.14, where K is coverage factor, using Gaussian distribution, for standard deviation (i.e. coverage factor 2 for confidence level of approx. 95% and coverage factor 3 for confidence level greater than 99%), σ_{CT} is standard deviation of C_T, and M is number of repeated runs for the same test.

$$P_{C_{T15C}} = \frac{K\sigma_{C_T}}{\sqrt{M}} \tag{D.14}$$

Tabulated summaries of results of resistance uncertainties for a length Froude number range of 0.2 to 0.48, two displacements (1,500t and 1,804t), and three static displacements for

each displacement are shown in Table D.1 and Table D.2. Tabulated summaries of results of resistance uncertainties for a length Froude number range of 0.1 to 0.2 using results of resistance measurements based on deep transom (at a static trim of approximately 3 degrees by bow) Prohaska runs are shown in Table D.3. Plotted total uncertainties in terms of total resistance coefficient (C_T) and length Froude number are shown in uncertainty analysis results presented in Section 4.4.10.

Table D.1: Summary Of Uncertainties For A Displacement Of 1,500t.

$\mathbf{F_r}$	$\boldsymbol{\theta_S B_S}$	$\boldsymbol{\theta_V B_V}$	$\boldsymbol{\theta_{Mx} B_{Mx}}$	$\boldsymbol{\theta_\rho(B_\rho + \theta_{\rho tw} B_{tw})}$	$\mathbf{B_{CT}}$	$\mathbf{P_{CT}}$
-	-	-	-	-	-	-
Displacement: 1,500t; static trim: level (0 degrees)						
0.10	-3.16E-05	-7.00E-06	6.56E-04	-5.83E-06	6.57E-04	1.47E-04
0.12	-3.20E-05	-5.92E-06	4.57E-04	-5.91E-06	4.58E-04	9.23E-05
0.14	-3.06E-05	-4.80E-06	3.30E-04	-5.65E-06	3.31E-04	3.77E-05
0.16	-3.02E-05	-4.16E-06	2.54E-04	-5.57E-06	2.56E-04	3.71E-05
0.18	-3.04E-05	-3.72E-06	2.01E-04	-5.62E-06	2.03E-04	1.70E-05
0.20	-3.18E-05	-3.49E-06	1.61E-04	-5.87E-06	1.64E-04	1.79E-05
0.23	-3.40E-05	-3.26E-06	1.23E-04	-6.28E-06	1.28E-04	1.30E-05
0.26	-3.67E-05	-3.09E-06	9.49E-05	-6.77E-06	1.02E-04	4.45E-05
0.28	-3.65E-05	-2.86E-06	8.22E-05	-6.74E-06	9.03E-05	1.30E-05
0.29	-3.68E-05	-2.80E-06	7.72E-05	-6.80E-06	8.58E-05	2.83E-05
0.31	-3.75E-05	-2.66E-06	6.75E-05	-6.92E-06	7.76E-05	4.50E-05
0.32	-3.72E-05	-2.55E-06	6.31E-05	-6.86E-06	7.36E-05	7.78E-06
0.34	-3.56E-05	-2.30E-06	5.56E-05	-6.58E-06	6.64E-05	1.68E-06
0.35	-3.51E-05	-2.20E-06	5.27E-05	-6.48E-06	6.37E-05	1.58E-05
0.37	-3.43E-05	-2.04E-06	4.72E-05	-6.33E-06	5.87E-05	1.47E-05
0.38	-3.45E-05	-1.99E-06	4.46E-05	-6.36E-06	5.68E-05	2.18E-05
0.39	-3.48E-05	-1.96E-06	4.22E-05	-6.43E-06	5.51E-05	6.05E-06
0.40	-3.53E-05	-1.93E-06	4.01E-05	-6.52E-06	5.39E-05	1.67E-05
0.41	-3.52E-05	-1.89E-06	3.83E-05	-6.50E-06	5.25E-05	2.42E-05
0.43	-3.53E-05	-1.80E-06	3.48E-05	-6.52E-06	5.00E-05	1.88E-05
0.44	-3.49E-05	-1.74E-06	3.32E-05	-6.44E-06	4.86E-05	5.55E-06
0.47	-3.44E-05	-1.60E-06	2.91E-05	-6.35E-06	4.55E-05	6.39E-06
Displacement: 1,500t; static trim: -0.5 degrees by bow						
0.23	-3.23E-05	-3.10E-06	1.25E-04	-5.97E-06	1.29E-04	2.52E-05
0.29	-3.38E-05	-2.57E-06	7.82E-05	-6.24E-06	8.54E-05	7.14E-06
0.35	-3.10E-05	-1.95E-06	5.35E-05	-5.73E-06	6.21E-05	1.66E-05
0.41	-3.30E-05	-1.76E-06	3.89E-05	-6.08E-06	5.13E-05	3.71E-05
0.47	-3.33E-05	-1.56E-06	2.96E-05	-6.15E-06	4.50E-05	1.05E-05
Displacement: 1,500t; static trim: 0.5 degrees by stern						
0.23	-3.50E-05	-3.36E-06	1.22E-04	-6.46E-06	1.27E-04	1.25E-05
0.29	-3.83E-05	-2.90E-06	7.60E-05	-7.06E-06	8.54E-05	1.45E-05
0.35	-3.68E-05	-2.31E-06	5.19E-05	-6.79E-06	6.40E-05	8.99E-06
0.42	-3.70E-05	-1.98E-06	3.78E-05	-6.82E-06	5.33E-05	2.65E-05
0.48	-3.53E-05	-1.65E-06	2.87E-05	-6.52E-06	4.60E-05	5.67E-06

Table D.2: Summary Of Uncertainties For A Displacement Of 1,804t.

$\mathbf{F_r}$	$\boldsymbol{\theta_S B_S}$	$\boldsymbol{\theta_V B_V}$	$\boldsymbol{\theta_{Mx} B_{Mx}}$	$\boldsymbol{\theta_\rho(B_\rho + \theta_{\rho tw} B_{tw})}$	$\mathbf{B_{CT}}$	$\mathbf{P_{CT}}$
-	-	-	-	-	-	-
Displacement: 1,804t; static trim: level (0 degrees)						
0.20	-3.27E-05	-3.59E-06	1.44E-04	-6.04E-06	1.48E-04	5.55E-05
0.23	-3.53E-05	-3.39E-06	1.10E-04	-6.52E-06	1.16E-04	2.35E-05
0.26	-3.81E-05	-3.21E-06	8.49E-05	-7.03E-06	9.34E-05	2.82E-05
0.29	-3.80E-05	-2.88E-06	6.88E-05	-7.01E-06	7.90E-05	2.37E-05
0.32	-4.03E-05	-2.77E-06	5.64E-05	-7.43E-06	6.97E-05	3.01E-05
0.35	-3.81E-05	-2.39E-06	4.70E-05	-7.04E-06	6.10E-05	2.70E-05
0.39	-3.73E-05	-2.15E-06	3.98E-05	-6.88E-06	5.50E-05	6.13E-05
0.42	-3.97E-05	-2.12E-06	3.42E-05	-7.33E-06	5.29E-05	9.78E-05
0.45	-4.02E-05	-2.00E-06	2.96E-05	-7.43E-06	5.06E-05	3.10E-05
0.48	-3.97E-05	-1.85E-06	2.60E-05	-7.34E-06	4.81E-05	5.69E-05
Displacement: 1,804t; static trim: -0.5 degrees by bow						
0.23	-3.27E-05	-3.13E-06	1.11E-04	-6.03E-06	1.16E-04	2.25E-05
0.29	-3.54E-05	-2.69E-06	6.97E-05	-6.54E-06	7.85E-05	4.71E-06
0.35	-3.46E-05	-2.17E-06	4.76E-05	-6.39E-06	5.92E-05	1.16E-05
0.41	-3.77E-05	-2.02E-06	3.47E-05	-6.96E-06	5.17E-05	1.67E-05
0.47	-3.82E-05	-1.78E-06	2.63E-05	-7.05E-06	4.69E-05	3.64E-05
Displacement: 1,804t; static trim: 0.5 degrees by stern						
0.23	-3.83E-05	-3.68E-06	1.09E-04	-7.07E-06	1.16E-04	4.47E-05
0.30	-4.08E-05	-3.09E-06	6.80E-05	-7.53E-06	7.97E-05	2.39E-05
0.36	-4.03E-05	-2.53E-06	4.64E-05	-7.45E-06	6.20E-05	6.06E-05
0.42	-4.29E-05	-2.30E-06	3.39E-05	-7.92E-06	5.53E-05	5.09E-06
0.48	-4.19E-05	-1.96E-06	2.57E-05	-7.74E-06	4.98E-05	4.70E-05

Table D.3: Summary Of Uncertainties For A Displacement Of 1,500t (Deep Transom Prohaska Runs).

$\mathbf{F_r}$	$\boldsymbol{\theta_S B_S}$	$\boldsymbol{\theta_V B_V}$	$\boldsymbol{\theta_{Mx} B_{Mx}}$	$\boldsymbol{\theta_\rho(B_\rho + \theta_{\rho tw} B_{tw})}$	$\mathbf{B_{CT}}$	$\mathbf{P_{CT}}$
-	-	-	-	-	-	-
0.11	-2.50E-05	-5.55E-06	6.66E-04	-4.61E-06	6.66E-04	1.65E-04
0.13	-2.36E-05	-4.36E-06	4.61E-04	-4.35E-06	4.62E-04	1.63E-04
0.15	-2.24E-05	-3.52E-06	3.32E-04	-4.13E-06	3.33E-04	2.81E-05
0.17	-2.22E-05	-3.06E-06	2.56E-04	-4.10E-06	2.57E-04	4.13E-05
0.19	-2.19E-05	-2.68E-06	2.02E-04	-4.04E-06	2.03E-04	9.74E-05
0.21	-2.21E-05	-2.42E-06	1.62E-04	-4.08E-06	1.64E-04	0.00E+00
0.22	-2.22E-05	-2.43E-06	1.62E-04	-4.09E-06	1.63E-04	6.42E-05

D.2 Flow Rate Measurement Test

Description and results of flow rate measurement uncertainty analysis based on the 95% confidence, large-sample approach for assessing random uncertainty, as recommended by the American Society of Mechanical Engineers (ASME PTC 19.1-2005). Using this method, total uncertainty in a measurement is based on the combination of uncertainty due to precision (random) error and uncertainty due to bias (systematic) error. The combined standard uncertainty, as described by ASME (2005), of the measured mean (μ), which is the total uncertainty at the standard deviation (σ) level, is calculated as shown in Equation D.15, where $b_{\bar{x}}$ is the standard systematic uncertainty, and $s_{\bar{x}}$ is the standard random uncertainty of the mean.

$$u_{\bar{x}} = \sqrt{(b_{\bar{x}})^2 + (s_{\bar{x}})^2} \tag{D.15}$$

As the main variable of the flow rate measurement test is the mass flow rate, Equation D.15 can be changed to Equation D.16, where $C_{\dot{m}}$ is a non-dimensional form of mass flow rate ($\dot{m}$), B represents bias (systematic) errors and P represents precision (random) errors.

$$U_{C_{\dot{m}}} = \sqrt{(B_{C_{\dot{m}}})^2 + (P_{C_{\dot{m}}})^2} \tag{D.16}$$

The non-dimensional mass flow rate was calculated using Equation D.17, where Q_J is measured volumetric flow rate, ρ is water density, D is nozzle diameter, and n is shaft speed per second (RPS).

$$C_{\dot{m}} = \frac{Q_J \rho}{\rho n^2 D^3} = \frac{Q_J}{n^2 D^3} \tag{D.17}$$

The bias errors are then broken down into individual components so that the total $C_{\dot{m}}$ bias as shown in Equation D.18.

$$B_{C_{\dot{m}}} = \sqrt{(\theta_{Q_J} B_{Q_J})^2 + (\theta_D B_D)^2 + (\theta_n B_n)^2} \tag{D.18}$$

Breakdown of components required for total $C_{\dot{m}}$ bias calculated using Equation D.18:

- θ_{QJ}, θ_D, and θ_n are volumetric flow rate (Q_J), nozzle diameter (D), and shaft speed per second (n) sensitivity coefficients (Equation D.19 to Equation D.21).
- B_{QJ} is volumetric flow rate bias based on standard deviation of flow rate measured in flow rate measurement test.
- B_D is nozzle diameter bias.
- B_n is shaft speed bias.

Sensitivity coefficients for volumetric flow rate (Q_J), nozzle diameter (D), and shaft speed per second (n) are calculated using:

$$\theta_{Q_J} = \frac{\partial C_{\dot{m}}}{\partial Q_J} = \frac{\rho}{\rho n^2 D^3} = \frac{1}{n^2 D^3} \tag{D.19}$$

$$\theta_D = \frac{\partial C_{\dot{m}}}{\partial D} = \frac{Q_J \rho}{\rho n^2}\left(-\frac{3}{D^4}\right) = \frac{Q_J}{n^2}\left(-\frac{3}{D^4}\right) \tag{D.20}$$

$$\theta_n = \frac{\partial C_{\dot{m}}}{\partial n} = \frac{Q_J \rho}{\rho D^3}\left(-\frac{2}{n^3}\right) = \frac{Q_J}{D^3}\left(-\frac{2}{n^3}\right) \tag{D.21}$$

Total volumetric flow rate bias (B_{QJ}), used in Equation D.18, can be broken down into uncorrelated elemental errors (i.e. B_{QJ1} = volumetric flow rate calibration bias, and B_{QJ2} = volumetric flow rate curve fit bias) which are combined using Equation D.22, where the bias limits for all B_{QJ} elements are estimated for each measured variable using the best information available at the time of testing.

$$B_{Q_J} = \sqrt{B_{Q_{J1}}^2 + B_{Q_{J2}}^2} \tag{D.22}$$

Precision limit of the average of M samples is calculated using Equation D.23, where K is coverage factor, using Gaussian distribution, for standard deviation (coverage factor $K = 2$ for confidence level of approx. 95% and coverage factor $K = 3$ for confidence level greater than 99%), $\sigma_{C_{\dot{m}}}$ is standard deviation of $C_{\dot{m}}$, and M is number of repeated runs for the same test.

$$P_{C_{\dot{m}}} = \frac{K\sigma_{C_{\dot{m}}}}{\sqrt{M}} \tag{D.23}$$

Tabulated summaries of mass flow rate uncertainties for port and starboard waterjet propulsion systems are shown in Table D.4, where θ_i are individual sensitivities, B_i are individual bias values, $B_{C_{\dot{m}}}$ is total bias, $P_{C_{\dot{m}}}$ is total precision error, and $U_{C_{\dot{m}}}$ is total uncertainty in terms of mass flow rate. Plotted total uncertainties in terms of mass flow rate coefficient ($C_{\dot{m}}$) and shaft speed (N) are shown in uncertainty analysis results presented in Section 4.5.5.

Table D.4: Summary Of Mass Flow Uncertainties For Port And Starboard Waterjet Propulsion Systems For Shaft Speed Range Of 1,000 To 3,400 RPM, Where θ_i Are Individual Sensitivities, B_i Are Individual Bias Values, $B_{C_{\dot{m}}}$ Is Total Bias, $P_{C_{\dot{m}}}$ Is Total Precision Error, And $U_{C_{\dot{m}}}$ Is Total Uncertainty.

Shaft speed	$B_{C_{\dot{m}}}$	$P_{C_{\dot{m}}}$	$U_{C_{\dot{m}}}$	**% of** $C_{\dot{m}}$
RPM	-	-	-	-
Port waterjet propulsion system				
1,000	0.0940	0.0028	0.0941	4.10
1,400	0.0833	0.0043	0.0835	2.56
1,800	0.0924	0.0048	0.0925	2.17
2,200	0.1061	0.0057	0.1062	2.01
2,600	0.1259	0.0018	0.1259	1.99
3,000	0.1489	0.0018	0.1490	1.96
3,400	0.1737	0.0146	0.1744	1.93
Starboard waterjet propulsion system				
1,000	0.0964	0	0.0964	4.10
1,400	0.0851	0	0.0851	2.56
1,800	0.0942	0.0182	0.0960	2.20
2,200	0.1090	0	0.1090	2.01
2,600	0.1313	0	0.1313	1.99
3,000	0.1597	0.0105	0.1600	1.97
3,400	0.1914	0.0182	0.1923	1.93

D.3 Waterjet Self-Propulsion Test

The uncertainty analysis carried out for model scale self-propulsion test results was based on ITTC guidelines for uncertainty analysis in waterjet self-propulsion tests as defined in ITTC (2011f). Experimental errors sources for waterjet propulsion are shown in Table D.5 which shows measurements systems and measurement of individual variables.

Table D.5: Experimental Error Sources For Waterjet Propulsion Used For Uncertainty Analysis.

Measurement system	**Variables**
Towing force	F_D
Waterjet geometry	D_N, w_{1A}
Intake velocity distribution	$u_{x1A}(y, z)$
Sinkage	Z_6
Speed	U_0
Flow rate pressure difference	Δp
Temperature and density	T, ρ

Bias limits of the input parameters are reduced into the bias limits for the results by using the following data reduction equations; Equation D.24 for flow rate, Equation D.25 for change

in momentum flux, and Equation D.26 for effective jet system power.

$$Q_J = \sqrt{\frac{\langle T_{Jx} \rangle \, A_N}{\rho \, c_{m6} \, cos\theta_N}} \tag{D.24}$$

$$\Delta \overline{M}_x = T_{Jx} - c_{m1} U_0 \sqrt{\frac{T_{Jx} \rho A_N}{cos\theta_N}} \tag{D.25}$$

$$P_{JSE} = \sqrt{\frac{\langle T_{Jx} \rangle \, A_N}{\rho \, c_{m6} \, cos\theta_N}} \left(\frac{\langle T_{Jx} \rangle}{2\rho A_N cos\theta_N} - \frac{1}{2} c_{e1}^2 \, (1 - C_p) \, U_0^2 - g z_6 \right) \tag{D.26}$$

The uncertainty interval ($\pm U_i$) of the measured value X_i, is the error band in which the researcher is 95% confident the true value of the variable lies and 95% uncertainty is in Equation D.27 where B are bias (systematic) errors and P are precision (random) errors.

$$U_i = \sqrt{B_i^2 + P_i^2} \tag{D.27}$$

Non-dimensional sensitivity relates the non-dimensional error in the result ($\theta_i^{'}$) to the non-dimensional error in the source parameter ($b_R^{'}$) using Equation D.28.

$$b_R^{'} = \sqrt{\sum_{i=1}^{k} (\theta'_i b'_i)} \tag{D.28}$$

Non-dimensional bias error ($b_i^{'}$) is defined by:

$$b_i^{'} = \frac{S_i}{X_i} \tag{D.29}$$

Non-dimensional sensitivity ($\theta_i^{'}$) is defined by:

$$\theta_i^{'} = \frac{\partial R}{\partial X_i} \frac{\overline{X_i}}{\overline{R}} \tag{D.30}$$

Similar results can be found for the non-dimensional precision error ($p_i^{'}$). Normalising the error contribution yields the advantage that all sensitivities and error contributions can be immediately compared for their relevance in the final result.

Elemental bias errors $(B_i)_k$ have to be estimated for each variable X_i using the best information available at the time of testing. Estimates are based best on manufacturers specifications, analytical estimates and results of previous experiments. Estimates for the bias errors were based on the results of the flow rate and self-propulsion test. Additional bias errors are based on not measuring directly the variable stated in the date reduction equation. An example for such an error is the assumption that the vena contracta of the jet coincides with the nozzle

discharge opening; that is momentum flux station 6 instead of station 7 is used to determine momentum and energy fluxes.

For multiple tests (i.e. repeated runs of the same test) the precision limit can be calculated using Equation D.31, where M is the number of repeated runs for which the precision limit is to be calculated, σ is the sample standard deviation, and K is the coverage factor which depends on the distribution of the error. For a Gaussian distribution of the error and a large sample $K = 2$ is used for a confidence level of 95% and $K = 3$ is used for a confidence level of more than 99%.

$$P = \frac{K\sigma}{\sqrt{M}} \tag{D.31}$$

As jet thrust (T_{Jx}) cannot be measured directly, thrust was determined from a differential pressure transducer attached to a Kiel probe (see Section 4.5.1) that was calibrated during a separate static flow measurement test. It was assumed that the relation between jet thrust from the nozzle and pressure reading was the same during calibration in the flow rate measurement test and during the self-propulsion test.

The best estimate for jet thrust is then given by Equation D.32 where the calibrated jet thrust (T_{JxCal}) is obtained from Equation D.33 and where ai denotes the calibration coefficients.

$$\langle T_{Jx} \rangle = T_{JxCal} \frac{T_{Jx}}{T_{JxCal}} \tag{D.32}$$

$$T_{JxCal} = a_0 + a_1 \Delta p \tag{D.33}$$

Bias error, precision error, and non-dimensional sensitivity are estimated for each variable, and the 95% confidence interval $URSS$@95% is then calculated using Equation D.27. Plotted total uncertainties using 95% probability interval for eight speeds are shown in uncertainty analysis results presented in Section 4.6.11.

References/Bibliography

Allison, J. (1993). "Marine Waterjet Propulsion". In: *Society of Naval Architects and Marine Engineers (SNAME) Transactions* 101, pp. 275–335.

Allison, J. (2001). "Research in Waterjet Inlet, Hull and Jet Interactions". In: *International Conference Waterjet Propulsion III. The Royal Institute of Naval Architects (RINA). Gothenburg, Sweden.*

ASME (2005). *Test Uncertainty*. Code/standard PTC 19.1-2005. Three Park Avenue, New York, NY 10016-5990: The American Society of Mechanical Engineers (ASME).

Bose, N. (2008). *Marine Powering Prediction and Propulsors*. Jersey City, N.J: Society of Naval Architects and Marine Engineers.

Bowden, B. S. and Davidson, N. J. (1974). *Resistance Increments Due to Hull Roughness Associated With Form Factor Extrapolation Methods*. Ship Technical Manual 3800. National Physical Laboratory (NPL).

Bulten, N. W. H. (2006). "Numerical Analysis of a Waterjet Propulsion System". PhD Thesis. Technische Universiteit Eindhoven.

Campana, E., Gorski, J., Chun, H., Day, A., Huang, D., Macfarlane, G., Mikkola, T., Tahara, Y., and Valle, J. (2008). "Final Report and Recommendations to the 25th ITTC". In: *Resistance Committee*. Vol. 1. International Towing Tank Committee (ITTC), pp. 21–81.

Chakrabarti, S. (1998). "Physical Model Testing of Floating Offshore Structures". In: *Dynamic Positioning Conference*. Houston, Texas, USA.

Chesnakas, C. (2001). "3-D LDV Mapping of The Flow About a Waterjet-Powered Hull in a Tow Tank". In: *26th American Towing Tank Conference (ATTC)*.

Coop, H. G. (1995). "Investigation of hull-waterjet interaction effects". PhD Thesis. Department of Mechanical Engineering, University of Canterbury, Christchurch. NeŽealand.

Dang, J., Liu, R., and Pouw, C. (2013). "Waterjet System Performance and Cavitation Test Procedures". In: *SMP13 - Third International Symposium on Marine Propulsion, Tasmania, Australia*, pp. 87–96.

Delaney, K., Donnelly, M., Ebert, M., and Fry, D. (2009). "Use of RANS for Waterjet Analysis of a High-Speed Sealift Concept Vessel". In: *First International Symposium on Marine Propulsors (SMP'09)*. Trondheim, Norway: Naval Surface Warfare Center Carderock Division, West Bethesda, MD USA, pp. 395–408.

Duerr, P. and von Ellenrieder, K. D. (2014). "Scaling and Numerical Analysis of Nonuniform Waterjet Pump Inflows". In: *Oceanic Engineering, IEEE Journal of* PP.99, pp. 1–9.

Eslamdoost, A. (2012). "Investigation of waterjet/hull interaction effects". Thesis for Degree of Licentiate of Engineering. Chalmers University of Technology, Gothenburg, Sweden.

Eslamdoost, A. (2014). "The Hydrodynamics of Waterjet/Hull interactions". PhD Thesis. Chalmers University of Technology, Gothenburg, Sweden.

Fujisawa, N. (1995). "Measurements of Basic Performances for Waterjet Propulsion Systems in Water Tunnel". In: *International Journal of Rotating Machinery* 2.1, pp. 43–50.

Ghadimi, P., Shademani, R., and Fard, M. Y. (2013). "Performance Assessment of the Waterjet Propulsion System through a Combined Analytical and Numerical Approach". In: *International Journal of Physics* 1.2, pp. 22–27.

Griggs, D. and Woo, E. (2005). *HSV-2 SWIFT Combined Standardization and Powering Trials Results*. Report NSWCCD-50-TR-2005-013. Naval Surface Warfare Center, Carderock Division.

Grigson, C. W. B. (1989). "Note on an accurate turbulent velocity profile for use at ship scale". In: *Journal of Ship Research* 33, pp. 162–168.

Grigson, C. W. B. (1993). "An accurate smooth friction line for use in performance prediction". In: *Transactions of the Royal institution of Naval Architects* 135, pp. 149–162.

Grigson, C. W. B. (1995). "An improved method of predicting the performance of merchant ships from models". In: *Transactions of the Royal Institution of Naval Architects* 142, pp. 221–239.

Grigson, C. W. B. (2000). "A planar friction algorithm and its use in analysing hull resistance." In: *Transactions of the Royal Institution of Naval Architects* 142, pp. 76–115.

Haakenstad, K. (2012). "Analysis and correction of sea trials". Master Thesis. Norwegian University of Science, Technology (NTNU), Faculty of Engineering Science, and Technology, Department of Marine Technology.

Haase, M., Binns, J. R., Bose, N., Davidson, G., Thomas, G., and Friezer, S. (2014). "Hydrodynamic Hull Form Design Space Exploration of Large Medium-speed Catamarans using CFD". In: *International Journal of Maritime Engineering*.

Haase, M. (2015). "Energy-Efficient Large Medium-Speed Catamarans: Hull Form Design By Full-Scale CFD Simulations". PhD Thesis. University of Tasmania.

Harvald, S. A. (1991). *Resistance and propulsion of ships*. Ocean engineering (John Wiley & Sons). New York: Krieger Pub. Co., pp. 1–353.

Holtrop, J. (2001). "Extrapolation of Propulsion Tests for Ships with Appendages and Complex Propulsors". In: *Marine Technology* 38.3, pp. 145–157.

Hughes, A. W. and Turnock, S. R. (1997). *Computational fluid dynamic investigation of hull-waterjet flow interaction*. Ship Science Report 102. University of Southampton.

Hughes, G. and Allan, J. F. (1951). "Turbulence Stimulation On Ship Models". In: *SNAME Transactions* 59, pp. 281–314.

ITTC (1978). "Final Report and Recommendations to the 11th ITTC". In: *Report of the Powering Performance Committee*. Proceedings of the 15th International Towing Tank Conference.

ITTC (1987). "Report of the Resistance and Flow Committee". In: *The Resistance Committee*. Proceedings of the 18th International Towing Tank Conference, Kobe, Japan.

ITTC (1996). "Final Report and Recommendations to the 11th ITTC". In: *The Resistance Committee*. Proceedings of the 11th International Towing Tank Conference.

ITTC (2002). "Final Report and Recommendations to the 23rd ITTC". In: *The Specialist Committee on Validation of Waterjet Test Procedures*. Proceedings of the 23rd International Towing Tank Conference.

ITTC (2005a). "Final Report and Recommendations to the 24th ITTC". In: *The Specialist Committee on Validation of Waterjet Test Procedures*. Proceedings of the 24th International Towing Tank Conference.

ITTC (2005b). "ITTC Recommended Procedures and Guidelines Testing and Extrapolation Methods High Speed Marine Vehicles, Waterjets Waterjet System Performance". In: *ITTC - International Towing Tank Conference*. Procedure 7.5-02-05-03.2, pp. 1–10.

ITTC (2008). "ITTC Recommended Procedures and Guidelines Ship Models". In: *ITTC - International Towing Tank Conference*. Procedure 7.5-02-02-02, pp. 1–9.

ITTC (2011a). "ITTC Recommended Procedures and Guidelines 1978 ITTC Performance Prediction Method". In: *ITTC - International Towing Tank Conference*. Procedure 7.5-02-03-01.4, pp. 1–10.

ITTC (2011b). "ITTC Recommended Procedures and Guidelines 1978 ITTC Performance Prediction Method". In: *ITTC - International Towing Tank Conference*. Procedure 7.5-02-02-01.

ITTC (2011c). "ITTC Recommended Procedures and Guidelines Propulsive Performance Prediction". In: *ITTC - International Towing Tank Conference*. Procedure 7.5-02-05-03.1, pp. 1–9.

ITTC (2011d). "ITTC Recommended Procedures and Guidelines Ship Models". In: *ITTC - International Towing Tank Conference*. Procedure 7.5-01-01-01, pp. 1–9.

ITTC (2011f). "ITTC Recommended Procedures and Guidelines Uncertainty Analysis - Example for Waterjet Propulsion Test". In: *ITTC - International Towing Tank Conference*. Procedure 7.5-02-05-03.3, pp. 1–9.

ITTC (2014). "Final Report and Recommendations to the 27th ITTC". In: *The Propulsion Committee*. Proceedings of the 27th International Towing Tank Conference.

Jessup, S., Donnelly, M., Fry, D., Cvsanelli, D., and Wilson, M. (2008). "Performance Analysis of a Four Waterjet Propulsion System for a Large Sealift Ship". In: *Twenty-Seventh Symposium on Naval Hydrodynamics*, pp. 769–795.

Kamal, I. M. (2015). "An insight into the powering performance of large medium-speed waterjet and propeller driven catamarans through model testing". PhD Thesis. University of Tasmania.

Kandasamy, M., Georgiev, S., Milanov, E., and Stern, F. (2011). "Numerical and Experimental Evaluation of Waterjet Propelled Delft Catamarans". In: *FAST 2011 - 11th International Conference on Fast Sea Transportation*. Honolulu, Hawaii, USA, pp. 217–224.

Larsson, L. and Raven, H. C. (2010). *Ship resistance and flow*. The Principles of Naval Architecture Series. Jersey City, N.J.: Society of Naval Architects and Marine Engineers (SNAME).

Lin, W. C. (1990). "Report of the panel on validation procedures". In: *Proceedings of the 19th International Towing Tank Conference*. Madrid, Spain.

Lindgren, H., Aucher, M., Bowen, B. S., Gross, A., Minsaas, K. J., Muntjewerf, J. J., Tamura, K., and Wermter, R. (1978). "Proceedings of the 15th International Towing Tank Conference". In: *International Towing Tank Conference*, pp. 1–46.

Manen, J. D. and Oossanen, P. (1988). *Principles of Naval Architecture (PNA), Volume II: Resistance and Propulsion*. Society of Naval Architects and Marine Engineers (SNAME).

MARIN (2008). *Calm Water Tests for the JHSV Wave Piercing Catamaran*. Final Report 22162-3-DT. Report has been ordered by: Bollinger Shipyards Inc. 100 James Drive Suite 350 St Rose LA 70087 USA. Maritime Research Institute Netherlands (MARIN).

Marquardt, M. W. (2011). *Summary of Two Independent Performance Measurements of the ONR Axial Waterjet 2 (AxWJ-2)*. Hydromechanics Department Report NSWCCD-50-TR-2011/01. Carderock Division, Naval Surface Warfare Center (NSWCCD).

McCarthy, J. H., Power, J. L., and Huang, T. T. (1976). "The Roles of Transition, Laminar Separation and Turbulence Stimulation in the Analysis of Axisymmetric Body Drag". In: *Proceedings of the Eleventh ONR Symposium on Naval Hydrodynamics, sponsored by the Office of Naval Research (ONR), London*, pp. 69–95.

National Physical Laboratory (1960). *Standard Procedure for Resistance and Propulsion Experiments with Ship Models*. NPL Report SHR 10/59 Revised. Deptartment of Scientific and Industrial Research, Ship Division, National Physical Laboratory.

Oura, T. and Ikeda, Y. (2007). "Maneuverability Of A Wavepiercing High-Speed Catamaran At Low Speed In Strong Wind". In: *The 2nd International Conference on Marine Research and Transportation*. Naples, Italy, pp. 83–88.

Øyan, E. (2012). "Speed and powering prediction for ships based on model testing". Master Thesis. Norwegian University of Science, Technology (NTNU), Faculty of Engineering Science, and Technology, Department of Marine Technology.

Preston, J. H. (1958). "The minimum Reynolds number for a turbulent boundary layer and the selection of a transition device". In: *Journal of Fluid Mechanics* 3.04, pp. 373–384.

Rispin, P. (2007). *Final Report: Self-Propulsion Model Tests for Application to a High-Speed Sealift Ship Utilizing Advanced Axial-Flow Waterjets*. Technical report 813-7. Center for the Commercial Deployment of Transportation Technologies (CCDoTT).

Robbins, A., Thomas, G., Renilson, M., Macfarlane, G., and Dand, I. (2009). "Vessel Trans-Critical Wave Wake, Divergent Wave Angle and Decay". In: *International Journal of Maritime Engineering* 151.A2, pp. 1–14.

Rovere, J. E. (1997). "Catamaran Resistance from Tests on a Single Demihull". In: *Proceedings 4th International Conference of Fast Sea Transportation (FAST97)*. Vol. 2. Sydney, Australia: ADI Limited, Australia, pp. 737–741.

Roy, S. M. (1994). "The Evolution of the Modern Waterjet Marine Propulsion Unit". In: *International Symposium of Waterjet Propulsion. The Royal Institute of Naval Architects (RINA), London*.

Scherer, O., Mutnick, I., and Lanni, F. (2001). "Procedure for Conducting a Towing Tank Test of a Waterjet Propelled Craft Using Laser Doppler Velocimetry to Determine the Momentum and Energy Flux". In: *26th American Towing Tank Conference (ATTC)*.

Schlichting, H. and Gersten, K. (2000). *Boundary-layer theory*. 8th rev. and enl. Berlin ; New York: Springer, xxiii, 799 p.

Schuster, S. (1955). *Beitrag zur Frage der Kanalkorrektur bei Modellversuchen*. Tech. rep. Bd. 3, 1955/56. Schiffstechnik.

Scott, J. R. (1970). "On Blockage Correction and Extrapolation to Smooth Ship Resistance". In: *SNAME Transactions*, pp. 288–324.

Steen, S. and Aarsnes, J. V. (2014). *Experimental Methods in Marine Hydrodynamics*. Trondheim, Norway: Norwegian University of Science and Technology (NTNU).

Takai, T., Kanadasamy, M., and Stern, F. (2011). "Verification and validation study of URANS simulations for an axial waterjet propelled large high-speed ship". In: *Journal of Marine Science and Technology* 16.4, pp. 434–447.

Tamura, K. (1975). "Blockage Correction". In: The 14th International Towing Tank Conference, Ottawa, Canada.

Taylor, E. S. (1974). *Dimensional analysis for engineers*. Oxford University Press.

Thornhill, E. (1999). "Development of Waterjet Testing Techniques". Master Thesis. Faculty of Engineering and Applied Science, Memorial University of Newfoundland, St. John's. Newfoundland. Canada.

van Terwisga, T. J. C. (1996). "Waterjet-Hull Interaction". PhD Thesis. Delft University of Technology, Delft, Netherlands.

Vantorre, M. (2003). "Review of practical methods for assessing shallow and restricted water effects". In: *International Conference on Marine Simulation and Ship Maneuverability - MARSIM'03*. Ghent University,Department of Mechanical construction and production.

Wilson, M. B., Gowing, S., Chenakas, C. J., and Lin, C. W. (2005). "Waterjet-Hull Interaction for Sealift Ships". In: *International Conference on Marine Research and Transportation (ICMRT'05)*.

Zürcher, K., Bose, N., Binns, J. R., Thomas, G., and Davidson, G. (2013). "Design and Commissioning Tests for Waterjet Self-Propulsion Testing of a Medium-Speed Catamaran Ferry using a Single Demihull". In: *Third International Symposium on Marine Propulsors (SMP'13)*. Launceston, Tasmania, Australia, pp. 97–103.